Electronic Quantum Fluids in Graphene and Quantum Hall Systems

Glenn Wagner

Merton College

University of Oxford

A thesis submitted for the degree of

Doctor of Philosophy

Trinity 2021

This thesis is dedicated to

my brother

Acknowledgements

First and foremost, I would like to thank my supervisor Steven Simon, from whom I have learnt so much. It was his undergraduate solid state course that first inspired me to consider a PhD in condensed matter physics and his passion for the quantum Hall effect is infectious. Steve has a great intuition for problems and I admire the wealth of his knowledge of both theoretical and experimental physics.

A very special thanks goes out to Dung Nguyen, a postdoc who took me under his wing from the very start of my PhD. I could not have hoped for a better mentor. I have learnt much from him and am impressed by the depth of his knowledge of the quantum Hall effect and field theory. Some of my favourite memories from my PhD were our blackboard discussions in Oxford and my research visit in Brown.

I want to thank all of my collaborators in Oxford and beyond. I had the pleasure of working with my academic sibling Henrik Røising, with fellow PhD student Yves Kwan, masters student Nilotpal Chakraborty and with the postdocs Dmitry Kovrizhin, Fernando de Juan, Nick Bultinck and Felix Flicker as well as with Sid Parameswaran and Bertrand Halperin. My time in Oxford during my PhD would not have been the same without my office mates Aleksandra Ziolkowska and Sam Garratt, with whom I share many fond memories of physics chat, formals, birthday parties and club nights. I thank all the other PhD students in the department during my time in Oxford. I also want to thank all the other students, postdocs professors I have had the luck to interact with during conferences, summer schools and seminars in Oxford and abroad. In particular, I thank Leonid Levitov, Gunnar Möller, Frank Pollmann, and Lars Fritz for insightful discussions. I thank Nicolas Regnault for assistance with the DiagHam software. I am grateful to Grisha Falkovich with whom I first embarked on my foray into electron hydrodynamic during a summer research programme at the Weizmann Institute back in 2015.

I would like to thank Merton College and its community of fellows and graduate

students. It was the place for many stimulating discussions and some very fine food. The Merton MCR always felt like home to me, with all the formal exchanges, guest nights, food tastings, Saturday morning brunches and bops. I also want to thank all my students at Merton College who I have had the pleasure of teaching. Their endless curiosity and intransigent questions lead to many interesting discussions. And I would like to thank my undergraduate tutors at Merton, Simon Hooker, Alan Barr and Alexander Schekochihin for teaching me how to think about physics.

I want to thank the KITP for hosting me during the Graduate Fellow programme in the Fall of 2020. I particularly benefited from the talks on twisted bilayer graphene and Leon Balents' weekly group meeting.

A huge thanks goes out to my friends, whose emotional support has allowed me to thrive. I thank Carla Groenland for countless evenings cooking together both virtually and in person, bike rides, picnics, film nights and most of all, conversations about life. I thank Mantas Abazorius for his long-lasting friendship and support, many conversations about food, and last but not least his sunny disposition and lightheartedness that never fails to cheer me up. I thank Hannes Britz for many film marathons, video game nights and countless skype-calls over the years. I thank Jason Parisi for being a fantastic housemate during the lockdown. The Saturday afternoon bikes rides, followed by homemade pizza are what kept me going during that time. And the many versions of tiramisu. There will always be a special place in my heart for my Merton physics friends from undergrad, our physics cooking and film nights, pool-playing and eventually the many antics in during the balls in *The Swan* to the tune of Tubthumping. I also fondly remember the members of *Spice Club* with whom many evenings in my first year were spent cooking, including the infamous Burns' Night and tacos with the spiciest chillies in the world.

I thank all my family and in particular my parents Sandra and Richard and my brother Gregory for their enduring support and encouragement, many pre-brunch skypes and virtual cooking.

Glenn Wagner

Oxford, June 2021

Abstract

This thesis focuses on several examples of strongly correlated electronic quantum fluids.

In chapter 2 we use a kinetic theory approach to describe the transport properties of bilayer graphene near charge neutrality. After solving the semiclassical Boltzmann equation, we find that the results are well approximated by a hydrodynamic two-fluid model. A fluid of electrons and a fluid of holes interact with each other via Coulomb drag.

Chapter 3 looks at quantum Hall edges. We consider a quantum Hall edge coupled to a driven quantum dot and compute the current on the edge downstream from the contact. We show that Coulomb interactions between the dot and the edge renormalize the charge in the current pulses.

Chapter 4 focuses on the bilayer quantum Hall system. Two layers of quantum Hall fluid are separated by a variable distance. At large interlayer separation, we have two well-separated composite Fermi liquids and we consider the pairing between the two layers as the interlayer separation is decreased. We propose a new trial state for this paired phase of matter and use exact diagonalization numerics to investigate this proposal.

Publications

This thesis is based on the work reported in the following publications:

1. G Wagner, DX Nguyen, SH Simon, BI Halperin: *s-wave paired composite-fermion electron-hole trial state for quantum Hall bilayers with $\nu = 1$*: arXiv: 2106.00690

2. G Wagner, DX Nguyen, SH Simon: *Transport properties of multilayer graphene*: Phys. Rev. B **101**, 245438 (2020)

3. G Wagner, DX Nguyen, SH Simon: *Transport in bilayer graphene near charge neutrality: Which scattering mechanisms are important?*: Phys. Rev. Lett. **124**, 026601 (2020)

4. DX Nguyen, G Wagner, SH Simon: *Quantum Boltzmann equation for bilayer graphene*: Phys. Rev. B **101**, 035117 (2020)

5. G Wagner, DX Nguyen, DL Kovrizhin, SH Simon: *Interaction Effects and Charge Quantization in Single-Particle Quantum Dot Emitters*: Phys. Rev. Lett. **122**, 127701 (2019)

6. G Wagner, DX Nguyen, DL Kovrizhin, SH Simon: *Driven quantum dot coupled to a fractional quantum Hall edge*: Phys. Rev. B **100**, 245111 (2019)

Further publications that were not included in this thesis are listed below:

1. YH Kwan, G Wagner, T Soejima, MP Zaletel, SH Simon, SA Parameswaran, N Bultinck: *Kekulé spiral order at all nonzero integer fillings in twisted bilayer graphene*: arXiv: 2105.05857

2. G Wagner, HS Røising, F Flicker, SH Simon: *A microscopic Ginzburg–Landau theory and singlet ordering in Sr_2RuO_4*: arXiv: 2012.09866

3. YH Kwan, G Wagner, N Chakraborty, SH Simon, SA Parameswaran: *Orbital Chern insulator domain walls and chiral modes in twisted bilayer graphene*: arXiv: 2007.07903

4. G Wagner, F de Juan, DX Nguyen: *Quantum Hall effect in curved space realized in strained graphene*: arXiv: 1911.02028

Contents

Chapter 1

Introduction

1.1 Prelude: Popular introduction

The electron is one of the fundamental particles of the Standard Model. In fact, it is safe to say that it is the most well-studied particle in the Standard Model. Quarks are always confined within composite particles like protons. Neutrinos are elusive because they only interact via the weak force. But electrons—are simple. They can be studied in isolation to a great precision. The mass of the electron is known to one part in a billion[1]. Its magnetic moment is known to a precision of twelve decimal places[1]. So does that mean we know everything there is to know about electrons?

To make an analogy, let us imagine a future where self-driving cars are a reality and car manufacturing has been taken over by a single company. Every car it produces is exactly the same. We take one of these cars and we study all of its properties. We know how much it weighs, how fast it accelerates, how much gas it uses and how much CO_2 it emits. Does this mean we know all there is to know about cars? Take a bunch of these cars and put them on a road together. Now the cars need to watch out that they don't crash into each other. If traffic is too dense, they will form traffic jams. Suddenly we have a number of cars interacting with each other and interesting things happen. We have emergent phenomena. There are many examples of emergent phenomena in the world: Flocks of birds, ant-hills, stock market crashes. What they all have in common is that to understand them it's not enough to study the individual building blocks. We need to study the system as a whole and study the interactions of the many building blocks with

each other.

In much the same way, when we put a bunch of electrons together, interesting things can happen. Much like cars, electrons don't like to crash into each other—they repel one another (This repulsion is known as the Coulomb interaction.). Electrons can get stuck in traffic jams (This is known as a Mott insulator.). Electrons go on coordinated dances with each other (We call the description of this dance the wavefunction of the electrons.). So even though we understand individual electrons very well, understanding what happens in many-electron systems is still a very active area of research. In this thesis we explore electronic quantum fluids—in other words: fluids made up of electrons.

1.2 Motivations

1.2.1 Condensed matter theory

Condensed matter is the study of emergent phenomena in many-body (quantum) systems. Below, we list a number of motivations for studying this field, illustrating each point with some work that was conducted during this DPhil.

- ***Because physics is universal:*** The same equations may be used to describe many different systems across different areas of physics. The renormalization group tells us that after coarse-graining, many systems look alike.

  Example: The hydrodynamic description of graphene (Chapter 2) is a beautiful example of universality in physics—the same fluid equations that have been known to govern classical fluids since the 19th century turn out to govern the flow of electrons in clean samples of graphene. Hydrodynamics is an effective field theory which only cares about the coarse-grained physics and is also used in plasma physics and high-energy physics.

- ***Because condensed matter has useful applications:*** Semiconductors revolutionized the world by allowing computers to thrive. Superconductors are used for medical imaging and to levitate trains. Materials that may show promise in the future include graphene and high temperature superconductors.

Example: Quantum Hall edges are a promising approach to constructing single-electron sources which may be useful for transmitting qubits across a device (Chapter 3).

- ***Because nature is emergent:*** Everything that surrounds us consists of many interacting parts. The essence of condensed matter physics is the realization that interacting quantum many-body problems become computationally intractable very quickly as the number of particles in the system increases. Although we understand very well the fundamental equations of motion governing a collection of electrons, for a generic system it is impossible to solve the equations exactly for more than a few dozen electrons. Strongly correlated phases of matter cannot be understood as a simple perturbation away from a non-interacting phase either. Instead they require entirely new concepts in order to be understood.

  Example: Take the bilayer quantum Hall problem (Chapter 4), where we have two layers of quantum Hall fluid separated by some distance d. At large d, although the system is built up out of electrons, the most convenient description of this system is in terms of emergent quasiparticles called composite fermions. At small d, this system is best described in terms of electrons. We will discuss a proposal to relate these two emergent descriptions.

- ***Because solid state experiments are a playground for fundamental physics in the lab:*** Before a fully-fledged quantum computer becomes available, we may need to rely on quantum simulators to probe difficult quantum problems. To do that, one builds an experiment that accurately reproduces a model one would like to study. Performing a measurement on that experiment is then equivalent to solving the model. Ultra-cold atom gases can be used to study the Hubbard model.

  Example: The electrons in strained graphene behave analogously to electrons moving in curved space. Thus strained graphene allows us to simulate quantum field theory in curved space in the lab [2].

- ***Because condensed matter connects to interesting and deep areas of mathematics:*** Since the 1980s, it has become clear that some phases of matter fall

beyond the classical Landau-Ginzburg paradigm and are classified using topology. The mathematics of K-theory and category theory then allows us to come up with a complete classification of such phases.

Example: In twisted bilayer graphene we have an interesting interplay of strong correlations and topology which affects the energetics of domain walls in that system [3].

- ***Because we can study these materials in the lab:*** In condensed matter there is a rich interplay between cutting-edge theory and state-of-the art experiments.

  Example: Strontium Ruthenate is an unconventional superconductor. The electrons in a superconductor pair up to form Cooper pairs and these Cooper pairs flow without dissipation. The way that the electrons pair up in Strontium Ruthenate is enigmatic however and hence we call it an unconventional superconductor. Strontium Ruthenate is one of the most widely studied unconventional superconductors and due to the wide range of experimental probes that are available we can make progress on this problem. For example we can write down a Ginzburg-Landau theory guided by experimental constraints to help identify candidates for the superconducting order parameter[4].

Electronic quantum fluids are useful platforms for studying many-body physics. In this thesis we will study electronic quantum fluids in low-dimensional systems.

1.2.2 Low-dimensional physics

Although the world that surrounds us has three spatial dimensions, there are a number of reasons why studying lower-dimensional problems (in one or two spatial dimensions) is interesting.

On the one hand, lower-dimensional problems are often simpler to solve and hence we can understand them better than higher-dimensional problems[1]. Famously, the Ising model can be solved exactly in one[5] and two[6] dimensions, but not in higher dimensions.

[1]This is not always true of course, notably mean-field theory is typically a better approximation in higher dimensions and becomes exact in the limit of infinite dimensions.

In one dimension, there are many examples of Hamiltonians that can be solved exactly, which has spawned the vast field of integrability. There are other powerful analytical techniques applicable in one spatial dimension, such as bosonization[7], which we will use to study quantum Hall edges in chapter 3. One-dimensional systems are also amenable to powerful numerical techniques such as the density matrix renormalization group (DMRG)[8].

Two dimensional problems are also interesting in their own right. For one, there is a wealth of experiments performed in two dimensional systems. One advantage is that the carrier concentration in two-dimensional materials can be easily tuned using gating, therefore allowing a high level of control. Furthermore, materials like graphene are extremely clean, allowing for astonishing transport regimes to be accessed, as we discuss in chapter 2.

On the theoretical side, there are interesting topological effects in two dimensions such as the Kosterlitz–Thouless transition[9] and the quantum Hall effect[10]. In three dimensions, particles are classified as either bosons or fermions, depending on how their wavefunctions changes under the exchange of two identical particles. On the other hand, in two dimensions we can have particles that are neither bosons or fermions, these are the so-called anyons. In chapter 3 we consider how to excite anyons on the edge of a quantum Hall fluid. Another type of particle special to two dimension is the so-called composite fermion and this will be the protagonist of chapter 4.

1.3 Outline

This thesis is divided into two parts. In part I (containing chapter 2) we study graphene. Chapter 2 shows how the electrons flowing in bilayer graphene behave like a fluid. In part II (containing chapters 3 and 4) we look at the quantum Hall effect. Chapter 3 looks at the ripples on the edge of a quantum Hall fluid and chapter 4 studies the analog of a superconducting fluid in quantum Hall bilayers. We conclude this thesis in chapter 5 and offer a perspective for the future.

1.4 Graphene

Graphene is a material which is beautiful in its simplicity. It consists of a single sheet of carbon atoms arranged on a honeycomb lattice. In a sense it is the most two-dimensional any material could be: It is only one atomic layer thick! It is also surprisingly easy to produce a sheet of graphene, all one needs is a piece of readily available graphite such as is found in pencils and a piece of scotch tape. By sticking the scotch tape on the graphite and pulling it off, one can exfoliate a sheet of graphene. Despite this seeming simplicity, graphene was only isolated in 2004[11].

In the same way that single monolayers of graphene are exfoliated from graphite[12], one can also exfoliate bilayers of graphene[13] and this is going to be the material we focus on in part I of this thesis. Bilayer graphene has a number of wonderful properties, for the following the most important property will be that it is extremely clean and this will lead to an extremely unusual transport regime.

1.4.1 Hydrodynamics

Hydrodynamics is an area of physics with a long history. It started with the study of classical fluids such as water or oil. The main idea is that the macroscopic dynamics of these fluids can be described in terms of the evolution of a small number of conserved quantities, such as particle number, momentum and energy. Even though collisions happen on a fast timescale τ_{coll}, since these collisions conserve particle number, momentum and energy, the conserved quantities evolve on a much longer time scale $t \gg \tau_{\text{coll}}$. The evolution of these quantities is described by the Navier–Stokes equations. Essentially, hydrodynamics relies on a separation of scales. One the one hand we have the macroscopic length scale L, which might be the size of our fluid channel. One the other hand we have a microscopic length scale λ_{mfp}, which is the mean free path (the typical distance an atom or molecule travels between collisions). We coarse-grain such that we consider the evolution of fluid parcels which have a mesoscopic size ℓ such that $L \gg \ell \gg \lambda_{\text{mfp}}$.

Hydrodynamics is more generally applicable than just to classical fluids however. The hydrodynamic formalism can be extended to quantum fluids such as superfluids. We may then ask what other types of condensed matter systems are well-described by

hydrodynamics. Some of the most studied condensed matter systems consist of electrons in metals. Can these behave hydrodynamically as well?

In ordinary metals, phonons and impurities cause dissipation of the momentum of the electrons. Since momentum is not conserved, hydrodynamics is not a good description of the system. However, in some ultra-clean materials one can enter a new regime, the so-called *hydrodynamic regime*, where the momentum of the electrons is approximately conserved. Typically at low temperatures, collisions of electrons with impurities dominate. At high temperatures, collisions of electrons with phonons dominate. If a material is sufficiently clean, there exists an intermediate temperature range dubbed the hydrodynamic window, where momentum is approximately conserved and hydrodynamics is is a good description.

We will apply the hydrodynamic formalism to the electronic fluid in bilayer graphene. Suspended bilayer graphene samples that have been investigated in recent experiments are extremely clean and as such are good candidates for hydrodynamic transport. To confirm that these experiments are indeed seeing hydrodynamic transport, we will model this system theoretically. We find that the hydrodynamic transport regime leads to distinct transport signatures. Ordinary metals satisfy what is known as the Wiedemann–Franz law: The electrical and thermal conductivity are proportional to each other since (at a fixed temperature), the charge and heat carried by an electron are proprtional to each other. However, we show that a signature of hydrodynamic transport in bilayer graphene is the violation of the Wiedemann–Franz law at charge neutrality. Another signature of hydrodynamic transport in bilayer graphene that we distill is the fast increase of the electrical conductivity away from charge neutrality.

1.4.2 Two-fluid models

What happens when you mix two types of fluid? Some fluids like oil and water are immiscible, they will not mix with each other and instead will phase separate. Other fluids like alcohol and water will mix readily. What happens when you mix two fluids will depend on the interactions between the fluid components. This leads us to the concept of a *two-fluid model*: This will consist of fluid equations for two different types of fluids which may

interact with one another. Two-fluid models have appeared in different contexts in the literature, for example a two-fluid model has been used to model traffic jams. In Ref. [14] a two-fluid model was developed where there is a fluid of moving cars and a fluid of stationary cars. One rather famous example from the realm of condensed matter physics is the two-fluid model of superfluid Helium introduced in 1938 by Tisza[15] and later refined by Landau[16]. Below the critical temperature, there is a finite density of both a normal and a superfluid component. The normal component of the fluid is responsible for its viscosity and carries the heat, whereas the superfluid component is dissipationless. This two-fluid model of Helium provided the explanation why some experiments seemed to show superfluid Helium had a nonzero viscosity whereas others seemed to support the opposite conclusion. We will find that a two-fluid model is the most appropriate description in bilayer graphene as well. In our case the two fluids in question are the electron and the hole fluids. At a special point called *charge neutrality* there is an equal number density of electrons and holes and hence we have particle-hole symmetry at this point. It is this regime close to charge neutrality that we explore.

1.4.3 Kinetic theory

Complementary to hydrodynamics, there is another approach to describing gases and fluids: Kinetic theory. Kinetic theory takes a more microscopic approach and the fundamental quantity one works with is the distribution function $f(\mathbf{p}, \mathbf{x}, t)$, which is defined such that $f(\mathbf{p}, \mathbf{x}, t)\, \mathrm{d}^D\mathbf{p}\, \mathrm{d}^D\mathbf{x}$ is the number of particles with positions in region $\mathrm{d}^D\mathbf{x}$ around $\mathbf{x}$ with momenta in region $\mathrm{d}^D\mathbf{p}$ around $\mathbf{p}$ at time t. D is the dimensionality of space. The evolution of the distribution function is described by the Boltzmann equation.

If there are conserved quantities, one can derive hydrodynamic equations from the kinetic theory by taking moments of the Boltzmann equation. Going from kinetic theory to hydrodynamics one is of course throwing away a lot of microscopic information. However, kinetic theory may be valid when hydrodynamics is not and vice versa.

Kinetic theory and hydrodynamics are two complementary approaches in the sense that they have distinct but overlapping regimes of validity. Kinetic theory describes two-body collisions of particles and hence relies of having a valid quasiparticle description.

This is not necessarily a given in a quantum system. In particular, in a strongly correlated system, we may not have long-lived quasiparticles. The requirement for the validity of kinetic theory is therefore that interactions are weak enough, such that the quasiparticle lifetime $\tau_{\text{qp}} \gg \hbar/(k_B T)$, where T is the temperature. On the other hand, hydrodynamics does not rely on quasiparticles, since it describes only the evolution of coarse-grained quantities. Hydrodynamics has indeed successfully been applied to a variety of strongly-correlated systems [17, 18]. Hydrodynamics only requires conservation laws to be obeyed, i.e. the timescale on which conservation laws are violated needs to be $t \gg \tau_{\text{coll}}$.

1.4.4 Hydrodynamic transport in bilayer graphene

Bilayer graphene turns out to be in a regime where both kinetic theory and hydrodynamics are applicable. In Chapter 2, we apply kinetic theory to bilayer graphene. We use the semiclassical Boltzmann formalism to compute the transport properties of bilayer graphene and by comparing to experimental data, we are able to deduce that phonons play a crucial role for the residual momentum relaxation in the hydrodynamic regime [19, 20]. We write down a hydrodynamic two-fluid model that accurately agrees with the kinetic theory calculations. This work is then extended to multilayer graphene, where we find that the hydrodynamic window is relatively unchanged as a function of the number of layers [21].

1.5 Interlude: The quantum Hall effect and graphene

Despite their simplicity, monolayer and bilayer graphene display many interesting behaviours. In the previous section, we outlined the hydrodynamic regime of graphene, where the electrons behave like particles in a fluid. The hydrodynamic regime of monolayer and bilayer graphene occurs at temperatures between tens and a few hundred Kelvin. When graphene is cooled to much lower temperatures (tens of milli-Kelvin) and subjected to a strong magnetic field, it enters a new regime where the so-called quantum Hall effect (QHE) is observed[22]. The electrons form strongly correlated states that have topological properties.

Historically, graphene is not the place that the QHE was observed for the first time,

however, in recent years graphene has emerged as very convenient platform for studying the QHE. The QHE was first observed in two-dimensional electron gases in GaAs heterostructures in the 1980s. In fact, GaAs was also the first material in which hydrodynamic transport was observed. The common denominator of hydrodynamic transport and the QHE is that they both require extremely clean materials in order to be observed.

1.6 The Quantum Hall effect

The quantum Hall effect is certainly one of the most interesting and surprising emergent phenomena. When electrons in a two-dimensional metal such a graphene are subjected to a large magnetic field B at very low temperatures they can form exotic states of matter. In high school, we were all taught about the three phases of matter: Solid, liquids and gases. But it turns out that nature is much richer. The quantum Hall fluid, which consists of electrons performing a coordinated dance, is a completely new phase of matter, and an interesting one at that: it is a topological phase of matter. A Hamiltonian describes a topological phase of matter if it is gapped and it cannot be continuously deformed to the atomic insulator limit without closing the gap.

To understand the quantum Hall effect, it first makes sense to understand the non-interacting problem of electrons in a magnetic field in two dimensions. It turns out that the electrons live in flat bands, the so-called *Landau levels* (LL), each of which is highly degenerate. The number of filled LLs is known as the filling factor ν. If we completely fill an integer number of LLs ($\nu \in \mathbb{Z}$), we have the integer quantum Hall effect. However, more interesting things happen, when LLs are only partially filled ($\nu \in \mathbb{Q}$), this is known as the fractional quantum Hall effect. In many problems, and certainly in this thesis, it will be enough to consider the electrons moving in the lowest Landau level (LLL), i.e. $\nu \leq 1$. So the kinetic energy is completely quenched and the Hamiltonian will be given by the Coulomb interaction projected onto the LLL. Since there is no kinetic energy, this is by definition a strongly interacting problem, the interaction cannot be treated perturbatively.

The fractional quantum Hall effect hosts some very exotic particles called anyons, which have a fractional charge. This is an example of an emergent quasiparticle. Although

our system consists entirely of electrons with one unit of charge, when we look at the fractional quantum Hall system at $\nu = 1/3$ we appear to see particles with one third of the charge of the electron. The electron has effectively split in three! Certain types of anyon called non-abelian anyons may one day be used to build a topological quantum computer[23]. Non-abelian anyons arise in non-abelian quantum Hall states such as the proposed Moore–Read (also called Pfaffian) state at $\nu = 5/2$.

Over the years, different approaches have been developed to understand the quantum Hall effect. An early approach that was successful was to use trial wavefunctions. Laughlin had the insight to write down wavefunctions, now named after him, that turn out to be very good approximations to the true ground state[24]. Another useful viewpoint is that of composite fermions: Composite objects consisting of $2p$ vortices of the wavefunction bound to an electron, where $p \in \mathbb{Z}$. The fractional quantum Hall effect of electrons at filling factor $\nu = \frac{n}{2pn\pm1}$ can be mapped to an integer quantum Hall effect of composite fermions at filling factor $\nu_{\mathrm{CF}} = n$.

1.6.1 Quantum Hall edges

By definition the gap must close at the boundary between a topological phase of matter and a trivial phase of matter. This implies that at the edge of a quantum Hall fluid, there are gapless excitations. These are known as quantum Hall edge modes. In Chapter 3 we consider a mechanism to drive currents on these quantum Hall edges using a quantum dot. A quantum dot can be thought of as an artificial atom. It is an energy level that can either be empty, or occupied with an electron or anyon. When a quantum Hall edge is coupled to a quantum dot via a quantum point contact, driving the quantum dot can excite a current along the edge. If the charge on the dot is quantized, then one expects a current pulse along the edge that carries a quantized charge, when the charge hops from the dot onto the edge. This set-up is therefore promising as a single-particle source for quantum information applications.

In Chapter 3 we study the effect of interactions on this set-up. Using bosonization and a mapping to the well-known spin-boson model, we were able to show that the Coulomb interaction between the dot and the edge destroys the precise charge quantization of the

pulses [25, 26].

1.6.2 Bilayer quantum Hall

We consider two layers of quantum Hall fluid separated by distance d and coupled via the Coulomb interaction. If both individual layers have filling factor $\nu = 1/2$, both the small and large d limits are very well understood. At large interlayer distances, the two layers are decoupled and can each be thought of as a Fermi sea of composite fermions. At small interlayer distances, the state is an exciton condensate—an electron in one layer pairs up with a hole in another layer. This is the famous 111 state[27]. However, at intermediate distances, where the interlayer distance is on the order of the magnetic length, the situation is far less clear. The ground state phase diagram as a function of d is not known. Many proposals for this intermediate state have been put forward[28, 29, 30, 31, 32, 33, 34, 35, 36, 37, 38, 39].

In Chapter 4 we study an alternative proposal: the s-wave pairing of a composite fermion in one layer with a composite hole in the other layer. Using Monte-Carlo studies and exact diagonalization, we will show that this new trial state captures the relevant physics down to the smallest interlayer distances.

Part I

Graphene

Chapter 2

Hydrodynamic electron flow in bilayer graphene

2.1 Introduction

Ordinary metals are dirty. The electrons are constantly scattering off impurities, the boundary of the sample or the atomic lattice (which we can view as collisions of electrons with phonons). These collisions relax the momentum of the electrons. The scattering rate for momentum-relaxing (mr) collisions is obtained by summing up the various contributions according to Matthiesen's rule

$$\tau_{\text{mr}}^{-1} = \tau_{\text{e-phonon}}^{-1} + \tau_{\text{e-impurity}}^{-1} + \tau_{\text{e-boundary}}^{-1} + ... \tag{2.1}$$

When we apply a voltage to a metal, the electric field is constantly accelerating the electrons and imparting momentum onto them. However, the momentum of the electrons will be dissipated by the collisions of the electrons with impurities, the boundary or phonons. The system reaches a steady state, where the momentum imparted to the electrons by the electric field is balanced by the momentum dissipated due to collisions. This is the essence of the theory of transport in metals that Drude proposed in 1900[40]. The Drude equation is

$$\frac{d\mathbf{p}}{dt} = -e\mathbf{E} - \frac{\mathbf{p}}{\tau_{\text{mr}}}, \tag{2.2}$$

where $\mathbf{p}$ is the momentum of the electrons, $-e$ is the electron charge and $\mathbf{E}$ is the applied electric field. This leads to the famous Drude result for the electrical conductivity

$$\sigma = \frac{e^2 n \tau_{\text{mr}}}{m}, \tag{2.3}$$

where n is the number density of electrons and m is their mass. A kinetic calculation for the thermal conductivity of a Fermi gas yields[41]

$$\kappa = \frac{\pi^2}{3} \frac{k_B^2 n T \tau_{\text{mr}}}{m} \tag{2.4}$$

and so taking the ratio to compute the Lorenz number $\mathcal{L}$, one obtains the Wiedemann–Franz law

$$\mathcal{L} \equiv \frac{\kappa}{\sigma T} = \frac{\pi^2}{3} \left(\frac{k_B}{e} \right)^2, \tag{2.5}$$

which is satisfied for many metals.

Essentially Drude theory is a kinetic theory for electrons in metals. However, there is one important distinction between the kinetic theory as applied to classical fluids and as applied to metals. In a classical fluid such as water, the dominant type of scattering is between the water molecules themselves. There are very few impurities in water and there is no atomic lattice for the water molecules to collide with. This begs the question, is it possible to enter an electronic transport regime which is more similar to this classical hydrodynamic regime? In other words, is it possible to find a material, where the dominant type of scattering is between the electrons themselves? Clearly this needs to be a very clean material.

This transport regime is nowadays known as *electron hydrodynamics*. In this regime, the electron-electron collisions, which are momentum-conserving[1], are the dominant source of scattering. The momentum of the electrons is therefore almost conserved. We denote the scattering rate of the momentum-conserving (mc) collisions as

$$\tau_{\text{mc}}^{-1} = \tau_{\text{e-e}}^{-1}. \tag{2.6}$$

[1]Umklapp scattering can relax momentum, however we will argue in Sec. 2.4.5 that at least for graphene near charge neutrality Umklapp scattering is not important.

(a) ordinary metal (b) electron hydrodynamics

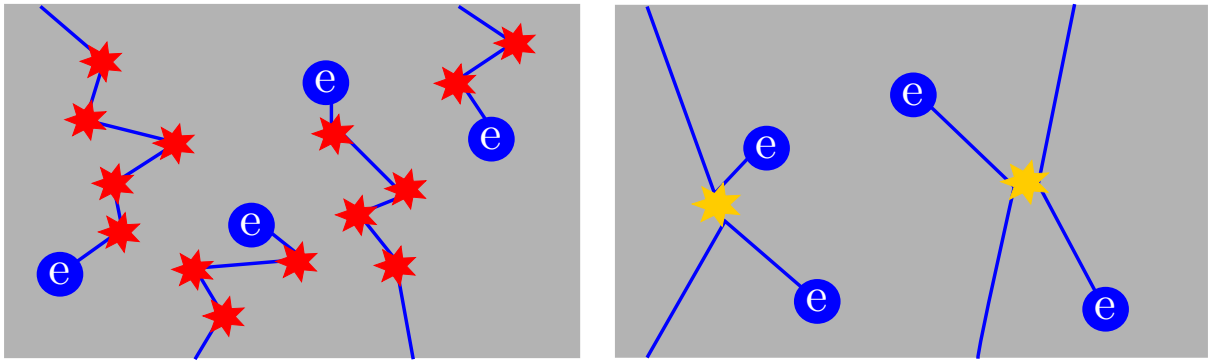

$\tau_{\mathrm{mr}}^{-1} \gg \tau_{\mathrm{mc}}^{-1}$ $\tau_{\mathrm{mc}}^{-1} \gg \tau_{\mathrm{mr}}^{-1}$

Figure 2.1: We distinguish momentum-relaxing collisions occuring on a timescale τ_{mr}(✸) and momentum-conserving collisions occuring on a timescale τ_{mc}(✸). Left: In the conventional diffusive transport regime of metals, the electrons predominantly collide with phonons and impurities, in momentum-relaxing collisions. Right: In the hydrodynamic regime, the electron-electron collisions are the dominant source of scattering. In these collisions, the momentum of the electrons is conserved.

Definition 1: The hydrodynamic regime

In the hydrodynamic regime of an electronic system, the scattering times satisfy

$$\tau_{\mathrm{mc}}^{-1} \gg \tau_{\mathrm{mr}}^{-1}. \tag{2.7}$$

where τ_{mc} is the timescale for momentum-conserving collisions and τ_{mr} is the timescale for momentum-relaxing collisions. This is illustrated in Fig. 2.1.

The hydrodynamic regime for electrons was first envisaged in 1962 by Gurzhi[42], who made the prediction of what is now known as the *Gurzhi effect*. Gurzhi's prediction was that as one enters the hydrodynamic regime, the resistivity decreases as the temperature increases. This is clearly a counter-intuitive result, for ordinary metals the resistivity increases as a function of temperature: As we increase the temperature, the momentum-relaxing collisions become more frequent, and hence via Eq. (2.3), the electrical conductivity decreases. To explain the Gurzhi effect, we should think about what limits the conductivity at different temperatures. We assume that there are no impurities. According to the Drude formula, the momentum-relaxing collisions are responsible

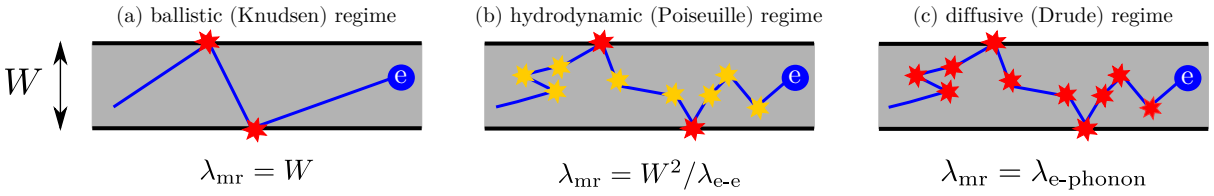

Figure 2.2: We distinguish momentum-relaxing collisions occuring on a timescale $\tau_{\rm mr}$(✸) and momentum-conserving collisions occuring on a timescale $\tau_{\rm mc}$(✸). As temperature is increased, the system moves from the Knudsen regime to the Drude regime. In certain materials one encounters the Poiseuille regime in between these two limits, where the Gurzhi effect is observed.

for limiting the electrical conductivity[2]. So we need to think about what mechanism sets the momentum-relaxing mean-free path $\lambda_{\rm mr} \sim \langle v \rangle \tau_{\rm mr}$ and then according to the Drude formula $\sigma \propto \lambda_{\rm mr}$. At the lowest temperatures, the momentum will be dissipated by electrons colliding with the boundary of the sample (panel (a) of Fig. 2.2). This leads to $\lambda_{\rm mr} \sim W$, where W is the width of the channel through which the electrons are flowing. With increasing temperature, electron-electron collisions become more frequent, until $\lambda_{\rm mc} = \lambda_{\text{e-e}} < W$ (panel (b) of Fig. 2.2). At this point, electrons undergo a random walk between collisions with the boundary and hence the distance travelled by the electrons between momentum-relaxing collisions increases to $\lambda_{\rm mr} \sim W^2/\lambda_{\text{e-e}}$. As we increase the temperature, electron-electron collisions become more frequent, $\lambda_{\text{e-e}}$ decreases, hence $\lambda_{\rm mr}$ increases and the conductivity increases as a function of increasing temperature: This is the Gurzhi effect. Finally, as we increase the temperature even further, electron-phonon collisions start becoming important and $\lambda_{\rm mr} = \lambda_{\text{e-phonon}}$ (panel (c) of Fig. 2.2). As the temperature increases, electron-phonon collisions become more frequent and the conductivity decreases as a function of temperature, taking us back to a more familiar regime. Fluid dynamicists love dimensionless numbers and in that spirit it is useful to define the Knudsen number $\text{Kn} = \frac{\lambda_{\text{e-e}}}{W}$. The Gurzhi effect occurs when we have the crossover from the (ballistic) Knudsen regime $\text{Kn} \gg 1$ to the (hydrodynamic) Poiseuille regime $\text{Kn} \ll 1$. The Gurzhi effect has a classical counterpart. In 1909 Knudsen observed that for gas flowing through a capillary, the pressure drop first increases and then decreases as the density of a gas is increased[43].

[2]Although we will see in Sec. 2.4.1 that in bilayer graphene at charge neutrality, momentum-conserving electron-electron collisions alone can limit the conductivity.

For many years, the electron hydrodynamic regime remained a theorist's fantasy. No materials were known that were clean enough. This changed in the 1980s, when ultra-high mobility two-dimensional electron gases (2DEGs) such as GaAs heterostructures were developed. This is the same advance that lead to the discovery of the quantum Hall effect, which will be the subject of part II of this thesis. It was in these ultra high mobilility 2DEGs that the electron hydrodynamic regime was first accessed experimentally [44, 45, 46] and this lead to a revival in theoretical interest in the problem [47, 48].

Since then, a new material has come on the market: Graphene. Graphene is clean. Very clean. Electrons in copper have a typical mean free path of around 40nm at room temperature[49], whereas in graphene, the mean free path for electron-impurity collisions can reach over 1μm at 200K[50]. Graphene has attracted an enormous amount of attention in the last decade[51]. There are several properties of graphene that explain the interest in this material: (i) It is the most two-dimensional any material can be, being only one atomic layer thick. (ii) It is simple to describe theoretically, consisting only of carbon atoms on a honeycomb lattice. (iii) The low-energy excitations offer a condensed matter realization of massless Dirac fermions. (iv) Graphene is extremely clean and the electrons have very high mobility. (v) Due to its two-dimensional nature, the carrier concentration in graphene can very easily be tuned via gating, offering a high level of control.

One of the first signatures of electron hydrodynamics in graphene was the observation of the *negative non-local resistance* [52, 53]. When current is injected into a graphene channel from a source, the flow profiles are drastically different in the Ohmic as opposed to the hydrodynamic regime. In the Ohmic regime, the electrons always flow outward from the current source (panel (a) of Fig. 2.3). On the other hand, if we treat the electrons as a viscous fluid, then electron whirlpools can form (panel (b) of Fig. 2.3). Due to the presence of these vortices, the electron flow profile is modified and in particular, electrons may flow towards the source as opposed to away from it. The experimental signature in which this will show up is that the voltage measured along the boundary has the "wrong" sign in the hydrodynamics regime and this has been dubbed negative non-local resistance.

Since then, further evidence that supports this picture of hydrodynamic electron trans-

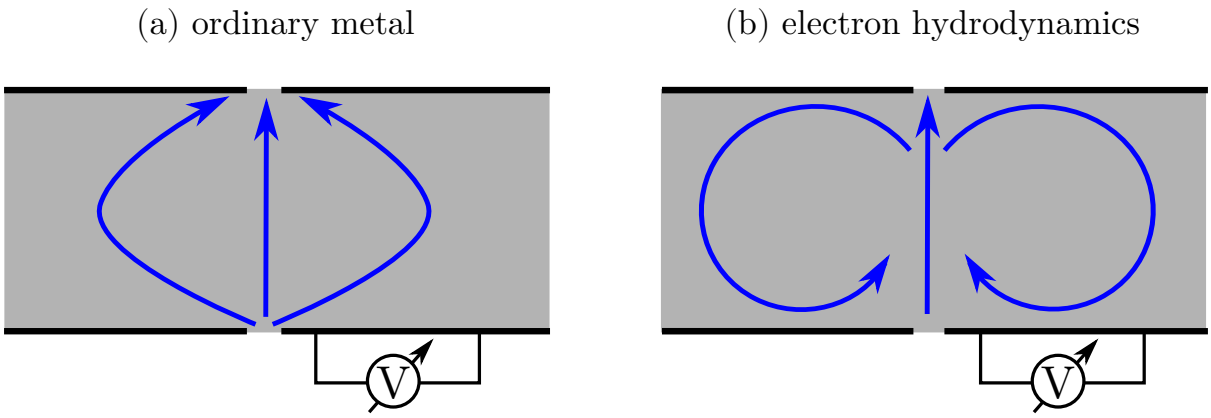

Figure 2.3: We consider a geometry with a current source and current drain on opposite sides of a finite-width channel. Due to the formation of electron whirlpools, the voltage V measured along the boundary of the sample will have the opposite sign in the hydrodynamic regime, compared to the conventional electronic transport regime. This effect is dubbed the negative nonlocal resistance.

port in monolayer graphene has come to light. The *Wiedemann–Franz law violation* [54], where the thermal conductivity is either enhanced or suppressed relative to the prediction of the Wiedemann–Franz law can have a hydrodynamic origin[3].

Experiments have observed *superballistic flow through constrictions*[56]. The measurement of the conductivity through narrow constrictions reveals that the flow is enhanced with respect to the case of ballistic transport. Due to viscous effects, the electrons can "slipstream" through the constriction[57]. In this geometry as in the Gurzhi effect, the rate of momentum relaxation decreases in the hydrodynamic regime.

An even more striking observation came in 2019, when two groups were able to image the *Poiseuille flow* in graphene. Poiseuille flow is a classical effect from undergraduate fluid dynamics. If one solves the Navier-Stokes equations for a viscous fluid flowing in a channel with a finite width, one finds a parabolic velocity profile. The first group measured the Hall voltage across a channel, using that to deduce the current profile [58]. The second group used a magnometry measurement to measure the spatially-dependent magnetic field, which allows one to deduce the spatial distribution of current by inverting the Biot-Savart law [59]. The current profile of the electron flow through the channel measured by both groups agrees with the prediction for a viscous fluid and thus lends

[3]The Wiedemann–Franz law violation is not a unique signature of hydrodynamic transport however, since other possible mechanisms such as bipolar diffusion [55] or phonon cooling [54] may be involved.

further evidence to the idea that electrons in monolayer graphene can be hydrodynamic.

Key Concept 1: Experimental evidence of hydrodynamic transport in monolayer graphene

To summarize, we have presented five transport signatures of the hydrodynamic regime that have been observed in monolayer graphene

1. *Gurzhi effect*[53][a]
2. *Negative non local resistance*[52, 53]
3. *Wiedemann–Franz law violation*[54]
4. *Superballistic flow through constrictions*[56]
5. *Poiseuille flow*[58, 59]

[a]Due to the details of the scattering off the boundary, in particular the large slipping length, the Gurzhi effect in monolayer graphene is weak. The resistivity is monotonic as a function of temperature (no Gurzhi effect), however the Gurzhi effect has been observed in the differential conductance.

While the transport properties of monolayer graphene have been extensively studied[60], other related materials are only beginning to be examined. We are interested in the question of whether bilayer graphene can exhibit hydrodynamic transport in the same way that monolayer graphene does. As in the case of monolayer graphene[61, 62], we expect that electrons in bilayer graphene (BLG) will have high mobility and scattering of electrons among themselves will be the dominant scattering mechanism. Advances in nanotechnology have recently allowed electrical measurements on suspended BLG samples[13, 63, 64, 65, 66, 67, 68, 69, 70]. A measurement of the electrical conductivity in BLG has been reported in Ref. [13] and we aim to understand these results using a theoretical framework. We focus our calculation on the regime explored in the experiment. This means we consider the chemical potential tuned to be close to the charge neutrality (CN) point, where the number density of electrons in the conduction band and holes in the valence band is equal. We also consider temperatures $T \sim 10\text{K}$ – 40K.

Our approach is similar to previous work on the conductivity of monolayer graphene

[71, 72], two coupled monolayers [73] and BLG[74, 75]. Compared to [74], which studies the case of clean BLG, we calculate the conductivity away from CN, which requires including additional scattering mechanisms. The paper [75] does study the conductivity of BLG away from CN by including the effect of disorder, however we aim to provide a more quantitative analysis allowing for comparison with experimental data.

2.2 Outline

In this chapter, we theoretically examine the zero frequency transport properties of BLG using a quantum Boltzmann equation (QBE) approach. To start off, in Sec. 2.3 we briefly review the derivation of the band structure and the explicit expressions for the single-particle wave functions in BLG. We also introduce the screened Coulomb interaction relevant for BLG near CN. We then discuss our QBE method in Sec. 2.4, with further details in App. A and in the paper[76]. The QBE method is a semiclassical approach and we discuss its validity in Sec. 2.5. Before solving the QBE, we develop some intuition for the problem by introducing our hydrodynamic two-fluid model in Sec. 2.6, providing further details in App. B. Solving the QBE is a numerically daunting task and the far simpler two-fluid model accurately describes the QBE results. The two-fluid model also provides us with explanations for two signatures of the hydrodynamic regime: The Wiedemann–Franz law violation and the fast increase of the electrical conductivity away from charge neutrality. We then explain how to solve the QBE in Sec. 2.7. We present numerical results obtained by solving the QBE for both electrical (Sec. 2.7.1) and thermal (Sec. 2.7.2) transport. We compare our results for the electrical conductivity to the experimental results from Ref. [13] in order to extract the value of the only free parameter of the theory: The phonon scattering rate. The value we determine for the phonon deformation potential lies within the range reported by previous authors. We show that our QBE results agree with the experimental data over a wide range of parameters. Finally we discuss the extension of our work to multilayer graphene in Sec. 2.8.

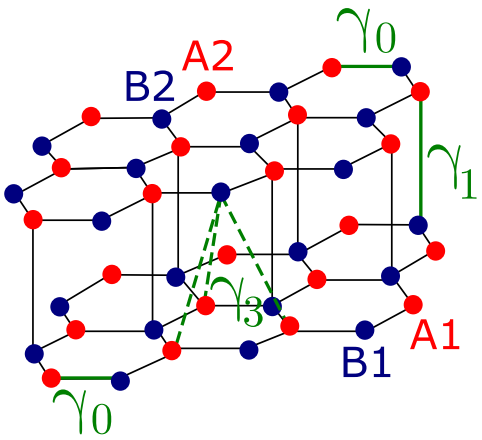

Figure 2.4: Sketch of the AB stacked bilayer graphene lattice used for the tight-binding Hamiltonian. There are two layers 1 and 2 and in each layer there are two inequivalent sites per unit cell labelled A and B. The hopping strengths γ_0 and γ_1 are the nearest-neighbour intralayer and interlayer hoppings respectively. The next-nearest neighbour interlayer hopping γ_3 leads to trigonal warping and is neglected in the following analysis.

2.3 The bilayer graphene Hamiltonian

We begin by discussing the microscopic model of bilayer graphene. Bilayer graphene consists of two stacked layers of graphene. Graphene itself consists of carbon atoms arranged on a honeycomb lattice. Since the honeycomb lattice is bipartite, the carbon atoms in a sheet of graphene can be classed as belonging to either the A or the B sublattice. In bilayer graphene, an atom in the top layer in the A sublattice can either sit on top of an atom in the bottom layer in the A sublattice (AA stacking) or the B sublattice (AB stacking, also known as Bernal stacking). We focus on AB stacked bilayer graphene, since this is the form that is most commonly found in experiments[13]. Quantum Monte Carlo[77] and density functional theory[78] calculations confirm that this is the more stable configuration.

2.3.1 Tight-binding Hamiltonian

The tight-binding Hamiltonian of AB stacked bilayer graphene with the couplings defined in Fig. 2.4 has the form

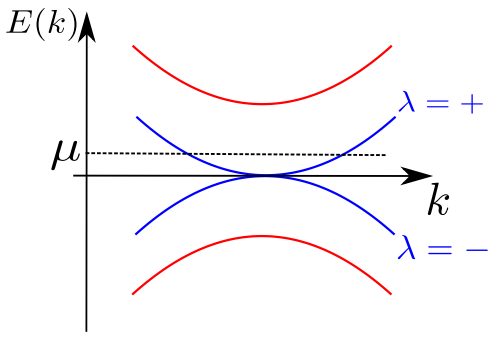

Figure 2.5: The low-energy bandstructure of bilayer graphene consists of two parabolic bands. We consider the transport regime near charge neutrality, i.e. $\beta\mu \lesssim 1$.

$$\mathcal{H}_{\text{kin}} = \gamma_0 \sum_{\mathbf{R}} \sum_i c^\dagger_{A_1}(\mathbf{R}) c_{B_1}(\mathbf{R}+\mathbf{l}_i) + h.c. \tag{2.8}$$

$$+ \gamma_0 \sum_{\mathbf{R}} \sum_i c^\dagger_{A_2}(\mathbf{R}) c_{B_2}(\mathbf{R}+\mathbf{l}_i) + h.c. \tag{2.9}$$

$$+ \gamma_1 \sum_{\mathbf{R}} c^\dagger_{A_2}(\mathbf{R}) c_{B_1}(\mathbf{R}) + h.c. \tag{2.10}$$

$$+ \gamma_3 \sum_{\mathbf{R}} \sum_i c^\dagger_{B_2}(\mathbf{R}) c_{A_1}(\mathbf{R}+\mathbf{l}_i) + h.c., \tag{2.11}$$

where $\mathbf{l}_1 = a(\frac{\sqrt{3}}{2}, \frac{1}{2})$, $\mathbf{l}_2 = a(-\frac{\sqrt{3}}{2}, \frac{1}{2})$ and $\mathbf{l}_3 = a(0,-1)$ are the three nearest neighbour displacements on the honeycomb lattice[4] (a is the lattice constant of graphene) and $\mathbf{R}$ is the position of a lattice site. $c^\dagger_{s_l}(\mathbf{R})$ creates an electron on sublattice $s \in \{A, B\}$ in layer $l \in \{1, 2\}$. $\mathcal{H}_{\text{kin}}$ is diagonal in spin so we are omitting the spin index for conciseness. We go to momentum space and introduce the operator $c_a(\mathbf{p}) = (c_{A_1}(\mathbf{p}), c_{B_2}(\mathbf{p}), c_{A_2}(\mathbf{p}), c_{B_1}(\mathbf{p}))$, such that the Hamiltonian becomes

$$\mathcal{H}_{\text{kin}} = \int \frac{d^2p}{(2\pi)^2} c^\dagger_a(\mathbf{p}) H_{ab}(\mathbf{p}) c_b(\mathbf{p}), \tag{2.12}$$

[4]Strictly speaking the term honeycomb lattice is a misnomer, what is meant by honeycomb lattice is a really a hexagonal lattice with a two-atom basis.

where the Bloch Hamiltonian is

$$H_{ab}(\mathbf{p}) = \begin{pmatrix} 0 & \gamma_3 \sum_i e^{-i\mathbf{p}\cdot\mathbf{l}_i} & 0 & \gamma_0 \sum_i e^{i\mathbf{p}\cdot\mathbf{l}_i} \\ \gamma_3 \sum_i e^{i\mathbf{p}\cdot\mathbf{l}_i} & 0 & \gamma_0 \sum_i e^{-i\mathbf{p}\cdot\mathbf{l}_i} & 0 \\ 0 & \gamma_0 \sum_i e^{i\mathbf{p}\cdot\mathbf{l}_i} & 0 & \gamma_1 \\ \gamma_0 \sum_i e^{-i\mathbf{p}\cdot\mathbf{l}_i} & 0 & \gamma_1 & 0 \end{pmatrix}. \tag{2.13}$$

We now expand the Bloch Hamiltonian for momenta $\mathbf{p} = \mathbf{K}_\xi + \mathbf{k}$ close to the K-points $\mathbf{K}_\xi = (\xi \frac{4\pi}{3\sqrt{3}a}, 0)$. $\xi = +1$ (-1) corresponds to the K (K') valley. The Hamiltonian becomes

$$\mathcal{H}_{\text{kin}} = \sum_\xi \int \frac{d^2k}{(2\pi)^2} c^\dagger_{\xi a}(\mathbf{k}) H_{\xi ab}(\mathbf{k}) c_{\xi b}(\mathbf{k}). \tag{2.14}$$

Here the integral over $\mathbf{k}$ runs over momenta near the K or K' valley with a cut-off $\Lambda \sim 2\pi/a$. We have moved from the UV-complete theory to a low-energy theory. The physical results will not depend on the cut-off since we consider the physics in the long wavelength limit where $k \ll \Lambda$. The explicit form of the Hamiltonian matrix is[79, 80, 81]

$$H_{\xi ab}(\mathbf{k}) = \begin{pmatrix} 0 & v_3(\xi k_x + i k_y) & 0 & v_F(\xi k_x - i k_y) \\ v_3(\xi k_x - i k_y) & 0 & v_F(\xi k_x + i k_y) & 0 \\ 0 & v_F(\xi k_x - i k_y) & 0 & \gamma_1 \\ v_F(\xi k_x + i k_y) & 0 & \gamma_1 & 0 \end{pmatrix}, \tag{2.15}$$

where the velocity v_3 is given by $v_3 = \frac{\sqrt{3}}{2} a\gamma_3/\hbar$ and the Fermi-velocity is given by $v_F = \frac{\sqrt{3}}{2} a\gamma_0/\hbar$. In the following, we will set $v_3 = 0$, since we are only interested in the quadratic bands. We are thus neglecting the trigonal warping, which is justified as long as the temperature is not too low (see Refs. [81, 79] for details). We also neglect additional effects such as the opening of an interaction induced gap [82], restricting the applicability of our approach to $T \gtrsim 10K$ [13].

2.3.2 Low energy effective Hamiltonian

Since the Hamiltonian (2.14) provides information about both high energy and low energy states, it will be useful to create a low-energy effective Hamiltonian. As shown in Fig. 2.5,

the bandstructure close to the K points consists of four parabolic bands, two of which are gapless. The gap to the higher energy bands is 0.4eV $\sim$ 4600K. In the temperature and density range relevant for the experiment[13] only the two low-energy bands that are gapless are relevant. To simplify our model, we consider only the low-energy bands near the two valleys. In the long wavelength limit $v_F k \ll \gamma_1$, one can derive

$$H_{\xi\alpha\beta}(\mathbf{p}) = -\frac{p^2}{2m}\begin{pmatrix} 0 & e^{-2i\xi\theta_{\mathbf{p}}} \\ e^{2i\xi\theta_{\mathbf{p}}} & 0 \end{pmatrix}, \qquad \mathcal{H}_{\text{kin}} = \sum_{\xi}\int \frac{d^2k}{(2\pi)^2} c^{\dagger}_{\xi\alpha}(\mathbf{k}) H_{\xi\alpha\beta}(\mathbf{k}) c_{\xi\beta}(\mathbf{k}), \tag{2.16}$$

where the effective mass is $m = \frac{\gamma_1}{2v_F^2} = 0.033 m_e$[83] and $\theta_{\mathbf{p}}$ is the angle between the vector $\mathbf{p}$ and the x-axis. We also have $c_\alpha(\mathbf{p}) = (c_{A_1}(\mathbf{p}), c_{B_2}(\mathbf{p}))$, which means that in the low energy limit, we only consider the electrons appearing at sites A_1 and B_2. Diagonalizing the Hamiltonian, we find

$$\mathcal{H}_{\text{kin}} = \sum_{\xi\lambda}\int \frac{d^2k}{(2\pi)^2}\epsilon_\lambda(\mathbf{k}) c^{\dagger}_{\lambda\xi}(\mathbf{k}) c_{\lambda\xi}(\mathbf{k}), \tag{2.17}$$

where the band energies are

$$\epsilon_\lambda(\mathbf{k}) = \frac{\lambda k^2}{2m} \tag{2.18}$$

and

$$c_{\lambda K}(\mathbf{k}) = \frac{1}{\sqrt{2}}\left(-\lambda e^{-2i\theta_{\mathbf{k}}} c_{K;A_1}(\mathbf{k}) + c_{K;B_2}(\mathbf{k})\right), \tag{2.19}$$

$$c_{\lambda K'}(\mathbf{k}) = \frac{1}{\sqrt{2}}\left(-\lambda e^{-2i\theta_{\mathbf{k}}} c_{K;B_2}(\mathbf{k}) + c_{K;A_1}(\mathbf{k})\right). \tag{2.20}$$

$\lambda = +1(-1)$ denotes electrons in the conduction (valence) band. We will often find it useful to think about electrons in the conduction band and holes in the valence band.

2.3.3 Interaction Hamiltonian

The interaction Hamiltonian will be

$$\mathcal{H}_{\text{int}} = \frac{1}{2}\int \frac{d^2q}{(2\pi)^2} V(\mathbf{q}) : \rho^{\text{eff}}(-\mathbf{q})\rho^{\text{eff}}(\mathbf{q}) :, \tag{2.21}$$

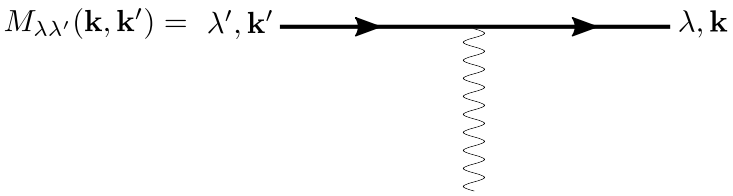

Figure 2.6: The BLG vertex coupling an electron to a photon. The initial (final) state of the electron is labelled by a band label λ' (λ) and has momentum $\mathbf{k}'$ ($\mathbf{k}$). The electron also has a flavour label specifying the spin and valley degrees of freedom which is suppressed in the diagram above. The vertex conserves the electron flavour.

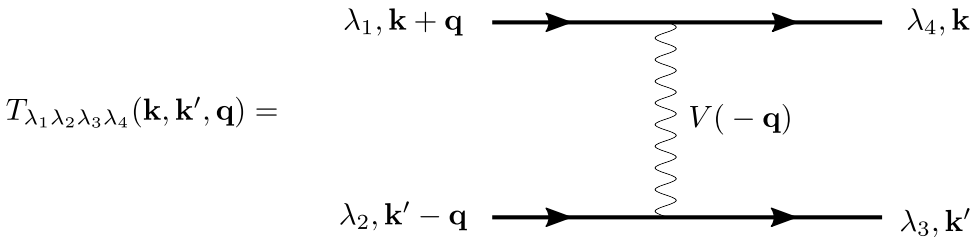

Figure 2.7: The BLG matrix element for two electrons interacting via the Coulomb interaction V. The state of the incoming and outgoing electrons has band and momentum labels $(\lambda, \mathbf{k})$ and the flavour label is suppressed. Both legs can have distinct fermion flavours.

where $V(\mathbf{q})$ is the screened Coulomb interaction and the two-dimensional electron density is given by

$$\rho^{\text{eff}}(\mathbf{q}) = \sum_{\xi} \int \frac{d^2k}{(2\pi)^2} c^{\dagger}_{\xi\alpha}(\mathbf{k}-\mathbf{q}) c_{\xi\alpha}(\mathbf{k}) \tag{2.22}$$

$$= \sum_{f} \int \frac{1}{2} \frac{d^2k}{(2\pi)^2} \sum_{\lambda,\lambda'} c^{\dagger}_{\lambda f}(\mathbf{k}-\mathbf{q}) c_{\lambda' f}(\mathbf{k}) \left(1 + \lambda\lambda' e^{-2i\left(\theta_{\mathbf{k}-\mathbf{q}} - \theta_{\mathbf{k}}\right)}\right), \tag{2.23}$$

where in the last line we have made spin index explicit via the flavour index f which takes into account the spin and valley degrees of freedom. In the following sections, we will omit the spin and valley indices for simplicity and include them back in the counting factors. There are two valleys (K and K') and two spin states in each valley, thus giving $N_f = 4$ flavors. From (2.22) we can read off the matrix element

$$M_{\lambda\lambda'}(\mathbf{k},\mathbf{k}') = \frac{1}{2}\left(1 + \lambda\lambda' e^{i(2\theta_{\mathbf{k}'} - 2\theta_{\mathbf{k}})}\right). \tag{2.24}$$

This corresponds to the vertex shown in Fig. 2.6. The matrix elements given by the

diagram (2.7) are

$$T_{\lambda_1\lambda_2\lambda_3\lambda_4}(\mathbf{k},\mathbf{k}',\mathbf{q}) = V(-\mathbf{q})M_{\lambda_1\lambda_4}(\mathbf{k}+\mathbf{q},\mathbf{k})M_{\lambda_2\lambda_3}(\mathbf{k}'-\mathbf{q},\mathbf{k}') \tag{2.25}$$

and hence the interaction Hamiltonian is

$$\mathcal{H}_{\text{int}} = \sum_{f,f'}\sum_{\lambda_i}\int \frac{d^2k}{(2\pi)^2}\frac{d^2k'}{(2\pi)^2}\frac{d^2q}{(2\pi)^2} T_{\lambda_1\lambda_2\lambda_3\lambda_4}(\mathbf{k},\mathbf{k}',\mathbf{q})\, c^\dagger_{\lambda_1 f'}(\mathbf{k}+\mathbf{q})\, c^\dagger_{\lambda_2 f}(\mathbf{k}'-\mathbf{q})\, c_{\lambda_3 f}(\mathbf{k}')\, c_{\lambda_4 f'}(\mathbf{k})\,. \tag{2.26}$$

Let us now consider the form of the interaction $V(\mathbf{q})$. Parabolic bands in two dimensions have a constant density of states, in particular there will be a finite density of states at CN, which will result in the Coulomb interaction being screened. This is in contrast to monolayer graphene, where the linear dispersion leads to a vanishing density of states at the Dirac point in which case the Coulomb interaction is unscreened. We use the form of the screened Coulomb potential valid in the experimentally-relevant regime $\beta\mu \lesssim 1$. The screened Coulomb potential is obtained via the random phase approximation (RPA)[76] as

$$V(q) = \frac{2\pi\alpha}{q + q_{TF}(q)}, \tag{2.27}$$

where $q = |\mathbf{q}|$. The Thomas–Fermi screening momentum is calculated according to the Lindhard formula which yields[84]

$$q_{TF}(q) \approx \alpha m N_f \left(1 + \frac{\beta q^2}{12m}\right), \tag{2.28}$$

where $\alpha = e^2/(4\pi\epsilon)$ is the electromagnetic fine structure constant multiplied by the speed of light and $\epsilon = \epsilon_0\epsilon_r$ is the permittivity. The typical momentum of an electron at temperature T is the thermal momentum $q_{\text{th}} = \sqrt{2mk_BT}$ and so

$$\frac{q_{\text{th}}}{q_{TF}(q=0)} \sim 0.02\epsilon_r\sqrt{T[\text{K}]/40}. \tag{2.29}$$

So for the temperature range $T \lesssim 40K$ and $\epsilon_r \sim 1$ for suspended samples, we have $q_{\text{th}} \ll q_{TF}$ and we can make the approximation $V(q) = \frac{2\pi}{N_f m}(1 + \frac{\beta q^2}{12m})^{-1}$. Note that the electromagnetic fine structure constant has dropped out when calculating the screened

potential.

2.4 The quantum Boltzmann equation

In equilibrium the occupancy of a state $(\lambda, \mathbf{p})$ is given by the usual Fermi factor

$$f_\lambda^0(\mathbf{p}) = \frac{1}{1 + e^{\beta(\epsilon_\lambda(\mathbf{p}) - \mu)}}, \tag{2.30}$$

where $\beta = 1/k_B T$ is the inverse temperature and μ is the chemical potential. We can distinguish two regimes

- $|\beta\mu| \gg 1$: This is the Fermi liquid regime where there is a well-defined Fermi surface and one type of charge carrier dominates.
- $|\beta\mu| \ll 1$: This is the regime near charge neutrality where both electrons and holes are thermally excited. This will be the regime of interest in this chapter.

The Boltzmann equation determines the change in occupancy of the $\mathbf{k}$ states due to small perturbations such as an external electric field $\mathbf{E}$ or temperature gradient ∇T.

Key Concept 2: The Boltzmann equation

The Boltzmann equation for the distribution function $f_\lambda(\mathbf{k}, \mathbf{x}, t)$ of electrons in band λ with charge $-e$ and dispersion $\epsilon_\lambda(\mathbf{k})$ is

$$\left(\frac{\partial}{\partial t} + \mathbf{v}_\lambda(\mathbf{k}) \cdot \frac{\partial}{\partial \mathbf{x}} - e\mathbf{E} \cdot \frac{\partial}{\partial \mathbf{k}}\right) f_\lambda(\mathbf{k}, \mathbf{x}, t) = -I_\lambda(\mathbf{k}, \mathbf{x}, t), \tag{2.31}$$

where the group velocity is defined as $\mathbf{v}_\lambda(\mathbf{k}) = \partial_{\mathbf{k}} \epsilon_\lambda(\mathbf{k})$ and $I_\lambda(\mathbf{k}, \mathbf{x}, t)$ is the collision integral.

The Boltzmann equation as written above can be applied to a variety of systems including classical gases (in which case the band label λ is replaced by a species label). The term quantum Boltzmann equation refers to applying the Boltzmann equation to a system of electrons or other quasiparticles arising in solid state systems. In that case, the distribution function is given by $f_\lambda(\mathbf{p}) = \langle c_\lambda^\dagger(\mathbf{p}) c_\lambda(\mathbf{p}) \rangle$. For BLG, the collision integral

consists of a sum of terms

$$I_\lambda(\mathbf{p}) = I_{\lambda,\text{e-e}}(\mathbf{p}) + I_{\lambda,\text{e-phonon}}(\mathbf{p}) + I_{\lambda,\text{e-impurity}}(\mathbf{p}) + I_{\lambda,\text{e-boundary}}(\mathbf{p}). \tag{2.32}$$

The first term in (2.32) accounts for the Coulomb scattering of electrons off each other. The second term describes the scattering of electrons off acoustic phonons. The third term describes scattering of electrons off impurities. The last term accounts for scattering of the electrons off the boundary of the necessarily finite-size sample. We will now discuss the form of the collision integral for each of these scattering mechanisms.

2.4.1 Coulomb scattering

We first consider Coulomb (electron-electron, electron-hole) scattering, which we expect to be dominant. There are two ways to derive the Coulomb scattering collision integral. The first, more rigorous method uses the non-equilibrium Keldysh formalism. The self-consistent Dyson equation is written down in the Keldysh basis and this leads to the so-called Kadanoff-Baym equations for the Green's function[85]. The second order Born approximation is used to evaluate the self-energy. The equation can then we re-written in the form of a QBE with the relevant collision integral. The details of this derivation for BLG are found in [20].

In this thesis we show how to motivate the form of the collision integral based on a more simple Fermi's Golden Rule calculation. The collision integral for scattering between electrons is

$$\begin{aligned} I_{\lambda,\text{e-e}}(\mathbf{p}) = -(2\pi) \sum_{\lambda_1\lambda_2\lambda_3} \int \frac{d^2\mathbf{k}}{(2\pi)^2}\frac{d^2\mathbf{q}}{(2\pi)^2} \delta(\epsilon_\lambda(\mathbf{p}) + \epsilon_{\lambda_1}(\mathbf{k}) - \epsilon_{\lambda_2}(\mathbf{p}+\mathbf{q}) - \epsilon_{\lambda_3}(\mathbf{k}-\mathbf{q})) \\ \times \left[N_f |T_{\lambda\lambda_1\lambda_3\lambda_2}(\mathbf{p},\mathbf{k},\mathbf{q})|^2 - T_{\lambda\lambda_1\lambda_3\lambda_2}(\mathbf{p},\mathbf{k},\mathbf{q}) T^*_{\lambda\lambda_1\lambda_2\lambda_3}(\mathbf{p},\mathbf{k},\mathbf{k}-\mathbf{p}-\mathbf{q})\right] \\ \times \Big[[1-f_\lambda(\mathbf{p})][1-f_{\lambda_1}(\mathbf{k})] f_{\lambda_2}(\mathbf{p}+\mathbf{q}) f_{\lambda_3}(\mathbf{k}-\mathbf{q}) \\ - f_\lambda(\mathbf{p}) f_{\lambda_1}(\mathbf{k})[1-f_{\lambda_2}(\mathbf{p}+\mathbf{q})][1-f_{\lambda_3}(\mathbf{k}-\mathbf{q})]\Big]. \end{aligned} \tag{2.33}$$

The collision integral $I_{\lambda,\text{e-e}}(\mathbf{p})$ describes the net rate at which electrons scatter into the state $(\lambda, \mathbf{p})$. The collision integral is a product of three pieces. The first term is a delta

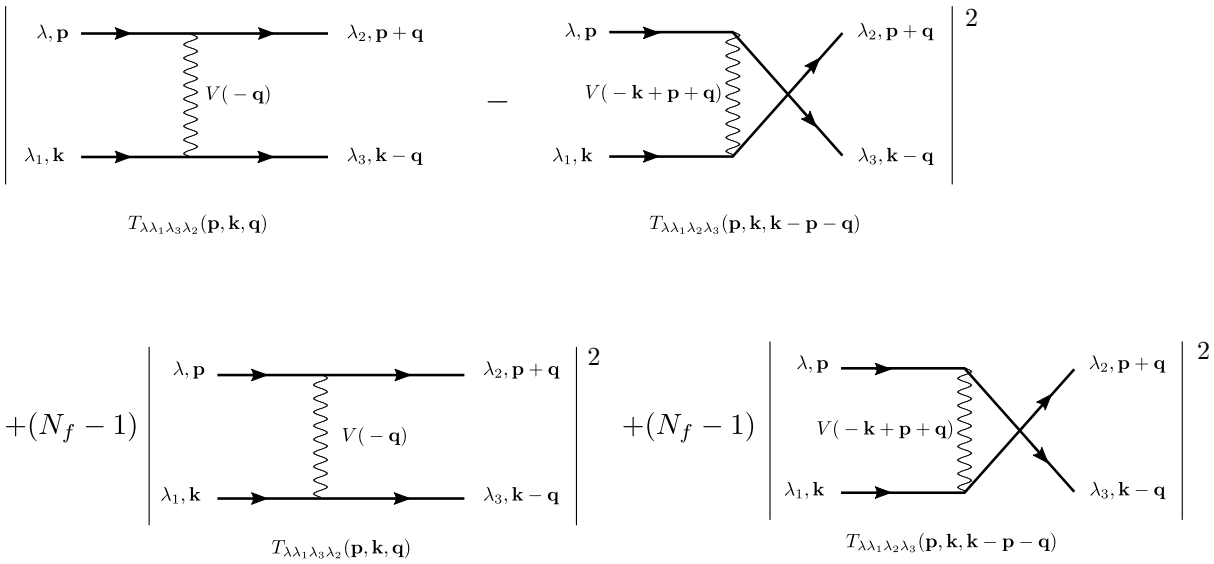

Figure 2.8: The diagrams entering the calculation of the collision integral. The top two diagrams have the same electron flavour on the two legs. The exchange diagram comes with a minus sign due to the fermion exchange. The bottom two diagrams have different electron flavours on the two legs and hence come with a factor of $(N_f - 1)$. $N_f = 4$ is the number of fermion species. We add the squares of the diagrams in the bottom line since the final states are distinguishable due to the different fermion flavours.

function that enforces energy conservation (momentum conservation is automatically satisfied via the definition of the momenta). The second term contains the matrix element for the scattering rate. The diagrams that enter the Golden Rule calculation are given by Fig. 2.8. Finally the last term contains the Fermi factors. For a scattering process to be possible, we require the two initial states to be occupied and the two final states to be unoccupied. The first product is for the case where an electron scatters into state $(\lambda, \mathbf{p})$ we subtract off the second product which is for the case where an electron scatters out of state $(\lambda, \mathbf{p})$.

As noted above, the electromagnetic fine-structure constant drops out when one uses the fully screened Coulomb potential. From a simple exercise in dimensional analysis, it is clear that at charge neutrality, the only scale in the problem that can set the electron-electron scattering rate is the temperature. Therefore, we find

$$\tau_{\text{e-e}}^{-1} = C\frac{k_B T}{\hbar}, \tag{2.34}$$

where C is a dimensionless constant. This type of scattering rate which only depends on

temperature is also known as *Planckian dissipation.* In fact

$$C \sim \frac{1}{N_f}, \tag{2.35}$$

where $N_f = 4$ is the number of fermion flavours. This can be easily seen by studying the collision integral (2.33), due to screening, the Coulomb interaction is $\propto 1/N_f$, in addition some of the diagrams come with a pre-factor N_f, giving us that the collision integral and hence the scattering rate for electron-electron interactions is $\propto 1/N_f$.

An important physical feature of this Coulomb collision integral is that it has a zero mode corresponding to momentum conservation. The collision integral vanishes for the case where we apply a Galilean boost to the Fermi distribution. In particular, the collision integral (2.33) vanishes for the Fermi distribution $f^0_\lambda(\mathbf{p})$ as well as for $f^0_\lambda(\mathbf{p}-\lambda m\mathbf{u})$, which corresponds to a Galilean boost by $\mathbf{u}$. This zero mode has electrons and holes moving in the same direction, and therefore always carries heat, and also carries charge as long as $|\mu| > 0$. This means that for the transport properties to be well defined, we need an additional mechanism to relax the heat and charge currents and this will be one of the momentum-relaxing mechanisms that we describe below. The only exception is the electrical conductivity at CN, which is well-defined even in the absence of momentum-relaxation since the zero mode does not carry charge at CN.

2.4.2 Impurity scattering

We consider Coulomb impurities, i.e. short-range point scatterers. Long-range charge disorder such as charge puddles are expected to be less important for suspended BLG. For this calculation, we put our system in a box of side length L with periodic boundary conditions. We consider a disorder Hamiltonian

$$H_{\text{dis}} = \int d^2\mathbf{x}\; V_{\text{dis}}(\mathbf{x})\rho^{\text{eff}}(\mathbf{x}), \tag{2.36}$$

where V_{dis} is the interaction potential between an electron and the impurities, which we take to be charges Ze located at random positions $\mathbf{x}_i$ and having number density

$n_{\text{imp}} = N_{\text{imp}}/L^2$. We use the screened Coulomb interactions to obtain

$$V_{\text{dis}}(\mathbf{x}) = \sum_{i=1}^{N_{\text{imp}}} \frac{Ze^2}{4\pi\epsilon|\mathbf{x}-\mathbf{x}_i|} e^{-q_{TF}|\mathbf{x}-\mathbf{x}_i|}. \tag{2.37}$$

From the interaction (2.36), we can calculate the scattering rate of quasi-particles off the disorder via a Golden Rule calculation [20]. We then obtain the impurity scattering rate

$$\tau^{-1}_{\text{e-impurities}} = \frac{1}{2} m n_{\text{imp}} \left(\frac{2\pi Ze^2}{\epsilon q_{TF}}\right)^2. \tag{2.38}$$

The contribution to the collision integral due to scattering off impurities is

$$I_{\lambda,\text{e-impurities}}(\mathbf{p}) = \frac{f_\lambda(\mathbf{p}) - f^0_\lambda(p)}{\tau_{\text{e-impurities}}}, \tag{2.39}$$

where the scattering rate has the temperature dependence

$$\tau^{-1}_{\text{e-impurities}} \propto T^0. \tag{2.40}$$

The form (2.39) of the collision integral is known as the *relaxation-time approximation*. As the name suggests, it will relax the distribution function to the equilibrium (Fermi) distribution function over a timescale $\tau_{\text{e-impurities}}$. In plasma physics, this is also known as the BGK (Bhatnagar-Gross-Krook) collision integral. Since we are working in the hydrodynamic regime, where the electron-electron scattering is the dominant scattering mechanism, we expect the relaxation time approximation to be valid for the subdominant scattering mechanism.

2.4.3 Phonon scattering

First of all, we are at low enough temperatures such that we only need to consider the acoustic phonons. We are left with three types of acoustic phonons: longitudinal acoustic (LA), transverse acoustic (TA) and out-of-plane (flexural) acoustic (FA). Now the the FA phonons only couple to the electrons at second order in the displacement, so we ignore them here[86]. The deformation potential of the TA phonons vanishes[87, 88]. Hence we

only need to consider the LA phonons.

The scaling of the phonon scattering rate will depend on which temperature regime we are in. In ordinary metals, the temperature scale that separates the high and low-temperature regime is the Debye temperature T_D. The Debye frequency is the maximum frequency of phonons. At temperatures above the Debye temperature, we have excited phonons of all possible frequencies and as we increase the temperature further, we simply increase the occupation of the phonon modes below the Debye frequency. This leads to a scattering rate $\propto T$. However, below the Debye temperature, two things happen as we increase the temperature. On the one hand we start exciting phonons with higher energies. On the other hand we increase the occupation number of the phonon modes that were already excited. These two effects lead to a higher power-law dependence of the scattering rate $\propto T^4$ ($\propto T^5$) for a two(three)-dimensional metal. For graphene, the Debye temperature is $T_D \sim 1800$K[89] and so the experimentally relevant regime is well below T_D, so naively one might expect a T^4 power law dependence.

However for materials with low electron densities such as bilayer graphene near charge neutrality the situation is slightly different. There is still a crossover between a high and low temperature scaling of the electron-phonon scattering rate, but it is set by the so-called *Bloch–Grüneisen temperature* T_{BG} instead of the Debye temperature. Due to the low electron density, the electrons have small momenta. So as we increase the temperature above the Bloch–Grüneisen temperature, the highest energy phonons have momenta $k_{\max} \sim k_B T_{\mathrm{BG}}/c_s$ (c_s is the speed of sound in graphene) which is too large to scatter electrons. The maximum momentum of the electron is set either by the Fermi momentum k_F (if $\beta\mu > 1$) or the thermal momentum q_{th} (if $\beta\mu < 1$). Since we are interested in the latter regime in our work, the Bloch–Grüneisen temperature will be set by the condition[5]

$$\frac{k_B T_{\mathrm{BG}}}{c_s} = q_{\mathrm{th}} = \sqrt{2mk_B T_{\mathrm{BG}}}. \tag{2.41}$$

With $c_s = 2 \times 10^4$m/s[90], we find $T_{\mathrm{BG}} = 3.4$K. The experiment is at temperatures above the Bloch–Grüneisen temperature and hence the longitudinal acoustic phonons have a

[5]We note that the Bloch–Grüneisen temperature is usually defined in the Fermi liquid regime, in which case $\frac{k_B T_{\mathrm{BG}}}{c_s} = k_F$. In our analysis we have modified this expression such that it is appropriate to the regime near CN.

scattering time [90, 88]

$$\tau^{-1}_{\text{e-phonon}} = \frac{D^2 m k_B T}{2\rho c_s^2}, \tag{2.42}$$

where D is the deformation potential and ρ is the mass density of BLG. D is not known with a high accuracy a priori since it varies from experiment to experiment, it is expected to be in the range $10 - 30\text{eV}$[91, 92, 93, 94, 95]. The contribution to the collision integral due to scattering off phonons is

$$I_{\lambda,\text{e-phonon}}(\mathbf{p}) = \frac{f_\lambda(\mathbf{p}) - f^0_\lambda(p)}{\tau_{\text{e-phonon}}}, \tag{2.43}$$

where the scattering rate has the temperature dependence

$$\tau^{-1}_{\text{e-phonon}} \propto T^1. \tag{2.44}$$

2.4.4 Scattering off the boundary

In very clean samples of bilayer graphene, it is expected that the scattering length due to impurity scattering is longer than the system size L, which is currently limited in suspended graphene samples to be $L \lesssim 1\mu\text{m}$[96]. There will be scattering of the electrons off the boundary, which effectively acts as an additional momentum-relaxing scattering time. Assume the typical scattering time due to collisions with the boundary is

$$\tau_{\text{e-boundary}} = \frac{L}{v_{\text{th}}}, \tag{2.45}$$

where L is the size of the sample and

$$v_{\text{th}} \sim \sqrt{\frac{k_B T}{m}} \tag{2.46}$$

is the thermal velocity, i.e. the typical velocity of an electron at temperature T. Here, we are making the simplifying assumption that the boundary scattering time does not depend on the momentum of the electrons. The contribution to the collision integral due

to scattering off the boundary is

$$I_{\lambda,\text{e-boundary}}(\mathbf{p}) = \frac{f_\lambda(\mathbf{p}) - f^0_\lambda(p)}{\tau_{\text{e-boundary}}}, \tag{2.47}$$

where the scattering rate has the temperature dependence

$$\tau^{-1}_{\text{e-boundary}} \propto T^{1/2}. \tag{2.48}$$

2.4.5 Umklapp scattering

It is in fact possible to get a finite conductivity purely from electron-electron collisions. In two-body electron-electron collisions, crystal momentum is conserved, however this does not necessarily mean the momentum is conserved. The momentum of the electrons can change by a reciprocal lattice vector. For a Fermi liquid, if Umklapp scattering is present, it has a scattering rate $\tau^{-1}_{\text{Umklapp}} \propto T^2$ (intuitively this scaling comes from the fact that we need the electrons to be within a shell $k_B T$ of the Fermi surface and we have two electrons in a collision). This leads to a resistivity $\rho \propto T^2$, which has indeed been observed experimentally for very clean Fermi liquids [97].

In the present case however, we are interested in graphene near charge neutrality i.e. far from the Fermi liquid regime and therefore Umklapp scattering is very weak. Electrons have typical momenta which satisfy $ka \ll 1$, where a is the lattice constant and therefore Umklapp scattering processes with $q \sim 1/a$ will be highly suppressed due to the $1/q$ scaling of the Coulomb interaction.

2.5 Validity of the semiclassical approach

The Boltzmann equation as formulated in the section above is a fundamentally semiclassical approach. It relies on a valid quasiparticle description of the system, which will clearly break down in the case of strong enough interactions. So the question is, what small paramater in this problem justifies the semiclassical approach?

For a valid quasiparticle description to hold, we want the mean free path of the electrons to be large compared to the de Broglie wavelength of the electrons. In the

hydrodynamic regime, the mean free path of the electrons will be set by the electron-electron scattering rate $\tau_{\rm mc}^{-1}$.

Remember that

$$\tau_{\rm mc}^{-1} = C\frac{k_B T}{\hbar} \sim \frac{1}{N_f}\frac{k_B T}{\hbar}. \tag{2.49}$$

Close to charge neutrality, the temperature will set the typical velocity of an electron and hence the mean free path of electrons is

$$\lambda_{\rm mfp} \sim v_{\rm th}\tau_{\rm mc}. \tag{2.50}$$

On the other hand the typical size of the de Broglie wavelength is set by the thermal wavelength

$$\lambda_{\rm th} \sim \frac{\hbar}{m v_{\rm th}}. \tag{2.51}$$

The ratio of these two length scales is therefore

$$\frac{\lambda_{\rm th}}{\lambda_{\rm mfp}} \sim C \sim \frac{1}{N_f} \ll 1 \tag{2.52}$$

and so as desired, the mean free path is long compared to the wavelength of the electrons. The small parameter that justifies our semiclassical analysis is $\frac{1}{N_f}$ where the number of fermion flavours is $N_f = 4$ for BLG.

2.6 Two-fluid model

Before we solve the QBE, let us develop some further intuition for this problem. If Coulomb scattering is dominant we expect a hydrodynamic description will be appropriate[98, 99, 100, 101, 102, 103, 104]. Further, since the scattering between electrons and holes is suppressed due to both matrix element effects and energy-momentum conservation constraints[76], we believe treating the electron fluid and the hole fluids as weakly interacting with each other will be accurate. In this limit, due to the strong scattering within each species, each of the two fluids should have a well defined temperature, chemical potential, and velocity. We thus introduce a two-fluid model [105, 106, 107, 108], which

shows excellent agreement with our detailed numerical calculation[6]. This simplification allows intuitive understanding of the physics that is not otherwise possible.

We start with the Boltzmann equation (2.31) with collision integral (2.32). We then multiply the Boltzmann equation by $\lambda\mathbf{p}/m$ and integrate over momentum space in order to derive the fluid equations.

Key Concept 3: The two-fluid model

The two-fluid model consists of two coupled equations for the evolution of the mean fluid velocities $\mathbf{u}^e$ and $\mathbf{u}^h$ of the electron and hole fluids respectively:

$$m\partial_t \mathbf{u}^e = -\frac{m}{\tau_{\text{e-h}}}(\mathbf{u}^e - \mathbf{u}^h) - \frac{m\mathbf{u}^e}{\tau_{\text{mr}}} - e\mathbf{E} - \Lambda^e k_B \nabla T \tag{2.53}$$

$$m\partial_t \mathbf{u}^h = \frac{m}{\tau_{\text{h-e}}}(\mathbf{u}^e - \mathbf{u}^h) - \frac{m\mathbf{u}^h}{\tau_{\text{mr}}} + e\mathbf{E} - \Lambda^h k_B \nabla T, \tag{2.54}$$

where τ_{mr} is the scattering time for momentum-relaxing collisions. $\tau_{\text{e-h}}$ is the scattering time of electrons by holes and $\tau_{\text{h-e}}$ is the scattering time of holes by electrons. $\Lambda^e(\Lambda^h)$ is the heat capacity per particle for an electron (hole), for which we provide detailed expressions in App. B.

The first term on the right-hand side (RHS) of (2.53) and (2.54) is the Coulomb drag term. This is a viscous term[7] via which the electron and the hole fluid can exchange momentum, while the total momentum of electrons plus holes is conserved. The second term on the RHS is a Drude-like term that allows for momentum-relaxation. The last two terms on the RHS are the driving terms due to the applied electric field and thermal gradients respectively.

We consider the steady state $\partial_t \mathbf{u}^e = \partial_t \mathbf{u}^h = 0$ and solve the fluid equations (2.53) and (2.54) for $\mathbf{u}^e$ and $\mathbf{u}^h$. Using these solutions, we calculate the electric current

$$\mathbf{J} = -e(n^e \mathbf{u}^e - n^h \mathbf{u}^h). \tag{2.55}$$

[6] We note that the two-fluid model is equivalent to performing the Spitzer-Härm calculation of Sec. 2.7 with two basis functions.

[7] We can also imagine adding viscous terms for the individual fluid components, viz. $\eta_e \nabla^2 \mathbf{u}^e$ and $\eta_h \nabla^2 \mathbf{u}^h$. Since we compute the transport properties for a spatially invariant system, these terms will not be relevant.

The number densities calculated from the Fermi distribution are

$$n^e = \frac{N_f m}{2\pi\beta}\ln\bigl(1+e^{\beta\mu}\bigr), \qquad n^h = \frac{N_f m}{2\pi\beta}\ln\bigl(1+e^{-\beta\mu}\bigr). \tag{2.56}$$

The heat current is given by

$$\mathbf{Q} = k_B T(\Lambda^e n^e \mathbf{u}^e + \Lambda^h n^h \mathbf{u}^h). \tag{2.57}$$

We define the electrical conductivity σ, the thermal conductivity K and the thermoelectric coefficient Θ via

$$\begin{pmatrix}\mathbf{J}\\ \mathbf{Q}\end{pmatrix} = \begin{pmatrix}\sigma & \Theta\\ T\Theta & K\end{pmatrix}\begin{pmatrix}\mathbf{E}\\ -\nabla T\end{pmatrix}. \tag{2.58}$$

The open circuit thermal conductivity [8] which is usually measured in experiments is given by $\kappa = K - T\Theta\sigma^{-1}\Theta$. We find the expressions

$$\sigma = \frac{e^2}{m(\tau_{\rm mr}^{-1}+\tau_{\rm e\text{-}h}^{-1}+\tau_{\rm h\text{-}e}^{-1})}\Bigl(n^e + n^h + \tau_{\rm mr}(\tau_{\rm h\text{-}e}^{-1}-\tau_{\rm e\text{-}h}^{-1})(n^e-n^h)\Bigr), \tag{2.59}$$

$$\Theta = \frac{-ek_B}{m(\tau_{\rm mr}^{-1}+\tau_{\rm e\text{-}h}^{-1}+\tau_{\rm h\text{-}e}^{-1})}\Bigl(n^e\tilde{\Lambda}^e - n^h\tilde{\Lambda}^h\Bigr), \tag{2.60}$$

$$K = \frac{k_B^2 T}{m(\tau_{\rm mr}^{-1}+\tau_{\rm e\text{-}h}^{-1}+\tau_{\rm h\text{-}e}^{-1})}\Bigl(\Lambda^e n^e\tilde{\Lambda}^e + \Lambda^h n^h\tilde{\Lambda}^h\Bigr), \tag{2.61}$$

where

$$\tilde{\Lambda}^e = \Lambda^e(1+\tau_{\rm mr}\tau_{\rm h\text{-}e}^{-1}) + \Lambda^h\tau_{\rm mr}\tau_{\rm e\text{-}h}^{-1}, \tag{2.62}$$

$$\tilde{\Lambda}^h = \Lambda^h(1+\tau_{\rm mr}\tau_{\rm e\text{-}h}^{-1}) + \Lambda^e\tau_{\rm mr}\tau_{\rm h\text{-}e}^{-1}. \tag{2.63}$$

For momentum conservation we require

$$n^e\tau_{\rm e\text{-}h} = n^h\tau_{\rm h\text{-}e}. \tag{2.64}$$

[8] κ measures the heat current in the absence of electrical current.

We verify explicitly that the Onsager relations for the thermoelectric coefficients are satisfied if equation (2.64) is satisfied. Thus we can choose

$$\tau_{\text{e-h}} = \tau_{\text{mc}} \frac{n^e + n^h}{n^h}, \qquad \tau_{\text{h-e}} = \tau_{\text{mc}} \frac{n^e + n^h}{n^e}, \tag{2.65}$$

where τ_{mc} is a function that only weakly depends on $\beta\mu$. In the limit $\tau_{\text{mr}} \gg \tau_{\text{mc}}$ we find the simpler expressions

$$\sigma = \frac{e^2}{m}\left(\tau_{\text{mc}}(n^e + n^h) + \tau_{\text{mr}} \frac{(n^e - n^h)^2}{n^e + n^h}\right), \tag{2.66}$$

$$\Theta = -\frac{2\pi e k_B^2 T}{3} \tau_{\text{mr}} \frac{n^e - n^h}{n^e + n^h}, \tag{2.67}$$

$$K = \frac{4\pi^2}{9} \frac{m k_B^2 T}{\beta^2 (n^e + n^h)} \tau_{\text{mr}}. \tag{2.68}$$

In deriving the above equation we have made use of the identity

$$n^e \Lambda^e + n^h \Lambda^h = \frac{2\pi}{3} \frac{m}{\beta}, \tag{2.69}$$

which can be proven from the explicit integral expressions for $\Lambda^{e,h}$.

2.6.1 Transport at charge neutrality

At charge neutrality we have an equal number density of electrons and holes. If we apply a thermal gradient, we will have electrons and holes travelling in the same direction at the same speed. We call this the *finite momentum mode*. In the language of the two-fluid model $\mathbf{u}^e = \mathbf{u}^h$. The Coulomb drag between electrons and holes will vanish in this mode and the thermal conductivity will be limited by the momentum relaxing scattering. Another way to say this is that momentum is conserved by the electron-electron scattering and hence the finite momentum-mode is long lived and is only relaxed on the slow time scale τ_{mr}.

On the other hand, when we apply an electric field we have electrons and holes moving in opposite directions at the same speed. We call this the *zero momentum mode*. In the

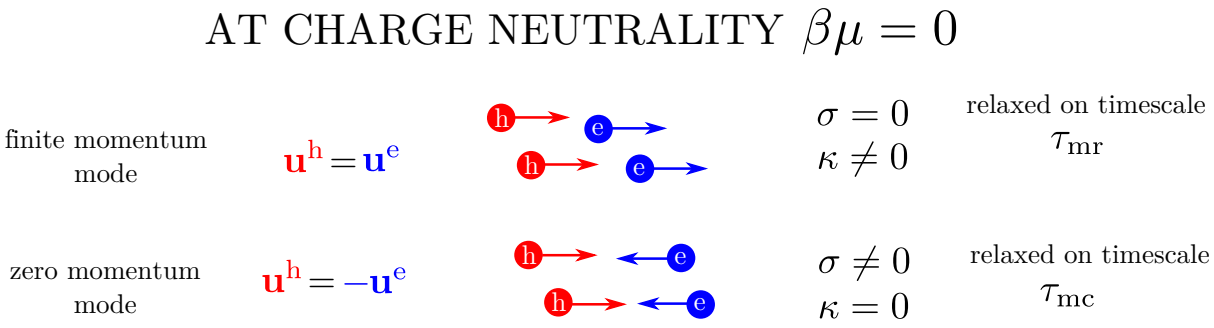

Figure 2.9: At CN the charge density of electrons and holes is equal. Therefore, the finite momentum mode with electrons and holes moving in the same direction carries heat, but no charge. This mode is relaxed on the slow timescale τ_{mr}. The zero-momentum mode with electrons and holes moving in opposite directions carries charge but no heat. This mode is relaxed on the fast timescale τ_{mc}.

language of the two-fluid model $\mathbf{u}^e = -\mathbf{u}^h$. Since this mode has no momentum associated with it, it can be relaxed on the fast timescale τ_{mc}. The electrical conductivity will hence be limited by the Coulomb drag between electrons and holes.

This is summarized in Fig. 2.9. Therefore, the electrical conductivity is suppressed compared to the thermal conductivity in the hydrodynamic regime where electron-electron scattering dominates, leading to a large Lorenz number $\mathcal{L} \equiv \kappa/(\sigma T)$. From the two-fluid model we can show that

$$\frac{\mathcal{L}(\beta\mu = 0)}{\mathcal{L}_{\mathrm{WF}}} \sim \frac{\tau_{\mathrm{mc}}^{-1}}{\tau_{\mathrm{mr}}^{-1}} \gg 1. \tag{2.70}$$

The violation of the Wiedemann–Franz law for BLG has been previously pointed out by [75] and has been experimentally observed for monolayer graphene in [54].

2.6.2 Transport away from charge neutrality

Away from charge neutrality both the zero-momentum and the finite momentum mode carry both heat and charge. Since the finite-momentum mode carries charge now and is relaxed on the slow time scale τ_{mr}, the electrical conductivity will increase sharply away from charge neutrality. We can show from the two fluid model that

$$\frac{\sigma(\beta\mu = 1)}{\sigma(\beta\mu = 0)} \sim \frac{\tau_{\mathrm{mc}}^{-1}}{\tau_{\mathrm{mr}}^{-1}} \gg 1. \tag{2.71}$$

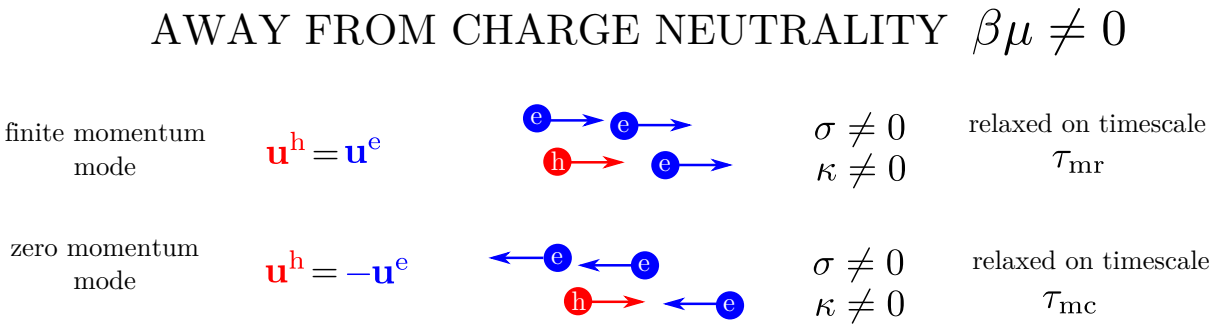

Figure 2.10: For $\mu > 0$ there is a larger density of electrons than holes. Therefore, both the finite momentum mode and the zero momentum mode carry both charge and heat.

2.7 Solving the quantum Boltzmann equation

Now that we have the intuition from the two-fluid model for the transport properties in BLG, we solve the QBE to confirm our expectations and to make a quantitative comparison with experiment. To calculate the quantum transport coefficients, we solve the QBE equation in the perturbed background to obtain the perturbation of the distribution function $f_\lambda(\mathbf{k})$ and then use the result to derive the linear response. The distribution function is expanded as

$$f_\lambda(\mathbf{p}) = f^0_\lambda(\mathbf{p}) + f^0_\lambda(\mathbf{p})[1 - f^0_\lambda(\mathbf{p}))]h_\lambda(\mathbf{p}) \tag{2.72}$$

about the equilibrium Fermi distribution. Assuming a steady state and a spatially uniform distribution function, the linearized quantum Boltzmann equation can then be derived to be

$$-I^{(1)}_\lambda(\mathbf{p}) = -\frac{\lambda\beta}{m} f^0_\lambda(\mathbf{p})[1 - f^0_\lambda(\mathbf{p})]\Big(- e\mathbf{E}\cdot\mathbf{p} - \frac{1}{T}\nabla T\cdot\mathbf{p}(\epsilon_\lambda(\mathbf{p}) - \mu)\Big)h_\lambda(\mathbf{p}), \tag{2.73}$$

where $\mathbf{E}$ is the electric field and ∇T is the thermal gradient. The collision integral will be a sum of terms $I^{(1)}_\lambda(\mathbf{p}) = I^{(1)}_{\lambda,\text{e-e}}(\mathbf{p}) + I^{(1)}_{\lambda,\text{mr}}(\mathbf{p})$. Linearizing the Coulomb collision integral

(2.33) using (2.72) we find

$$
\begin{aligned}
I^{(1)}_{\lambda,\text{e-e}}(\mathbf{p}) = -(2\pi) \sum_{\lambda_1\lambda_2\lambda_3} \int \frac{\mathrm{d}^2\mathbf{k}}{(2\pi)^2} \frac{\mathrm{d}^2\mathbf{q}}{(2\pi)^2} \delta(\epsilon_\lambda(\mathbf{p}) + \epsilon_{\lambda_1}(\mathbf{k}) - \epsilon_{\lambda_2}(\mathbf{p}+\mathbf{q}) - \epsilon_{\lambda_3}(\mathbf{k}-\mathbf{q})) \\
\times \Big[N_f |T_{\lambda\lambda_1\lambda_3\lambda_2}(\mathbf{p},\mathbf{k},\mathbf{q})|^2 - T_{\lambda\lambda_1\lambda_3\lambda_2}(\mathbf{p},\mathbf{k},\mathbf{q}) T^*_{\lambda\lambda_1\lambda_2\lambda_3}(\mathbf{p},\mathbf{k},\mathbf{k}-\mathbf{p}-\mathbf{q}) \Big] \\
\times \Big[[1 - f^0_\lambda(\mathbf{p})][1 - f^0_{\lambda_1}(\mathbf{k})] f^0_{\lambda_2}(\mathbf{p}+\mathbf{q}) f^0_{\lambda_3}(\mathbf{k}-\mathbf{q}) \Big] \\
\times \Big[- h_\lambda(\mathbf{p}) - h_{\lambda_1}(\mathbf{k}) + h_{\lambda_2}(\mathbf{p}+\mathbf{q}) + h_{\lambda_3}(\mathbf{k}-\mathbf{q}) \Big].
\end{aligned} \tag{2.74}
$$

We can easily read off the zero mode $h_\lambda(\mathbf{p}) = \beta \mathbf{p} \cdot \mathbf{u}$. We also have

$$
I^{(1)}_{\lambda,\text{mr}}(\mathbf{p}) = \frac{f^0_\lambda(\mathbf{p})[1 - f^0_\lambda(\mathbf{p}))] h_\lambda(\mathbf{p})}{\tau_{\text{mr}}}. \tag{2.75}
$$

We obtain the solution to the QBE by expanding $h_\lambda(\mathbf{p})$ in a set of basis functions, which then reduces the QBE to a set of linear equations which can be numerically solved. The size of the basis set is then expanded to convergence[109, 74, 73, 72]. This method of solution for the Boltzmann equation is well-known in the plasma physics community and goes by the name Spitzer-Härm method [110]. Details of the method of solution are presented in detail in Appendix A and Ref. [76]. Once we have solved the QBE, we calculate the electrical current

$$
\mathbf{J} = -\frac{e}{m} N_f \sum_\lambda \int \frac{d^2\mathbf{p}}{(2\pi)^2} \lambda \mathbf{p} f_\lambda(\mathbf{p}) \tag{2.76}
$$

and the heat current[9]

$$
\mathbf{Q} = N_f \sum_\lambda \int \frac{d^2k}{(2\pi)^2} \frac{\lambda \mathbf{k}}{m} \left(\epsilon_\lambda(\mathbf{k}) - \mu\right) f_\lambda(\mathbf{k}). \tag{2.77}
$$

From this we can determine the electrical conductivity σ, the thermal conductivity K and the thermo-electric coefficient Θ from (2.58).

[9] We note that the interactions may also contribute the energy current. However, we show that at least at mean-field level this can be absorbed into a shift of the chemical potential[20]. In a more careful analysis one can view this contribution as the heat carried by plasmons[111].

2.7.1 Electrical transport

In the experimental data[13], the electrical conductivity is measured as a function of number density for different temperatures. It is found that to a good approximation the conductivity only depends on the dimensionless combination $\beta\mu$ (see Fig. 2.11) and not separately on temperature. A priori it is not obvious why this should be the case. If only Coulomb interactions are included then $\beta\mu$ is the only dimensionless parameter of the problem (the electromagnetic fine-structure constant cancels out when the screened potential is used). However, away from charge neutrality (CN), the *finite momentum mode* carries electrical current and is not relaxed by Coulomb scattering since it conserves momentum. Thus, to obtain a finite conductivity, another scattering mechanism that relaxes momentum must be considered. We identified three possible such mechanisms: Impurity scattering, scattering off the boundary of the finite-size sample, and phonons. This additional scattering mechanism can introduce an additional temperature dependence.

From (2.71), if we want $\sigma(\beta\mu = 1)/\sigma(\beta\mu = 0)$ to only depend on $\beta\mu$ and not on temperature separately, we need $\tau_{\text{mc}}^{-1}/\tau_{\text{mr}}^{-1}$ to not depend on temperature.

Key Concept 4: Temperature scaling of scattering mechanisms

Recall the scaling with temperature of the different scattering mechanisms we discussed in Sec. 2.4:

1. electron-electron: $\tau_{\text{e-e}}^{-1} \propto T$
2. electron-impurity: $\tau_{\text{e-impurity}}^{-1} \propto T^0$
3. electron-phonon: $\tau_{\text{e-phonon}}^{-1} \propto T$
4. electron-boundary: $\tau_{\text{e-boundary}}^{-1} \propto T^{1/2}$

We have

$$\tau_{\text{mc}}^{-1} = \tau_{\text{e-e}}^{-1}. \tag{2.78}$$

By evaluating the collision integral in (2.33) at CN numerically (see App. A for details),

we find that the timescale τ_{mc} for electron-electron scattering defined in (2.65) is

$$\beta\tau_{\text{mc}}^{-1} = 0.15. \tag{2.79}$$

Recall from Sec. 2.5 that we expected this quantity to be $\sim 1/N_f$. The momentum-relaxing timescale is

$$\tau_{\text{mr}}^{-1} = \tau_{\text{e-phonon}}^{-1} + \tau_{\text{e-impurity}}^{-1} + \tau_{\text{e-boundary}}^{-1}. \tag{2.80}$$

From the scaling of the scattering rates with temperature, it is clear that for $\tau_{\text{mc}}^{-1}/\tau_{\text{mr}}^{-1}$ to be independent of temperature, electron-phonon scattering must be the dominant source of scattering. We emphasize the surprising result that even at these comparatively low temperatures of $12-40$K, phonons provide the primary momentum relaxation mechanism.

We are explaining the scaling collapse of the electrical conductivity when plotted as a function of $\beta\mu$ as a consequence of the electron-phonon scattering being the dominant source of momentum-relaxation for the electrons. However, an alternative explanation has been suggested by Ref. [112]. In that work, the authors argue that the ground state of suspended bilayer graphene has an interaction-induced gap. It is argued that the presence of this gap modifies the transport properties in a way that one still obtains a scaling collapse of the electrical conductivity even when the dominant source of momentum-relaxation is provided by electron-impurity collisions. This explanation relies on having charge-puddle disorder, which can be thought of as a position-dependent chemical potential.

The electrical conductivity σ depends on the dimensionless number $\beta\mu$ and on τ_{mr}. A non-zero $\tau_{\text{mr}} = \tau_{\text{e-phonon}}$ makes the conductivity finite and, as mentioned above, the curves for different temperatures approximately collapse when plotted as a function of $\beta\mu$. We treat the deformation potential D as a fit parameter being that various different approaches have given different estimates of this quantity[91, 92, 93, 94, 95]. By fitting our QBE results to the experimental data we extracted $\beta\tau_{\text{e-phonon}}^{-1} = 0.03$.Comparing to (2.79) we find that $\tau_{\text{e-phonon}}^{-1} \ll \tau_{\text{mc}}^{-1}$ which means that the scattering rate due to electron-electron collisions dominates over the electron-phonon scattering. This justifies the use of the hydrodynamic theory. Our best fit value for $\tau_{\text{e-phonon}}^{-1}$ corresponds to $D \approx 27$eV, which is consistent with prior expectation that it lies in the range $10 - 30$eV. Including

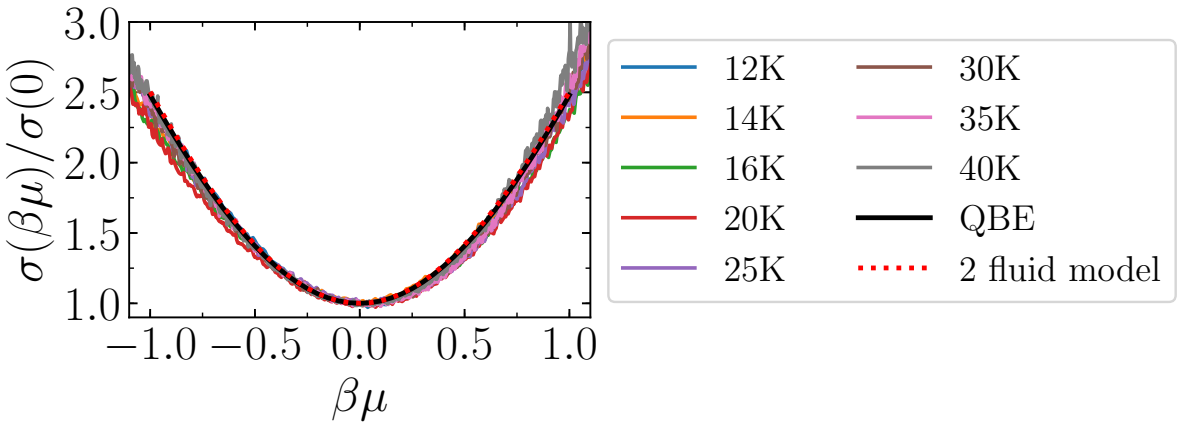

Figure 2.11: Electrical conductivity $\sigma(\beta\mu)$ for different values of the temperature. From the experimental data, we fit the value $\tau^{-1}_{\text{e-phonon}}$. The experimental data is from [13]. The black solid curve is the result of the QBE calculation. The black dashed curve shows the result from the two-fluid model and shows good agreement with the full QBE calculation (the two lines are almost indistinguishable).

the effect of finite size (boundary scattering) reduces the phonon scattering required to match the experiment. Taking account of the fact that the typical size of the system is around $3\mu m$, and there will be additional momentum-relaxing scattering off the boundary of the sample, the best fit D may be reduced by around 30%. In Fig. 2.11 we show σ as a function of $\beta\mu$. We show both the result of QBE calculation using the above discussed fit value of D as well as the experimental data from Ref. [13]. The thermal density of electrons (holes) for the free Fermi gas is given by (2.56) and as we increase $|\beta\mu|$ there are more charge carriers. However the total number density of electrons plus holes only increases by 17% between $|\beta\mu| = 0$ and 1 (at fixed T). Instead, the main contribution for the increase of the electrical conductivity away from CN comes from the finite momentum mode kicking in. We also note the good agreement of the QBE calculation and the two-fluid model.

At CN we get a finite electrical conductivity even in the absence of momentum-relaxation. Exactly at CN, we can compare our prediction for the magnitude of σ to prior calculations by Ref. [74]. Our work differs in three respects from Ref. [74]. Firstly, they take the screening wavevector q_{TF} to be constant, secondly they do not make the approximation $q_{TF} \gg q$ in the screened potential and thirdly they have not included all the second order diagrams for BLG. In order to compare our work, we ignore the momentum-

relaxing scattering mechanisms since Ref. [74] does not include those and the conductivity is well-defined without them at CN. Ref. [74] finds $\sigma(\mu = 0) = \frac{e^2}{h}(27.4 + 0.353\sqrt{T[\mathrm{K}]})$, which has a large constant piece and a smaller piece that depends on temperature. On the other hand, from dimensional analysis, in a clean system our result at CN does not depend on temperature. This discrepancy arises from making the approximation $q_{TF} \gg q$. However, in an experimental setting, the contributions arising from momentum-relaxing scattering will be the most significant for the temperature dependence, justifying our approximation.

The electron and hole densities at CN are

$$n^e = n^h = \frac{N_f m}{2\pi\beta}\ln(2). \tag{2.81}$$

The expression for the conductivity (2.66) becomes

$$\sigma(\mu = 0) = \frac{e^2\tau_{\mathrm{mc}}}{m}(n^e + n^h) \approx 36.9\frac{e^2}{h} \tag{2.82}$$

using result (2.79) and we have exceptionally restored Planck's constant h. In particular, we note that $\sigma(\mu = 0)$ is independent of temperature, which is consistent with experiments[13, 113]. In [13], in three of four samples, $\sigma(\mu = 0)$ does not vary more than about 10% over the full range of measured temperatures $10 - 100$K.

We can also compare our results to those in Ref. [75], which analyses the QBE for BLG. We note that Ref. [75] includes only the direct terms in the collision integral, however the effect of the exchange terms is small, justifying their approach. A further difference between our work and Ref. [75] is that we use the full momentum-dependent screening wavevector. Overall, we find qualitative agreement with that work.

2.7.2 Thermal transport

Including only Coulomb scattering, the thermal conductivity K diverges since the finite momentum mode carries thermal current and cannot be relaxed by Coulomb interactions. Phonons again regulate this divergence. One might expect that the thermal conductivity increases with increasing $|\beta\mu|$ since the total heat transport carrier den-

sity $n^e + n^h$ increases. However, we note that K actually decreases with increasing $|\beta\mu|$ which is counter-intuitive. In the limit of weak phonon scattering we will see below that $K \sim 1/(n^e + n^h)$. The open circuit thermal conductivity κ, plotted in Fig. 2.12 (top), decreases faster than K away from CN since the momentum mode carries electric current and hence does not contribute to κ. The thermoelectric coefficient Θ plotted in Fig. 2.12 (bottom) vanishes at CN and increases as we increase $\beta\mu$, as the momentum mode now carries both heat and charge. Using the value of $\tau_{\rm mr}^{-1} = \tau_{\text{e-phonon}}^{-1}$ extracted from the experiment, we find $\mathcal{L}(\beta\mu = 0) \approx 25(k_B/e)^2$ which is much larger than the value of $\pi^2/3(k_B/e)^2$ predicted by the Wiedemann–Franz law.

We note that we only consider the electronic contribution to the thermal transport. Phonons also carry heat. In order to detect hydrodynamic signatures, one therefore has to separate out the phonon contribution from the electronic contribution. In an experimental tour-de-force, this was achieved by heating only the electronic fluid of monolayer graphene while keeping the temperature of the lattice fixed and indeed a Wiedemann–Franz law violation was observed[54].

2.7.3 Comparison to two-fluid model

In Figs. 2.11 and 2.12 we also compare the results from the QBE and the two-fluid model. For the electrical conductivity and the thermopower the agreement is extremely good, whereas for the thermal conductivity we note a slight quantitative disagreement. This can be traced back to the fact that the two-fluid model only includes the first momentum moment of the QBE. In order to account for the thermal current more accurately, the second momentum moment would have to be included as well. Although we only compare the two-fluid model and the QBE results for the experimentally relevant value of $\tau_{\text{e-phonon}}$, we show in Ref. [76] that the agreement continues to hold well for a range of $\tau_{\text{e-phonon}}$.

2.8 Multilayer Graphene

The formalism we developed for BLG can also be applied to multilayer graphene (MLG), in particular, we focus on Bernal (AB) stacked multilayers. The electrical conductivity of multilayer graphene has been measured experimentally for a range of temperatures

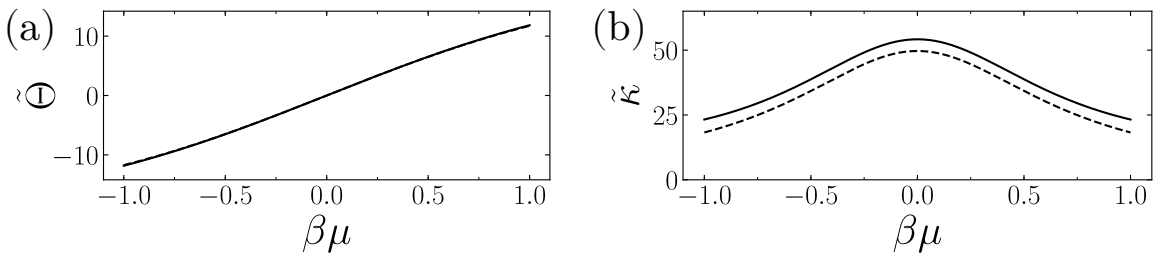

Figure 2.12: (a) The dimensionless thermoelectric coefficient is defined as $\tilde{\Theta} = (N_f e k_B T/2\hbar)^{-1}\Theta$ calculated using QBE (solid) and two-fluid approximation (dashed). The two curves show near perfect overlap. (b) The dimensionless open-circuit thermal conductivity $\tilde{\kappa} = (N_f k_B^2 T/2\hbar)^{-1}\kappa$ calculated using QBE (solid) and two-fluid approximation (dashed). Both figures use $\beta\tau_{\text{e-phonon}}^{-1} = 0.03$.

and densities [114, 115]. In Ref. [116], measurements on the minimum of the electrical conductivity for different numbers of layers are reported. Further experiments by a different experimental group have been reported [117], however, they consider the high-density regime which is the opposite limit to the one we will consider in this work.

For even[10] N, we have N quadratic bands, which we label with $r = (R, \sigma)$ where $R = 1, \ldots, N/2$ and $\sigma = \pm 1$. The energies are

$$\epsilon_{R\sigma}(p) = \sigma \frac{p^2}{2m_R}, \tag{2.83}$$

where the mass is

$$m_R = 2m \cos\left(\frac{R\pi}{N+1}\right), \tag{2.84}$$

with $m = \gamma_1/2v_F^2$. Therefore the bands appear in pairs labelled by the same R which have the same mass. For a fixed R, we have the same bandstructure as in BLG.

For BLG we had $\tau_{\text{e-e}}^{-1} \propto 1/N_f$. However, since each electron can now scatter off $N \times N_f$ species of electrons, the electron-electron scattering rate will be $\tau_{\text{e-e}}^{-1} \propto 1/(N \times N_f)$ for MLG. Recall the formula for the electron-phonon scattering rate (2.42). We note that $\rho \propto N$ and $c = \text{const.}$ as a function of N, so assuming that D only depends weakly on N, we have $\tau_{\text{e-phonon}}^{-1} \propto 1/N$. We now see that both the electron-electron and the electron-

[10] We only study even N in this section. For odd N, the low energy theory consists of $N-1$ parabolic bands and one Dirac cone. However, in the regime $\beta\mu \lesssim 1$ the density of states will be dominated by the quadratic bands. Therefore the results for odd N are expected to be similar to the results for even N, as long as one accounts for the different values of the band masses.

phonon scattering rates behave like $1/N$, although the reasons behind this scaling are very different for the two scattering mechanisms. Based on this simple scaling, it stands to reason that the hydrodynamic window in multilayer graphene is similar to that of BLG: $\tau_{\text{e-e}}^{-1}/\tau_{\text{e-phonon}}^{-1}$ is only weakly N-dependent. Since we successfully applied a hydrodynamic model to BLG, we expect this to work for MLG as well and this is confirmed in Ref.[21].

2.9 Conclusion

Hydrodynamic electron transport is a highly unusual transport regime that only occurs in extremely clean materials. Only a few materials are known that exhibit these transport properties, it is well-established that monolayer graphene is one of these materials and in this chapter we argued that bilayer graphene is another example.

In this chapter we calculated the transport properties of bilayer graphene. Our results for the electrical conductivity match the experimental results in [13]. From the experimental data we deduce that even at low temperatures, the scattering off phonons is crucial. Nonetheless, the dominant scattering mechanism is between charge carriers of the same species, which justifies a two fluid approach which shows excellent agreement with the detailed numerical results of the QBE and provides a simple way of calculating the transport properties analytically. One can adapt our two fluid model to different experimental setups with slight modifications [76].

From the two-fluid model, we immediately see two signatures of the hydrodynamic regime: (i) The violation of the Wiedemann–Franz law close to charge neutrality. (ii) The sharp increase in the electrical conductivity as the chemical potential is tuned away from charge neutrality.

We considered thermal transport as well and it would be interesting to test our predictions for the thermopower and thermal conductivity in upcoming experiments. We also extended our analysis to graphene multilayers.

The success of the two-fluid model in BLG as well as the multi-fluid model in multilayer graphene suggests that the hydrodynamic description of electrons in bilayer and multilayer graphene is accurate. This once again confirms the idea that electrons in strongly interacting systems can be considered as (multi-component) fluids [118]. The

search is ongoing for other materials that exhibit hydrodynamic electron transport. Recent candidates include WTe_2[119] and $PtSn_4$[120]. WP_2 is another candidate material, in which a violation of the Wiedemann–Franz law has been observed [121, 122]. Other candidates include the delafossites such as $PdCoO_2$ [123]. $PdCoO_2$ is notable for being three-dimensional in contrast to the other candidate materials. Transport through finite-width channels shows signatures of hydrodynamic behaviour[124]. There also attempts to detect hydrodynamic behaviour of other (quasi-)particles besides electrons in condensed matter systems, for example magnons in spintronic systems [125].

Another frontier in electron hydrodynamics is taking into account plasmons. In our work we have used the static screened Coulomb interaction. In other words, we have neglected the scattering of electrons off plasmons. In addition, the plasmons may also carry heat. In order to take into account plasmons, one must now consider a coupled set of Boltzmann equations, one for the electrons and one for the plasmons. There is evidence the plasmon contribution to heat transport is significant in monolayer graphene [111].

In future work, we plan to compute the viscosity for BLG. Adding the viscosity to the two-fluid model will give us the Navier-Stokes equations, which can then be used to simulate the electron fluid in BLG for realistic geometries. We expect those simulations to yield interesting results such as vortices in the electron flow and the corresponding negative nonlocal resistance, as for single-layer graphene. One can go even further and consider spin-transport by applying a weak magnetic field. We then have a very interesting multi-component fluid which carries charge, heat and spin.

Part II

Quantum Hall

Chapter 3

Single-particle emitters using quantum dots

3.1 Introduction

The quantum Hall effect arises when a two-dimensional electron gas (2DEG) is subjected to a strong perpendicular magnetic field. The single particle physics consists of discrete Landau levels which are highly degenerate. Once the effect of Coulomb interactions are taken into account, the electrons are known to form highly correlated states, the most simple and famous of which are the Laughlin states. In this chapter we will be interested in the ripples at the surface of this quantum Hall fluid. We will describe a method to excite these so-called edge modes to create a single-particle emitter.

Single-particle sources have many applications in physics and with the advent of quantum information and nanodevices, they are to poised to gain an even more prominent role in the future. Single-photon sources are already routinely used in quantum information processing. Knill, Laflamme and Milburn showed that linear optical quantum computing can provide a universal quantum computer [126] and single photon sources are crucial for these devices. Recently, there has been both experimental and theoretical interest in developing the analogous device for electrons, a *single-electron source* (SES) [127, 128, 129, 130, 131, 132, 133, 134]. This is essential for the growing field of nanoelectronics where one wants to control a single electron on nanodevices. As in the case of

single photons, single-electron sources are of interest to quantum computation [135, 136]. In addition, they could be useful as a current standard in metrology [137]. In this work, we also consider a source of fractional quantum Hall quasiparticles. These quasiparticles are anyons with fractional charge and statistics. Having an on-demand source of quasiparticles would be very exciting for fundamental physics research, since it would allow their properties to be better studied. In fact, recent experiments on quantum Hall edges have probed the fractional statistics of these quasiparticles [138, 139].

There are two main proposals for constructing such a source of single particles on a $1d$ conducting channel. The first proposal consists of applying a voltage pulse directly to the channel. The second proposal uses a driven quantum dot coupled to the conductor. We now discuss both methods in turn.

Refs. [140] and [141] suggested that by applying a quantized Lorentzian voltage pulse to a single channel conductor, one can generate a pure quantum excitation which includes only a single electron– a *leviton*. One place where a $1d$ conducting channel arises naturally is at the edge of a $2d$ quantum Hall droplet. In Ref. [142], Levitov et al. showed that by applying a Lorentzian voltage pulse to a quantum Hall edge (FQH and IQH), one could also achieve a pulse which includes a single quantized excitation. The scattering of these pulses and associated shot noise has been studied [143, 144, 145, 146].

An alternative proposal for the SES is to use a quantum dot—a variable energy level that can either be empty or filled—coupled to the conductor at a single quantum point contact [147, 148, 149]. Varying the energy of the dot can lead single particles to be emitted. FIG. 3.1 shows the experimental set-up where the conductor is a quantum Hall edge. By applying a time-dependent voltage, the energy of the quantum dot can be varied. We start with a dot having an energy below the chemical potential of the edge so that it is filled. Then the bias is gradually increased. We expect that as the bias crosses the chemical potential, the charge will jump off the dot onto the edge. This will result in a current pulse on the edge that can be measured downstream from the quantum point contact (QPC). It was expected that this would be a method for generating exactly quantized charge pulses, since the quantized charge on the dot will jump onto the edge and lead to a precisely quantized current pulse downstream from the QPC [149].

However, we show that for the second proposal, interactions renormalize the charge

of the pulses. Thus, we show that it is not possible to obtain precisely quantized charge pulses in this proposal. Coulomb interactions are ubiquitous in these systems, they cannot be fully screened and even if the interaction is screened with a gate, a dipole interaction will remain. Thus, the breaking of charge quantization will affect all experimental set-ups, underlining the importance of this work. If one wants to obtain a single quantized charge pulse, then our work suggests that one should use the first proposal, where the voltage pulse is applied directly to the edge.

Furthermore, we investigate more closely the mapping between our model of a single-particle source and the spin-boson model, originally suggested by [150]. This mapping is extremely useful, since the spin-boson model is very well-studied [151] and many powerful numerical techniques have been developed to solve it. We show how the results from the spin-boson model can be adapted to describe the current profile of a single-particle pulse.

3.2 Outline

The outline of this chapter is as follows. In section 3.3, we introduce quantum Hall edges. Then, section 3.4 presents our main results. We discuss in detail the model of the single-particle source that we consider and discuss how we use the mapping to the spin-boson model to obtain the current on the edge. In section 3.5 we present numerical results for the time-dependence of the current on the edge when we drive the dot. This section uses some numerical techniques developed for solving the spin-boson model. We conclude in section 3.6. Appendix C contains technical details of the calculations described in section 3.4.

3.3 Quantum Hall edges

3-dimensional metals are very successfully described by Fermi liquid theory[152]. The physics of interacting electrons in $1+1d$ is radically different to the situation in higher dimensions [153], they are described as Luttinger liquids. In this chapter, we study the chiral edge of a $2d$ fractional quantum Hall state. This 1-dimensional edge is a chiral Luttinger liquid.

Key Concept 5: The quantum Hall effect

The quantum Hall effect arises when a $2d$ electron gas is cooled to low temperatures and placed in a magnetic field B [154]. This results in a perfectly quantized electrical Hall conductance $\sigma_{xy} = \nu\frac{e^2}{h}$, where the filling fraction $\nu = N_e/N_\phi$ is the number of electrons N_e divided by the number of electrons in a filled Landau level N_ϕ. For the integer quantum Hall (IQH) effect, ν is an integer. Including the Coulomb interactions between the electrons leads to new quantum Hall states at fractional values of ν, this is the fractional quantum Hall (FQH) effect. In our work below, we focus on the case where the physics is described by the Laughlin wavefunction[a], i.e. when $1/\nu$ is an odd integer [156].

There are two distinct types of charged excitations in FQH systems. On the one hand we have electrons of charge $-e$. We also have quasiparticles of charge $-\nu e$. The quasiparticles are anyons satisfying fractional statistics. When we exchange two quasiparticles, we pick up a statistical phase $+\pi\nu$ ($-\pi\nu$) for a clockwise (counterclockwise) rotation.

[a]The Laughlin wavefunction is a proposed many-body wavefunction for fractional quantum Hall states that is the exact ground state for very short-range interactions. For Coulomb interactions this wavefunction shows a very good overlap with numerical results for small numbers of electrons[155].

3.3.1 Hydrodynamic theory of quantum Hall edges

There is a nice intuitive derivation of the Luttinger liquid Hamiltonian for the case of a quantum Hall edge. We follow the hydrodynamic approach laid out by Wen [157].

We measure the distance x along the edge. Consider a segment of length $\mathrm{d}x$. The maximum distance of the displaced fluid from the equilibrium is $h(x,t)$. Due to the confining electric field E, this displacement will be associated with an energy cost

$$U = -Ene\int \mathrm{d}x \int_0^{h(x,t)} \mathrm{d}y\; y = Ene\int \mathrm{d}x \frac{h(x,t)^2}{2}, \tag{3.1}$$

where n is the electron density, assumed uniform. The electric charge per unit length on

the edge is related via

$$\rho(x,t) = -enh(x,t) \tag{3.2}$$

and by the definition of the filling fraction ν we have

$$n = \frac{\nu eB}{2\pi\hbar}, \tag{3.3}$$

where B is the magnetic field applied perpendicularly to the disc (and we have exceptionally restored $\hbar$). Substituting (3.2) and (3.3) into (3.1) we find

$$U = \frac{\pi E}{\nu e^2 B}\int \mathrm{d}x\rho(x,t)^2 = \frac{\pi v}{\nu e^2}\int \mathrm{d}x\rho(x,t)^2, \tag{3.4}$$

where the edge velocity is $v = E/B$. This motivates the Hamiltonian

$$\hat{H}_{\mathrm{LL}} = \frac{\pi v}{\nu e^2}\int \mathrm{d}x\hat{\rho}(x,t)^2. \tag{3.5}$$

The electron operator on the edge can be written in terms of bosonic field $\hat{\varphi}(x)$ (see below). From this so-called bosonization procedure it follows that the charge density

$$\hat{\rho}(x,t) = +e\sqrt{\nu}\partial_x\hat{\varphi}/2\pi, \tag{3.6}$$

where $\hat{\varphi}(x)$ is a bosonic field satisfying bosonic commutation relations:

$$[\hat{\varphi}(x), \hat{\varphi}(x')] = i\pi\mathrm{sgn}(x-x'), \tag{3.7}$$

where $\mathrm{sgn}(x)$ is the sign function.[1] This yields

$$\hat{H}_{\mathrm{LL}} = \frac{v}{2}\int \frac{dx}{2\pi}\,(\partial_x\hat{\varphi})^2 \tag{3.8}$$

when substituted into (3.5).

[1] Technically, we should introduce a short distance cut-off a and spread the sign function continuously over a.

3.4 Quantum dot emitter

3.4.1 Quantum dots

Quantum dots are nanoscale artificial atoms [158, 159]. Like real atoms, they have discrete energy levels, however their properties are experimentally modifiable, making them very interesting for applications ranging from solar cells [160] to quantum computation [135].

In our case, we are considering a quantum dot consisting of a quantum well created using an applied voltage. By varying the applied voltage, it is possible to vary the energy of the energy levels. The quantum dot will consist of a set of approximately equidistant single electron energy levels. However, assuming the difference in energy between the levels is large enough, we can focus only on that level which is closest to the chemical potential of the edge. We denote the energy difference between this level and the chemical potential of the edge as the bias $\varepsilon(t)$. This level can be either empty or occupied, therefore we can describe the quantum dot as an effective two-state system in our model. If we create a potential well outside the quantum Hall fluid, then we can use this to store an electron. On the other hand, if we create the potential well inside the quantum Hall fluid, then this so-called anti-dot can store an FQH quasihole with fractional charge.

There is a long history of study of quantum dots coupled to Luttinger liquids [161, 162, 163, 164, 165, 166, 167, 168, 169, 170, 171, 150]. This is the set-up that we consider, however most previous work focussed on the case of a constant bias $\varepsilon(t) = \varepsilon_0$. However, in this work we are interested in the non-equilibrium driving of the quantum dot, such that we obtain a time-dependent current on the edge.

3.4.2 Model

We model the experimental set-up presented in Fig. 3.1: A quantum dot coupled to a chiral edge channel at a quantum point contact at $x = 0$. We describe this system with the time-dependent Hamiltonian

$$\hat{H}(t) = \hat{H}_{\mathrm{QD}}(t) + \hat{H}_{\mathrm{LL}} + \hat{H}_{\mathrm{tun}}(t) + \hat{H}_{\mathrm{int}}. \tag{3.9}$$

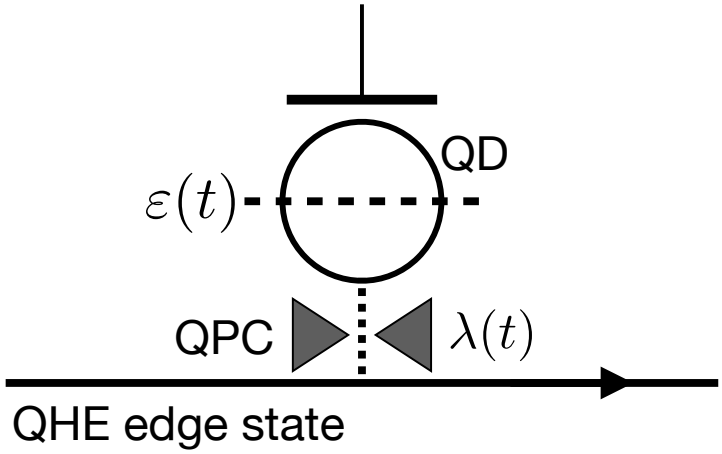

Figure 3.1: Set-up of the model. The quantum dot (QD) is connected to a quantum Hall edge (QHE) state at a quantum point contact (QPC). The QD is modelled as a single energy level which can be occupied with an electron or quasiparticle. The energy of the dot $\varepsilon(t)$, can be varied via an applied gate voltage. There is tunnelling amplitude $\lambda(t)$ between the QD and the edge, which can be controlled by the voltage applied to the QPC. Figure reproduced from [172].

The first term

$$\hat{H}_{\mathrm{QD}}(t) = \varepsilon(t)\hat{S}_z \tag{3.10}$$

describes the quantum dot with a single energy level $\varepsilon(t)$ which is controlled by a time-dependent gate voltage. The dot is a two-state system: It can be either empty or filled. Hence, it can be described by spin-1/2 operators, which have the same Hilbert space[2]. The presence or absence of a particle on the dot is measured by the operator $\hat{N} = \hat{S}_z + 1/2$. As required, $\hat{N}$ has eigenvalues 0 and 1 if $\hat{S}_z$ has eigenvalues $\pm 1/2$[3]. The operators $\hat{S}^+$ and $\hat{S}^-$ act as creation and annihilation operators respectively for the particle on the QD. When we have electrons tunnelling, $\hat{S}^+$ creates an electron with charge $-e$ on the dot with $e > 0$. When we have quasiparticles tunnelling, it creates a quasiparticle with charge $-\nu e$[4].

[2]This is not to be confused with the spin of the electrons on the edge, which we neglect due to the large Zeeman splitting in the presence of a magnetic field required to enter the quantum Hall regime.

[3]It is perhaps more intuitive to describe the quantum dot by a creation and annihilation operator $\hat{a}^\dagger/\hat{a}$, such that the occupation number of the dot is given by $\hat{N} = \hat{a}^\dagger\hat{a}$. In this case we can switch to the spin-representation via the transformation: $S_z = \hat{a}^\dagger\hat{a} - \frac{1}{2}, \quad S^+ = \hat{a}^\dagger, \quad S^- = \hat{a}$.

[4]The spin-operators commute with $\hat{\psi}(x)$ instead of satisfying fermionic or anyonic statistics, as the electron or quasiparticle operators should. As long as we are interested in the current, this will not affect the calculations. This can be seen explicitly in the perturbation theory calculation as we discuss in more detail in [173].

The second term in Eq. (3.9) is the Luttinger liquid Hamiltonian

$$\hat{H}_{\mathrm{LL}} = \frac{v}{2}\int \frac{dx}{2\pi}\,(\partial_x\hat{\varphi})^2 \tag{3.11}$$

which describes a chiral quantum Hall edge of length L and with edge velocity v. The edge is a Laughlin state at filling fraction $\nu = 1/M$, where M is an odd integer [157]. Assuming periodic boundary conditions, the bosonic field $\hat{\varphi}$ has an eigenmode expansion with momenta $k = 2\pi m/L$ where $m \in \mathbb{Z}$[7],

$$\hat{\varphi}(x) = -\sum_{k>0}\sqrt{\frac{2\pi}{kL}}(\hat{b}_k e^{ikx} + \hat{b}_k^\dagger e^{-ikx})e^{-ka/2}, \tag{3.12}$$

where a is the short-distance cutoff, and bosonic operators $\hat{b}_k$ obey commutation relations $[\hat{b}_k, \hat{b}_{k'}^\dagger] = \delta_{kk'}$.

The third term in the Hamiltonian (3.9) incorporates the tunnelling from the dot to the edge with tunnelling amplitude $\lambda(t)$:

$$\hat{H}_{\mathrm{tun}}(t) = \lambda(t)\left(\hat{\psi}^\dagger(0)\hat{S}^- + \hat{\psi}(0)\hat{S}^+\right). \tag{3.13}$$

The first term creates a particle (electron or quasiparticle, depending on γ) on the edge and annihilates the particle on the dot. The second term creates a particle on the dot and annihilates a particle on the edge. For an FQH edge with filling fraction ν, the electron and quasiparticle operators in the bosonized form [157, 7, 174] are described by the vertex operators[5]

$$\hat{\psi}(x) = \frac{1}{\sqrt{2\pi a\gamma}}e^{-i\gamma\hat{\varphi}(x)}, \tag{3.14}$$

where $\gamma = 1/\sqrt{\nu}$ for electrons, and $\gamma = \sqrt{\nu}$ for quasiparticles. When $\hat{\psi}(x)$ is the electron annihilation operator, it satisfies the fermion anticommutation relations

$$\{\hat{\psi}(x), \hat{\psi}(x')\} = 0 \tag{3.15}$$

[5]Technically, we should include Klein factors in the bosonization identity. However, since in our model below we only have one species of chiral fermion and are interested in calculating the current, the Klein factors will drop out of the calculation and hence for simplicity, we do not introduce them in the first place.

whereas when $\hat{\psi}(x)$ is the quasiparticle annihilation operator, it satisfies the anyon commutation relations

$$\hat{\psi}(x)\hat{\psi}(x') = e^{i\pi\nu \mathrm{sgn}(x-x')}\hat{\psi}(x')\hat{\psi}(x). \tag{3.16}$$

The last term in Eq. (3.9) incorporates the Coulomb interactions between the dot and the edge,

$$\hat{H}_{\mathrm{int}} = -\gamma \frac{g}{2\pi}\partial_x \hat{\varphi}(0)\hat{S}_z, \tag{3.17}$$

where $g > 0$ is the interaction strength. To justify this expression, recall that from the bosonization scheme, we can show that the charge density operator on the edge is [6]

$$\hat{\rho}(x) = +e\sqrt{\nu}\partial_x\hat{\varphi}/2\pi. \tag{3.18}$$

If we have a quasiparticle, then $\gamma = \sqrt{\nu}$ and the charge of the particle is $-\nu e$. If we have an electron, then $\gamma = 1/\sqrt{\nu}$ and the charge of the electron is $-e$. We can summarize this by saying that the charge of the particle on the dot is $q = -\gamma\sqrt{\nu}e$. Since the number operator on the dot is $\hat{N} = \hat{S}_z + 1/2$, the operator giving the charge on the dot is $\hat{Q} = -\gamma\sqrt{\nu}e\hat{N}$. The Hamiltonian will hence be

$$\hat{H}_{\mathrm{int}} \propto \hat{\rho}(0)\hat{Q} = -\gamma\nu e^2 \frac{1}{2\pi}\partial_x\hat{\varphi}(0)\hat{N} \tag{3.19}$$

where the proportionality constant will depend on the geometry (distance of dot from edge) and the dielectric constant of the material. We assumed that the Coulomb interactions only affect one point $x = 0$ on the edge.

3.4.3 Mapping to the spin-boson problem

The Hamiltonian of our model Eq. (3.9) can be mapped to the spin-boson model using the unitary transformation suggested by Furusaki and Matveev [150]. Following these authors we define an operator $\hat{U}_1 = \exp\left[-i\gamma\hat{\varphi}(0)\hat{S}_z\right]$. Under a unitary transformation

[6] This can be shown by using the expression (3.14) in $\hat{\rho}(x) = -e : \hat{\psi}^\dagger(x)\hat{\psi}(x) :$ and using point-splitting. Here, $: \cdots :$ stands for normal ordering and $\hat{\psi}^\dagger(x)$ is the electron operator.

$\hat{H}_1 = \hat{U_1}^\dagger \hat{H} \hat{U}_1$ the Hamiltonian becomes

$$\hat{H}_1 = \varepsilon(t)\hat{S}_z + \frac{v}{2}\int \frac{dx}{2\pi}(\partial_x\hat{\varphi})^2 + \lambda(t)\sqrt{\frac{2}{\pi a\gamma^2}}\hat{S}_x + v\tilde{\gamma}\hat{S}_z\partial_x\hat{\varphi}(0). \tag{3.20}$$

In this representation the effect of the Coulomb interactions amounts to a rescaling of γ such that

$$\tilde{\gamma} = \gamma\left(1 - \frac{g}{2\pi v}\right). \tag{3.21}$$

To bring it into the more familiar spin-boson form, we introduce

$$\Delta(t) = \lambda(t)\sqrt{\frac{2}{\pi a\gamma^2}}, \quad \eta_k = v\tilde{\gamma}\sqrt{\frac{2\pi k}{L}}e^{-ka/2} \tag{3.22}$$

to obtain

$$\hat{H}_1 = \varepsilon(t)\hat{S}_z + \Delta(t)\hat{S}_x + \sum_{k>0}\omega_k\hat{b}_k^\dagger\hat{b}_k - i\hat{S}_z\sum_{k>0}\eta_k(\hat{b}_k - \hat{b}_k^\dagger), \tag{3.23}$$

where $\omega_k = vk$. This is the spin-boson Hamiltonian [151]. We emphasize that the transformation between Hamiltonians of Eq. (3.9) and Eq. (3.23) is exact. We present a detailed version of this calculation in Appendix C.

3.4.4 The spin-boson model

The spin-boson model derived in the previous section consists of a spin in a magnetic field coupled to a bosonic heat bath. Since a spin-1/2 is a two-level system, we can also view the spin-boson model as describing a two-level system, where $\varepsilon(t)$ is the energy difference between the levels and $\Delta(t)$ quantifies the tunnelling amplitude between them. The spin-boson model is the archetype of a quantum dissipative system. It is useful as a model for what happens when we couple a quantum system to an environment—a so-called open quantum system. For example, it can be used as a model for the decoherence of qubits in quantum information[175, 176]. The first two terms in the Hamiltonian (3.23) describe the Zeeman coupling of the spin $\hat{\mathbf{S}} = (\hat{S}_x, \hat{S}_y, \hat{S}_z)$ to the time-dependent magnetic field $\mathbf{B}(t) = \varepsilon(t)\hat{\mathbf{z}} + \Delta(t)\hat{\mathbf{x}}$. The second term describes the bosonic heat bath as a set of harmonic oscillators with frequency $\omega_k = vk$. The bosonic ladder operators $\hat{b}_k$ obey commutation relations $[\hat{b}_k, \hat{b}_{k'}^\dagger] = \delta_{kk'}$. The last term couples the heat bath to the spin

with coupling constants η_k. By creating or annihilating a boson in the heat bath, it is possible to flip the spin (in the x basis). The spectral function of the spin-boson model is defined as

$$J(\omega) = \pi \sum_{k>0} \eta_k^2 \delta(\omega - \omega_k) = 2\pi\alpha\omega\Theta(\omega)e^{-\omega a/v}, \tag{3.24}$$

using the form of η_k from eq. (3.22) (the so-called Ohmic heat bath). Here $\Theta(\omega)$ is the Heaviside theta-function and a is again a UV-cutoff. We have defined the dimensionless coupling $\alpha = \tilde{\gamma}^2/2$.

The mapping to the spin-boson model is useful, due to the wealth of numerical techniques developed to study it. We discuss these in Section 3.5.

3.4.5 Current

We now discuss the main topic of this chapter—the current on the edge when the QD is driven. As we increase the bias of the QD $\varepsilon(t)$ from far below to far above the chemical potential of the edge, the dot will go from initially being fully occupied, $\langle \hat{N} \rangle = 1$, to being empty, $\langle \hat{N} \rangle = 0$. Thus, the particle will jump off the dot onto the edge. This will lead to a current pulse on the edge, which can be measured using a detector downstream from the QPC. We are interested in the relation between the rate of change of the occupation number on the dot, $d\hat{N}/dt$ and the current on the edge $\hat{I}$. For the chiral FQH edge, the current operator is given by

$$\hat{I}(x,t) = v\hat{\rho}(x,t) \tag{3.25}$$

in terms of the charge density operator $\hat{\rho}$, since all excitations move at speed v.

In this section, we will present an exact relation between the current on the edge and the rate of change of the QD occupation number. In order to calculate the current, we work in the Heisenberg picture, where the operators are time-dependent and calculate the equations of motion for the operators $\hat{N}(t)$ and $\hat{\varphi}(x,t)$. In Appendix C, we show that we can use the equations of motion generated from $\hat{H}$ to derive the relation between $\partial_x\hat{\varphi}$

just left and just right of the QPC

$$\frac{v}{2\pi}(\partial_x\hat{\varphi}(+0,t) - \partial_x\hat{\varphi}(-0,t)) = \tilde{\gamma}\frac{d\hat{N}(t)}{dt}. \tag{3.26}$$

Equations (3.18) and (3.25) allow us to relate the left-hand side of (3.26) to the current on the edge. We now assume the boundary condition that there is no incoming current left of the QPC, hence $\partial_x\hat{\varphi}(-0,t) = 0$. The equations of motion for $\hat{\varphi}(x,t)$ away from $x = 0$ are just those of a free chiral wave propagating to the right at speed v. Therefore, we can relate the current measured by the detector at a point $x > 0$ further downstream from the QPC to the current just right of the QPC. This introduces the argument $t - x/v$:

$$\hat{I}(x,t) = -\tilde{q}\frac{d\hat{N}(t - x/v)}{dt}, \tag{3.27}$$

where

$$\tilde{q} = q\left(1 - \frac{g}{2\pi v}\right). \tag{3.28}$$

The details of this calculation are found in Appendix C.

If we integrate both sides of (3.27) over time, then the LHS gives us the total charge in the pulse measured by a detector downstream. The RHS gives us the change in $\hat{N}$. Naively, one would therefore expect from charge conservation that the proportionality constant between $\hat{I}$ and $d\hat{N}/dt$ should be equal to the charge of the particle on $\hat{N}$, i.e. q. Indeed this is case in the absence of Coulomb interactions between the dot and the edge. In the interacting case the charge of the pulse gets renormalized by a factor $\tilde{\gamma}/\gamma < 1$ i.e. the charge in the pulse is not the same as the charge on the dot.

We present the following physical explanation of this surprising result. The repulsive Coulomb interactions due to the charge on the dot depletes the charge on the edge close to the QPC. If we charge the dot with a particle of charge q from the edge, then the charge on the edge at the QPC is depleted by $q - \tilde{q}$ due to the repulsive Coulomb interactions. This will lead to a net charge pulse $-\tilde{q}$ travelling down the edge. Following emission of the particle of charge q by the dot, charge $q - \tilde{q}$ fills up the depleted area on the edge, which reduces the net charge flowing downstream from the dot to $\tilde{q}$. Therefore, when a particle tunnels from the dot into the edge, the charge leaving the dot is quantized, but

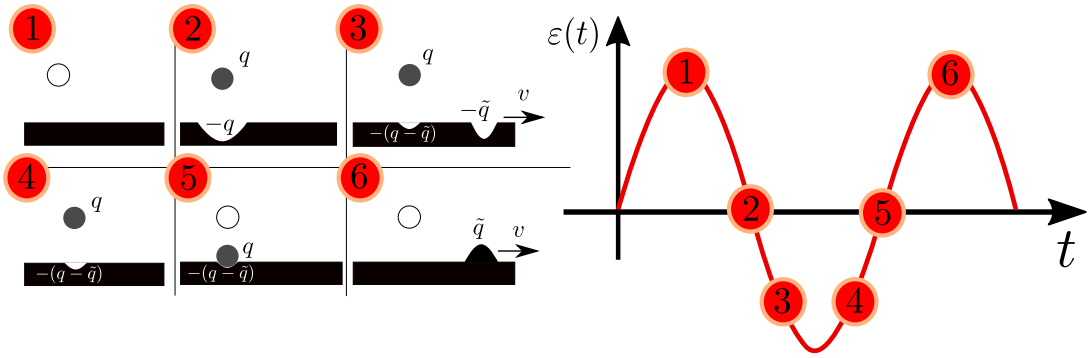

Figure 3.2: Sketch of one cycle of a drive of the single-particle emitter. (1) The bias $\varepsilon(t)$ of the quantum dot is far above the chemical potential of the edge and hence the dot is empty. (2) As the bias crosses the chemical potential, the dot fills up with charge q from the edge. By charge conservation the edge must be depleted by charge q. (3) There will be a pulse of charge $-\tilde{q}$ downstream travelling at speed v. (4) A depletion of amount $q - \tilde{q}$ will stay at the QPC, this is the depletion due to Coulomb repulsion. (5) As the dot crosses above the chemical potential again, charge q will jump off the dot. (6) The energy of the dot is high above the chemical potential so the dot is empty and there is not charge depletion at the QPC any more. Charge q from the dot and the depletion $q - \tilde{q}$ have cancelled to give a pulse of charge $\tilde{q}$ downstream.

the net charge in the resulting current pulse downstream is always less than the particle charge. As shown in Fig. 3.2 during a whole cycle of the bias e.g. $\varepsilon(t) = \varepsilon_0 \sin \Omega t$—as long as the amplitude of oscillation ε_0 is large enough and the frequency Ω of oscillations is small— there will be two well-separated charge pulses, one with charge $-\tilde{q}$ and one with charge $\tilde{q}$.

Another intuitive way to understand this result is in terms of capacitance. The interactions effectively add a capacitance to the system, and the charge stored on this capacitor is released in addition to the charge on the dot in the emission process. Since the current from the capacitor is exactly out of phase with the current from the dot, this reduces the charge in the outgoing pulse on the edge.

3.5 Numerics

The spin-boson model can be solved exactly at the Toulouse point $\alpha = 1/2$. In the quantum dot model, this corresponds to $\nu = 1$ i.e. the IQH case. Indeed, in the IQH case we can directly solve the quantum dot model for arbitrary bias [173]. Away from this solvable point, numerical techniques must be used. The mapping to the spin-boson

Hamiltonian is particularly useful, since it enables one to use powerful numerical techniques developed for this well-studied problem. These include the non-interacting blip approximation (NIBA) [151], the generalized master equation (GME) approach [177], the stochastic Schrödinger equation (SSE) approach [178], the Bethe-Ansatz [179], the numerical renormalization group approach [180, 181] and, most recently, tensor network methods [182, 183]. Most approaches have limitations in that they require either small coupling λ or small spin-bath coupling α and the computation time scales poorly with the total time scale. We will adopt the generalized master equation approach, which is both simple in its implementation and which makes possible calculations for arbitrary times provided α is small. This allows the calculation of the current resulting from non-equilibrium driving of the quantum dot.

The master equation is an integro-differential equation for the time-evolution of the expectation value of the spin $\langle \hat{S}_z \rangle$. It is derived from the path-integral solution for the time-evolution of the reduced density matrix in terms of the Feynman-Vernon influence functional, see [184]. The heat-bath degrees of freedom are traced out exactly, leaving the evolution of the spin. The GME is [184, 177]

$$\frac{d}{dt}\langle \hat{S}_z(t) \rangle = \int_0^t d\tau \, [\frac{1}{2} K^a(t,\tau) - K^s(t,\tau)\langle \hat{S}_z(\tau) \rangle]. \tag{3.29}$$

Here the integral kernels $K^{(a,s)}(t,\tau)$ can be obtained in terms of a series expansion in $\Delta(t)$ for arbitrary α. However, each factor of $\Delta(t)$ in this expansion comes with an integration over time, hence we have to truncate the series in our numerical calculations in the case when α is not small. Remarkably, to linear order in α it is possible to sum up the entire series expansion in $\Delta(t)$ analytically [177] and obtain expressions for $K^{a,s}(t,\tau)$ which are exact in $\Delta(t)$. This formulation of the master equation is useful for $\alpha = \tilde{\gamma}^2/2 \ll 1$. Experiments have already been performed for a driven quantum dot single particle source in the IQH case [148]. The results agree with the exact results that can be obtained in the IQH case [149]. Future experiments may be able to access the FQH regime, in order to obtain a single quasiparticle source. We are particularly interested in the fractional case with filling fraction $\nu = 1/3$ since it is the most robust FQHE state. We will focus on the case where quasiparticles are tunnelling, since this gives a smaller value of α. For

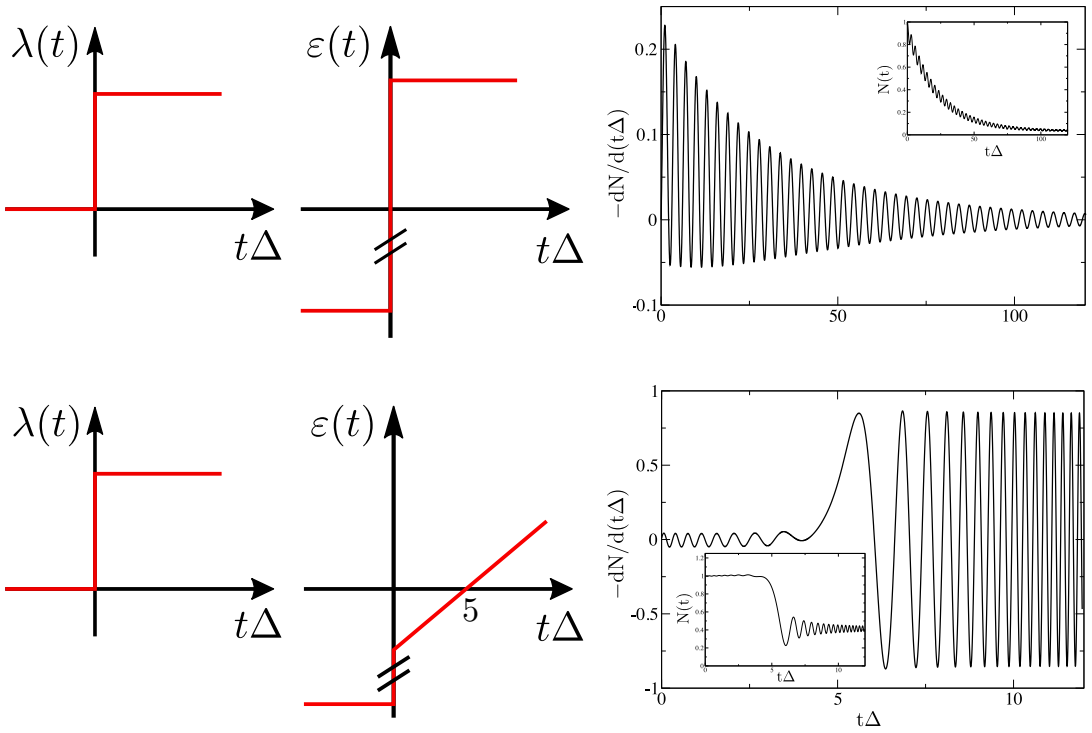

Figure 3.3: Numerical results for the current on the edge $I(t, x = +0) \propto -dN/d(t\Delta)$ (main figures) and the time-evolution of the occupation of the QD $N(t)$ (insets). We present two different sweep protocols. In both cases, the coupling is switched on suddenly at $t = 0$ so $\lambda(t) = \lambda\Theta(t)$. The initial condition on the dot occupation is $N(0) = 1$ which corresponds to a large negative bias at $t < 0$. (Top) At $t = 0$ the bias undergoes a step to $\varepsilon(t) = \varepsilon_0$ at $t > 0$. The parameters are $a = 0.005v\Delta^{-1}$, $\alpha = 0.05$, $\varepsilon_0 = 2\Delta$. We use an analytical expression valid in this situation. (Bottom) Starting at $t = 0$ the bias increases linearly as $\varepsilon(t) = \xi(t - t_0)$. The bias passes through $\varepsilon = 0$ at $t_0 = 5\Delta^{-1}$. The other parameters are $a = 0.005v\Delta^{-1}$, $\alpha = 0.05$, $\xi = 2\Delta^2$. We numerically solve the GME for this plot. Figure reproduced from [172].

the case without Coulomb interactions, $\alpha = 1/6$ when $\nu = 1/3$. This is not small enough to justify the use of the GME, which typically requires $\alpha < 0.05$. However, the reduced value of effective interaction strength $\tilde{\gamma}$ compared to γ (see eq. (3.21)) suggests that it may be possible to have small values $\alpha \ll 1$ even for the $\nu = 1/3$ state.

We consider two different experimentally relevant sweep protocols of the bias $\varepsilon(t)$ in this section. In both cases, the initial condition has the dot occupied $N(0) = 1$ and the edge in equilibrium. This means the the bias $\varepsilon(t < 0)$ is large and negative. We suddenly switch on the coupling $\lambda(t)$ between the dot and the edge at $t = 0$ i.e. $\lambda(t) = \lambda\Theta(t)$. We plot the rate of change of the occupation of the dot, $-\,\mathrm{d}N/\,\mathrm{d}(t\Delta)$, which is proportional to the current $I(t, x = +0)$ just downstream from the QPC according to (3.27).

In the top panel of Fig. 3.3 we present the results when a constant bias is applied to the dot, $\varepsilon(t) = \varepsilon_0 > 0$ for $t > 0$. Since the bias is negative for $t < 0$, this models the step in the first half-period of a square-wave bias. This case with a constant bias does not require the full GME, in fact there is an analytical expression obtained in [178, 185] for the time-evolution of the spin. This approximation is valid at $\alpha \ll 1$.This approach allows us to study much later times $t\Delta \gg 1$ than with the GME. The inset shows the occupation of the QD $N(t)$. At late times, N tends to zero, which corresponds to a downstream current pulse of charge $\tilde{q}$ according (3.27). We find that the current oscillates function of time after the voltage step. These coherent oscillations are typical of the small α regime. There is a change in behaviour in the spin-boson model as α passes through $1/2$. For $\alpha < 1/2$ we get coherent oscillations as above. When $\alpha > 1/2$, the dynamics become incoherent, i.e. $N(t)$ will decay monotonically [151]. $\alpha = 1/2$ corresponds to the IQH case, however the effect of the Coulomb interactions is to decrease α. Therefore, the Coulomb interactions in the IQH case could push the system from the incoherent dynamics to the coherent dynamics regime.

The bottom panel of Fig. 3.3 shows our numerical results obtained from the GME for the current on the edge when the energy of the QD increases linearly with rate ξ. so that $\varepsilon(t) = \xi(t - t_0)$. This is the so-called Landau-Zener sweep. It can model the situation where the bias $\varepsilon(t)$ passes through the chemical potential during a sine-wave drive. In this case, in contrast to a step-pulse, not all the charge leaves the quantum dot during the ramp, instead the occupation number of the QD at late times tends to $\exp(-\pi\Delta^2/2\xi)$. This is the Landau-Zener result [178, 186, 187]. It is surprising since $\varepsilon(t)$ becomes very large at late times, so we would expect the occupation to drop to zero. This behaviour is distinctly non-adiabatic since the equilibrium occupation of the QD at large bias must vanish. The current produced by the linear ramp oscillates as a function of time with an instantaneous frequency set by $\varepsilon(t)$ [7].

In our idealized model, the charge on the dot tends to a nonzero constant at late times, however in realistic settings, there will be additional effects such as phonons. These will cause the charge to leak off the dot eventually. As long as these timescales are long

[7]Oscillations in the current, when the energy of the dot is well below the chemical potential of the edge (i.e. before the onset of the voltage ramp), is an artefact of an abrupt switching-on of the tunnelling $\lambda(t)$ at $t = 0$.

enough, the Landau-Zener result is another impediment to precisely quantized pulses.

3.6 Conclusion

We studied a model of a single-particle emitter consisting of a driven quantum dot coupled to a quantum Hall edge. When the energy of the dot passes through the chemical potential, charge jumps off the dot onto the edge, producing a charge pulse. We showed that there are two effects that destroy the precise quantization of these pulses: (1) The Coulomb interactions between the dot and the edge. (2) Landau-Zener physics. Coulomb interactions are unavoidable in the QD set-up, and hence we argue that this set-up is not the most promising route for creating precisely quantized charge pulses.

In the alternative proposal for a single-particle emitter, where a voltage pulse is applied directly to the edge at the QPC, there are no Coulomb interactions and therefore the quantization of the charge pulses is robust. This approach is therefore more promising for creating a single-particle source. The drawback in this proposal is that the applied voltage pulses must be fine tuned Lorentzians. Another alternative is the pump geometry proposed by [188]. In this case, there are two QH channels connected via a quantum dot. We can tunnel one particle from the first channel onto the dot and then on from the dot onto the second channel. It is clear, that in this case a full charge must be transferred from one edge onto the other. However, even in this case the Coulomb interactions have an effect. Instead of one pulse on the edge when the charge is transferred, there will be two pulses. When we fill the dot from the first edge, the Coulomb repulsion between the dot and the second edge means there will be a pulse on the second edge and the charge on the second edge will be depleted. When the charge from the dot is released onto the second edge, there will be a second pulse, however its charge will be reduced due to the charge depletion.

An experiment in the IQH case approximated by the model we described was performed in [148]. However, a more accurate experiment would be required in order to determine whether the charge quantization of the pulses is indeed modified by the Coulomb interactions as we have discussed. It would be very interesting to perform this experiment to higher accuracy or modify it to include a FQH edge.

We showed how the mapping to the spin-boson problem and the generalised master equation solution can be used to efficiently simulate this system. For the future, the approach to solving the spin-boson problem using tensor network techniques is very promising. The work [183] which focussed on the zero bias case $\varepsilon(t) = 0$ can be extended to arbitrary time-dependent bias $\varepsilon(t)$ [189]. It is valid for arbitrary α and arbitrary λ. Therefore, using the mapping of the single-particle source to the spin-boson model, this approach will enable the calculation of any current pulse in any regime. This will enable a clear comparison between experiments and the theory.

Chapter 4

Trial wavefunctions for quantum Hall bilayers

4.1 Introduction

In this chapter we study the longstanding problem of a bilayer quantum Hall (BQH) system at total filling fraction $\nu = 1$[190]. The $\nu = 1$ BQH system consists of two two-dimensional electron gases in a magnetic field B applied perpendicular to the layers (Fig. 4.1). The two layers are separated by a distance d. The typical separation between electrons within a layer is given by the magnetic length $\ell_B = \sqrt{\hbar/eB}$. The system is thus governed by a single dimensionless parameter: d/ℓ_B. The typical scale of the Coulomb interaction within a layer will be $e^2/(\epsilon\ell_B)$, whereas the maximum interaction between the layers will be $e^2/(\epsilon d)$. Therefore, d/ℓ_B can be thought of as tuning the ratio of intralayer ($V_{\uparrow\uparrow}$) to interlayer ($V_{\uparrow\downarrow}$) Coulomb interactions. For large d/ℓ_B, this ratio will be $V_{\uparrow\uparrow}/V_{\uparrow\downarrow} \sim d/\ell_B$, whereas for small d/ℓ_B, this ratio will be $V_{\uparrow\uparrow}/V_{\uparrow\downarrow} \sim 1$.

If the distance d between the two layers is large compared to the magnetic length ℓ_B, the two layers behave essentially as independent quantum Hall systems with intralayer interactions only. As d/ℓ_B is decreased, interlayer correlations develop. The BQH set-up thus offers a platform to study systems of strongly-interacting electrons with competing interactions. The nature of the transition between the small and large d states and the state around $d/\ell_B \sim 1$ are poorly understood.

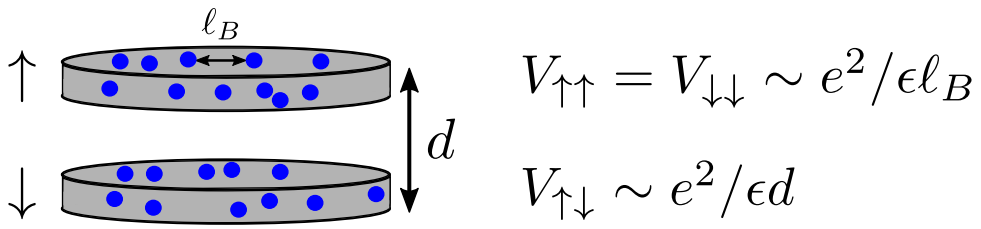

Figure 4.1: The BQH system consists of two layers of quantum Hall fluid separated by distance d. We label the layers by a pseudospin index $(\uparrow, \downarrow)$. The typical distance between electrons within a layer is ℓ_B. Thus the typical scale of the Coulomb interaction within a layer will be $e^2/(\epsilon\ell_B)$, whereas the maximum interaction between the layers will be $e^2/(\epsilon d)$.

The behaviour at small interlayer separations is well understood. At $d/\ell_B = 0$ Halperin's 111 state [27] is the exact ground state. The 111 state can be viewed as a condensate of interlayer excitons, i.e. s-wave pairing of electrons in one layer with holes in the other layer. Since electrons repel each other, at small d it makes sense for an electron in one layer to pair with a hole in the opposite layer in order to minimize the energy. Alternatively, the 111 state can be viewed as a pseudospin ferromagnet where the pseudospin index is the layer index [191, 192]. Numerous experiments on quantum Hall bilayers [193, 194, 195, 196, 197, 198, 199, 200, 201, 202, 203, 204, 205, 206, 207] support the exciton picture, see also review [190] and references therein. As d/ℓ_B is decreased, a zero-bias peak in the tunnelling conductance is seen starting around $d/\ell_B \sim 1.6$ [197] and this is taken to be the signature of a phase transition to an interlayer coherent phase: If an electron in the top layer is bound to a correlation hole in the bottom layer, it is easy for the electron to tunnel from the top layer to the bottom layer, since the charge distribution in the bottom layer is favourable for such a tunnelling process to occur. A further signature of the exciton condensate is seen in the counterflow geometry, where two opposite currents flow in opposite layers without resistance, which can be interpreted as the superflow of excitons [199, 201, 207].

In the case where the two layers are balanced, i.e. $\nu_\uparrow = \nu_\downarrow = 1/2$, the large d/ℓ_B behaviour is also well known. The two layers behave essentially as independent $\nu = 1/2$ quantum Hall systems. For a single independent $\nu = 1/2$ layer, we can perform the flux attachment procedure [208, 209, 210, 211, 212, 213] to attach two flux quanta to each electron, forming composite fermions. These composite fermions (CFs) now feel no

average magnetic field and can therefore form a composite Fermi liquid (CFL), which has been seen in experiments[214, 215]. This has also been termed a hidden Fermi liquid [216], since it is only after the flux attachment procedure, that the Fermi liquid nature of the state becomes apparent. The CFL is described by the Halperin-Lee-Read (HLR) [217] theory, however Son recently put forward an alternative proposal, where the composite fermions are Dirac fermions [218, 219].

The challenge is then to find a unified description for both the small and large d/ℓ_B behaviour, since the description in the two regimes is in terms of different quasiparticles: electron-hole excitons at small distances and composite fermions at large distances. In this chapter we propose a unified description that works well for any interlayer separation.

Early theoretical work based mainly on Hartree-Fock (HF) calculations [192, 220, 221, 222, 223, 224, 225] suggested that at small d/ℓ_B the BQH system behaves like an easy-plane ferromagnet. At small d/ℓ_B there is a Goldstone mode, which can be viewed as pseudospin waves. The HF calculations see a roton-like minimum in this dispersion develop and go gapless at a finite momentum at some critical interlayer separation[220, 221, 222, 223, 224]. This is viewed as a signal of an instability towards a state with pseudospin density waves, however this is a spurious result of the HF treatment. No evidence of translational symmetry breaking has been seen in experiments, where we would expect to see an anisotropy in the transport properties if there is a modulation at a single wavevector. Furthermore, in exact diagonalization the ground state is always a translationally invariant state (on the sphere we always have a rotationally invariant ground state).

Key Concept 6: Exact diagonalization (ED)

For a finite system, we can always write down the exact Hamiltonian matrix for the system and diagonalize it. This method is known as exact diagonalization. For large matrices, this diagonalization is best done using the iterative Lanczos algorithm. The Hilbert space dimension will be exponential in the number N of electrons and therefore this approach will be limited to small system sizes. For quantum Hall systems one typically looks at electrons on a sphere or on a torus. State-of-the-art numerics are limited to around $N \lesssim 20$ electrons.

Since then, there have been many numerical approaches to investigate the transition between the small and large distance physics in the BQH system including detailed ED up to 20 electrons [226, 35, 227, 38, 39, 31, 228, 229, 230, 231, 34] and a DMRG study on 24 electrons[232]. Despite all these years of work, the nature of the transition between the state at small d and large d has remained elusive. Many physical proposals have been put forward: A picture entirely in terms of composite bosons (CBs) [28, 29, 30], mixed CB-CF wavefunctions [31], a finite momentum BEC of excitons [32], a paired exciton condensate [33], a BEC of CB excitons [34] and deconfined merons [35].

Two proposals for the intermediate phase are particularly relevant for the present work. Firstly, in the interlayer coherent composite Fermi liquid (ICCFL) [36, 37] picture, the composite fermions form bonding and anti-bonding orbitals. A mean field theory calculation [36] including the short-range interlayer interactions shows a first order transition from a state of decoupled CFLs to a state where all the CFs are in the bonding orbitals. However, the ICCFL is not thought to be relevant in the description of double quantum wells since the ICCFL would have a large longitudinal drag resistance which is not seen experimentally. Secondly, one may view the intermediate state as a BCS pairing instability of the composite Fermi seas in the two layers. In work based on HLR theory[233, 234] the instability is proposed to be p-wave pairing of the composite fermions and indeed in an ED study [39] the p-wave channel was found to be the symmetry channel with the largest gap. In ED studies[38, 39] the p-wave paired state has very high overlaps with the exact ground states down to distances $d \sim \ell_B$, however these previous studies found that the overlap decreases at $d \lesssim \ell_B$ which would seem to indicate that this trial state does not capture the 111 phase. However Ref. [235] argues that the p-wave paired state and the 111 state can in fact be continuously connected. Therefore the BQH system is in the same phase of matter in both the $d \to 0$ and $d \to \infty$ limit, i.e. there need not be a phase transition as a function of interlayer distance. In this chapter we re-examine this p-wave trial state by including more variational parameters and by using an optimization algorithm designed to converge to global and not only local minima. We find that this p-wave trial state in fact does have high overlaps with the 111 state, consistent with Ref. [235].

Key Concept 7: Trial wavefunctions

A complementary approach to ED is that of trial wavefunctions. Motivated by ED or perhaps field theory, one can write down a wavefunction for the system which one hopes is in the same universality class as the true ground state. The trial wavefunction may be a single wavefunction or a class of variational wavefunctions. One way to verify that the trial state is close to the ground state is by computing the overlap with the true ground state found in ED. The ED ground state will only be known for small system sizes and then we can extrapolate the trial wavefunction thus found to larger system sizes. The advantage of these trial states is that they can be used for larger system sizes where ED is no longer feasible. In addition, a trial wavefunction can yield better physical understanding of the problem at hand.

We suggest a new description of the physical system, namely s-wave pairing of the composite fermions in one layer with composite holes (anti-CFs, or: ACFs) in the other layer. This proposal is appealing, because it describes the correct types of quasiparticles in both the small d/ℓ_B limit (excitons) and large d/ℓ_B limit (CFs). The evolution of the system as a function of d/ℓ_B is analogous to the BEC-BCS crossover familiar from cold atom gases[236] as shown in Fig. 4.2. At large d, we have weakly bound CF/ACF pairs (BCS limit), whereas at small d, we have tightly bound CF/ACF pairs (BEC-like limit[1]). We show that the trial wavefunction we propose has high overlaps with the ED ground state. A further advantage of this trial state is that it very naturally deals with charge imbalance of the layers.

4.2 Outline

In Sec. 4.3 we discuss the bilayer quantum Hall set-up. We then introduce the problem in the spherical geometry in Sec. 4.4: We present the single-particle wavefunctions and write down the states relevant in the small d (111 state) and large d (CFL) limits. We also write down the Hamiltonian. In Sec. 4.5 we introduce two different trial states. We

[1]We refer to this as a BEC-like limit instead of a true BEC limit, since the BEC limit is strictly speaking the limit $\Delta \gg E_F$, where Δ is the superconducting order parameter and E_F is the Fermi energy. In Sec. 4.7 however, we show that $\Delta \sim E_F$ at $d = 0$. One way to reach the true BEC limit may be to highly imbalance the layers[237].

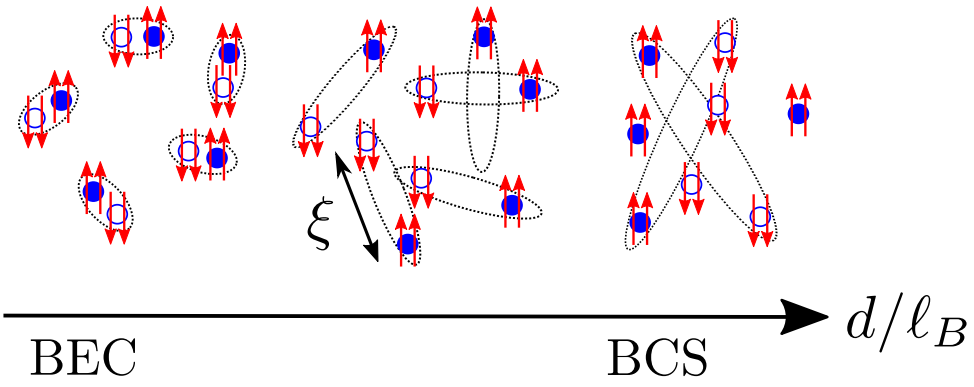

Figure 4.2: The bilayer quantum Hall system in the BEC-BCS crossover framework: At large d/ℓ_B, we have weakly bound CF(↑)/ACF(↓↓) pairs. The size of the Cooper pairs, ξ is much larger than the typical interparticle spacing ℓ_B. This is the BCS limit. At small d/ℓ_B, we have tightly bound CF/ACF pairs (BEC-like limit).

first recap the p-wave paired BCS state from Refs. [238, 239]. We then introduce the new s-wave paired state which we investigate in this chapter. We then present our numerical results. First we describe the case of the balanced bilayers (Sec. 4.6) and we compute the BCS parameters from the trial wavefunction to substantiate the BEC-BCS crossover picture (Sec. 4.7). Next we discuss the imbalanced case (Sec. 4.8). We close with a discussion of the relevance to experiments in Sec. 4.9. In App. D we provide details on the Monte-Carlo procedure and the ground state Hilbert space dimension.

4.3 Problem set-up

We consider two semiconductor layers parallel to the xy-plane with electron densities $n_\uparrow$ and $n_\downarrow$ separated by distance d with an insulating material with dielectric constant ϵ, such that there is negligible tunnelling between the layers (Fig. 4.1). We apply a field $\mathbf{B} = B\hat{z}$ perpendicular to the layers. The magnetic length is $\ell_B = 1/\sqrt{eB}$. The filling fractions in the layers are $\nu_{\uparrow,\downarrow} = 2\pi n_{\uparrow,\downarrow}\ell_B^2$ and we set the field such that the total filling factor $\nu_T = \nu_\uparrow + \nu_\downarrow = 1$ is fixed. We are interested in changes in the system as d/ℓ_B varies. In experiments, d is fixed for a given sample. Therefore changing d/ℓ_B is achieved by changing ℓ_B rather than changing d. This can be done by varying B and $n_T = n_\uparrow + n_\downarrow$ such that ν_T stays fixed.

If the distance between two electrons projected onto the xy-plane is r, then the

Coulomb interaction potential is $V_{\uparrow\uparrow}(r) = V_{\downarrow\downarrow}(r) = e^2/(4\pi\epsilon r)$ for electrons in the same layer (intralayer interaction) and $V_{\uparrow\downarrow}(r) = e^2/(4\pi\epsilon\sqrt{r^2+d^2})$ for electrons in different layers (interlayer interaction).

To simplify the problem, we assume that the physical spin of the electrons is completely polarized due to the Zeeman splitting and exchange interaction, although we note that recent work [193] suggests that incomplete spin polarization may be important for this problem, when tunnelling into a layer is considered. Furthermore, we work in the lowest Landau level (LLL) limit.

4.4 Quantum Hall on the sphere

4.4.1 Single-particle states

The single particle eigenstates on the sphere are the monopole harmonics $Y_{q,n,m}(\Omega)$, where the total flux through the sphere is $N_\phi = 2q$ (q can be integer or half-integer), $n = 0, 1, 2, \ldots$ is the LL index ($n = 0$ for the LLL). $m = -q-n, -q-n+1, \ldots, q+n$ labels the $d_n = 2(q+n)+1$ degenerate states within a LL. From [240]

$$\begin{aligned} Y_{q,n,m}(\Omega) =& N_{qnm}(-1)^{q+n-m} e^{iq\varphi} u^{q+m} v^{q-m} \\ & \times \sum_{s=0}^{n} (-1)^s \binom{n}{s} \binom{2q+n}{q+n-m-s} (v^* v)^{n-s} (u^* u)^s , \end{aligned} \tag{4.1}$$

where the spinor coordinates are

$$u = \cos(\theta/2) e^{-i\varphi/2} \text{ and } v = \sin(\theta/2) e^{i\varphi/2} \tag{4.2}$$

in terms of the usual polar coordinates $\Omega = (\theta, \varphi)$ on the sphere. $\binom{n}{k}$ is the binomial coefficient. The normalization constant N_{qnm} is

$$N_{qnm} = \sqrt{\frac{2q+2n+1}{4\pi} \frac{(q+n-m)!(q+n+m)!}{n!(2q+n)!}}. \tag{4.3}$$

$l = q+n$ is the angular momentum quantum number associated with L^2 and m is the angular momentum quantum number associated with L_z.

4.4.2 Warm-up: Filled LLL

Let us start by considering a single layer of quantum Hall fluid. In second quantized notation, the filled LLL, i.e. the $\nu = 1$ state, is written as

$$|\Psi_{\nu=1}\rangle = \prod_m c_m^\dagger |0\rangle, \tag{4.4}$$

where $c_m^\dagger$ creates an electron in orbital m and $|0\rangle$ is the vacuum with no electrons. To write down the corresponding wavefunction in real space, we consider N electrons on the sphere, with coordinates $\Omega_i = (\theta_i, \varphi_i)$, where $i = 1, \ldots, N$. The LLL eigenstates on the sphere in the presence of $N_\phi = 2q$ flux quanta are the monopole harmonics $Y_{q,0,m}(\Omega)$, where $m = -q, \ldots, q$. Note that in the LLL, the single-particle wavefunction will depend only on u and v and not on u^* and v^*. For a single layer, the $\nu = 1$ Laughlin state is then given by filling all $N = 2q + 1$ orbitals, i.e.

$$\Psi_{\nu=1}(\{\Omega\}) = \det \begin{pmatrix} Y_{-q}(\Omega_1) & \ldots & Y_{-q}(\Omega_N) \\ \vdots & & \vdots \\ Y_q(\Omega_1) & \ldots & Y_q(\Omega_N) \end{pmatrix}, \tag{4.5}$$

where we have introduced the shorthand $Y_m(\Omega) \equiv Y_{q,0,m}(\Omega)$. Now from the definition of the monopole harmonics (4.1)

$$Y_{q,0,m}(\Omega) \sim u^{q+m} v^{q-m}, \tag{4.6}$$

where we have omitted phase factors and normalization constants and u and v are the usual spinor coordinates. Using this, we obtain the form

$$\Psi_{\nu=1}(\{\Omega\}) = \prod_{i<j} (u_i v_j - v_i u_j) \equiv \prod_{i<j} (\Omega_i - \Omega_j), \tag{4.7}$$

where the last equality introduces a shorthand notation that we will find convenient in the following. This form can be related to the standard form in complex planar coordinates $z_i = x_i + i y_i$, viz. $\Psi_{\nu=1}(\{z\}) = \prod_{i<j}(z_i - z_j)$ by using the stereographic projection

$z_i = 2Rv_i/u_i$. Recall the definition of the shift $\mathcal{S}$

$$N_\phi = \frac{N}{\nu} - \mathcal{S} = N - \mathcal{S} \tag{4.8}$$

for $\nu = 1$. So the filled LLL has shift $\mathcal{S} = 1$.

4.4.3 Composite Fermi liquid (CFL)

Let us consider an isolated layer with $N_\uparrow$ electrons and N_ϕ flux quanta. The CFL for a single isolated layer occurs for $N_\phi = 2q = 2\,(N_\uparrow - 1)$ and hence $\mathcal{S} = +2$. It is clear from this, that for a single layer CFL, we need q to be integer. The CFL has $N_\uparrow = \frac{N_\phi}{2} + 1$ electrons. We attach two flux quanta to each electron to obtain a composite fermion as shown in Fig. 4.3a. An electron does not experience flux attached to itself i.e. the flux attachment procedure leads to a change in flux of $N_{\text{flux attached}} = 2(N_\uparrow - 1) = N_\phi$. Thus the CFs experience a net flux of $N_\phi^{\text{eff}} = 2Q = N_\phi - N_{\text{flux attached}} = 0$. Since the CFs experience no net flux, they are described by the ordinary spherical hamonics instead of the monopole harmonics and so the nth CF shell contains $2n + 1$ states. For example, for $N_\uparrow = 4$ we have two filled CF shells ($n = 0$ and $n = 1$). The CFL will just be a Slater determinant of the CF orbitals for the filled shells. For other $N_\uparrow$ we have one partially filled shell, which we fill according to Hund's rule [241] (maximize total angular momentum).

We can write down related CFL states even when the CFs experience a net effective flux $2Q$ by simply filling CF orbitals. Once we have decided which states to fill, we can write down a single Slater determinant and attach the flux quanta via the usual Jastrow factor

$$\Psi_{\text{CFL}}(\{\Omega\}) = \mathcal{P}_{\text{LLL}}\Big[\mathcal{J}(\{\Omega\})\,\text{Det}\left[Y_i\left(\Omega_j\right)\right]\Big], \tag{4.9}$$

where i is a shorthand for the indices (Q, n, m) of the filled states, bearing in mind that the flux Q will be the same for all states we decide to fill. The Jastrow factor is

$$\mathcal{J}(\{\Omega\}) = \prod_{j<k}\left(u_j v_k - v_j u_k\right)^2 e^{i(\varphi_j+\varphi_k)} = \prod_j J_j(\{\Omega\}), \tag{4.10}$$

where

$$J_j(\{\Omega\}) = \prod_{k\neq j} (u_j v_k - v_j u_k)\, e^{i(\varphi_j+\varphi_k)/2}. \tag{4.11}$$

The LLL projection $\mathcal{P}_{\text{LLL}}$ is necessary because the CFs feel a reduced flux and hence fill higher LL states. From the paper by Jain and Kamilla [240] we use the trick to project the single particle states (together with the Jastrow factor J_j) to the LLL. The single Slater determinant of states that are all in the LLL will obviously be in the LLL as well. Computationally this is a necessary simplification and the resulting states have a high overlap with the states obtained when the LLL projection is done properly. The projected single particle states $\tilde{Y}_{Q,n,m}(\Omega_j)$ are defined via

$$\mathcal{P}_{\text{LLL}}\Big[\text{Det}\left[J_j(\{\Omega\})Y_i(\Omega_j)\right]\Big] \approx \text{Det}\left[\mathcal{P}_{\text{LLL}}J_j(\{\Omega\})Y_i(\Omega_j)\right] \equiv \text{Det}\Big[J_j(\{\Omega\})\tilde{Y}_i(\Omega_j)\Big] \tag{4.12}$$

and the explicit expression is

$$\begin{aligned}\widetilde{Y}_{Q,n,m}(\Omega_j) =& N_{Qnm}(-1)^{Q+n-m}\frac{(2q+1)!}{(2q+n+1)!}u_j^{Q+m}v_j^{Q-m}e^{iq\varphi_j} \\ &\times\sum_{s=0}^{n}(-1)^s\binom{n}{s}\binom{2Q+n}{Q+n-m-s}v_j^{n-s}u_j^s R_j^{s,n-s},\end{aligned} \tag{4.13}$$

where $q = Q + (N_\uparrow - 1)$. The definition of $R_j^{s,n-s}$ is [240]

$$R_j^{s,n-s} = \mathbf{U}_j^s\mathbf{V}_j^{n-s}1 \tag{4.14}$$

with

$$\begin{aligned}\mathbf{U}_j &= 2\sum_{k\neq j}\frac{v_k}{u_j v_k - v_j u_k} + \frac{\partial}{\partial u_j} \\ \mathbf{V}_j &= 2\sum_{k\neq j}\frac{-u_k}{u_j v_k - v_j u_k} + \frac{\partial}{\partial v_j}\end{aligned} \tag{4.15}$$

and the normalization constant N_{qnm} is given by (4.3). Note that the LLL projected single-particle orbitals in general depend on *all* electron coordinates. A good approximation for the CFL is then

$$\tilde{\Psi}_{\text{CFL}}(\{\Omega\}) = \prod_{i<j}(\Omega_i - \Omega_j)^2 \det\left[\widetilde{Y}_i(\Omega_j)\right]. \tag{4.16}$$

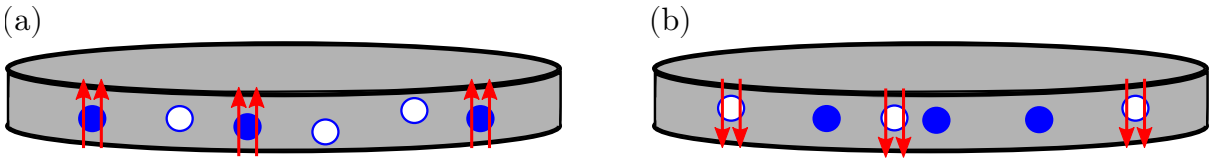

Figure 4.3: Two alternative descriptions of the half-filled LLL. (a) We can attach two flux quanta to each electron, in order to form CFs. The CFs experience no net magnetic field and hence form a Fermi liquid state. This is the CFL. (b) We can attach two flux quanta to each hole, in order to form ACFs. Since the holes have opposite charge to the electrons, we must attach the statistical flux in the opposite direction in order for the ACFs to not experience any net magnetic field. We obtain the ACFL when the ACFs form a Fermi liquid state. The CFL and ACFL are particle-hole conjugates of each other and are not identical.

In the bilayer case, we will always work in the flux sector of the 111 state, i.e. $N_\phi = 2N_1 - 1$ in the balanced case and hence after attaching two flux quanta to each electron we have one leftover flux quantum and hence $Q = \frac{1}{2}$ for the CFs. For filled shell configurations (e.g. $N_1 = 6$), the CFL for two layers is just obtained by the tensor product of the individual layers. For cases with unfilled shells, the total state for the two layers is obtained by first maximizing the orbital angular momentum of each layer according to Hund's rule and then pairing the two layers up to obtain an $L^2 = 0$ state using the appropriate Clebsch-Gordan coefficients.

4.4.4 Anti-composite Fermi liquid (ACFL)

Now we consider the particle-hole conjugate of the CFL, which we dub anti-CFL (ACFL), pictured in Fig. 4.3b. Let us particle-hole conjugate the bottom layer. $\Omega_1^\downarrow, \cdots, \Omega_{N_\downarrow}^\downarrow$ are the coordinates of electrons in the bottom layer and $\varpi_1^\downarrow, \cdots, \varpi_{M_\downarrow}^\downarrow$ are coordinates of holes in the bottom layer. We have $N_\downarrow + M_\downarrow = N_\phi + 1$.

In terms of the hole coordinates, the ACFL wavefunction is just given by a complex conjugation $\Psi^*_{\text{CFL}}(\{\varpi\})$. If we want to write this wavefunction in terms of electron coordinates, we perform the particle-hole transformation [242]

$$\Psi_{\text{ACFL}}(\{\Omega\}) = \sqrt{\frac{(N_\downarrow + M_\downarrow)!}{N_\downarrow! M_\downarrow!}} \int [d\varpi] \Psi_{\nu=1}(\{\Omega\}, \{\varpi\}) \Psi^*_{\text{CFL}}(\{\varpi\}). \tag{4.17}$$

[243] shows that the CFL and its PH conjugate have very high overlap for all system sizes

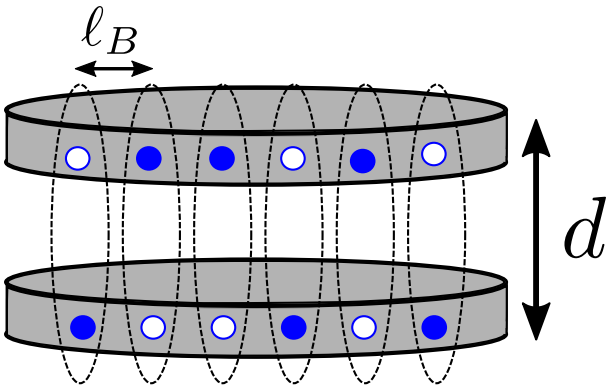

Figure 4.4: The 111 state describes an exciton condensate of electrons and holes.

considered.

The CFL has $N_\uparrow = \frac{N_\phi}{2} + 1$ electrons (and hence the same number of composite fermions). The filled LLL has $N_e = N_\phi + 1$ electrons. Therefore, the ACFL has $N_\downarrow = \frac{N_\phi}{2}$ electrons and consequently $N_{\downarrow,\text{holes}} = \frac{N_\phi}{2} + 1$, which of course is the same as the number of electrons in CFL. The state is given by the Slater determinant of single-particle wavefunctions of the holes

$$\Psi^*_{\text{CFL}}(\{\varpi\}) = \mathcal{P}_{\text{LLL}}\left[\mathcal{J}^*(\{\varpi\})\,\text{Det}\left[Y_i^*\left(\varpi_j\right)\right]\right], \tag{4.18}$$

where ϖ_j is the coordinate of a hole. Beware that since ϖ_j are hole coordinates, $\mathcal{P}_{\text{LLL}}$ yields a wavefunction that depends only on ϖ_j^*. In analogy with the the Jain and Kamilla procedure, we want to project the single-particle states.

$$\widetilde{\Psi}^*_{\text{CFL}}(\{\varpi\}) = \prod_{i<j}(\varpi_i^* - \varpi_j^*)^2\,\text{Det}\left[\widetilde{Y}_i^*\left(\varpi_j\right)\right]. \tag{4.19}$$

4.4.5 111 state

We now consider two layers of quantum Hall fluid with zero interlayer separation and at total filling factor $\nu = 1$. In this limit the problem has an enhanced $SU(2)$ pseudospin symmetry. The exact ground state in that case is the 111 state: Each orbital m is occupied either with an electron in the top layer or the bottom layer (Fig. 4.4). In second

quantized notation, the 111 state is written as

$$|\Psi_{111}\rangle = \prod_m (c^\dagger_{m\uparrow} + e^{i\theta} c^\dagger_{m\downarrow})|0\rangle, \tag{4.20}$$

where $|0\rangle$ is the vacuum where both layers are unoccupied and $c^\dagger_{m\sigma}$ creates an electron in orbital m and layer σ. The relative phase difference θ corresponds to the orientation of the pseudospin in the xy plane and results in a Goldstone mode. Let $N_\uparrow$ and $N_\downarrow$ be the number of electrons in the top and bottom layer respectively. The number of flux quanta is $N_\phi = 2q$. Then the wavefunction as written has definite total particle number $N = N_\uparrow + N_\downarrow = N_\phi + 1 = 2q + 1$ but indefinite pseudospin $S_z = \frac{N_\uparrow - N_\downarrow}{2}$. So to consider a fixed particle number in each layer, we need to project this wavefunction down to a sector with fixed pseudospin. We can consider the 111 state for both the cases of a balanced ($N_\uparrow = N_\downarrow = N_1$) and an imbalanced ($N_\uparrow \neq N_\downarrow$) bilayer. Since $N = N_\phi + 1$ the 111 state has shift $\mathcal{S} = 1$.

Let us now consider this wavefunction in the position representation. In particular, electron coordinates in the top layer will be $\Omega^\uparrow_i = (u^\uparrow_i, v^\uparrow_i)$ with $i = 1, \ldots, N_\uparrow$. The electron coordinates in the bottom layer will be $\Omega^\downarrow_i = (u^\downarrow_i, v^\downarrow_i)$ with $i = 1, \ldots, N_\downarrow$. The 111 state is obtained as

$$\Psi_{111}(\{\Omega^\uparrow\}, \{\Omega^\downarrow\}) = \det \begin{pmatrix} Y_{-q}(\Omega^\uparrow_1) & \ldots & Y_{-q}(\Omega^\uparrow_{N_\uparrow}) & Y_{-q}(\Omega^\downarrow_1) & \ldots & Y_{-q}(\Omega^\downarrow_{N_\downarrow}) \\ \vdots & & \vdots & \vdots & & \vdots \\ Y_q(\Omega^\uparrow_1) & \ldots & Y_q(\Omega^\uparrow_{N_\uparrow}) & Y_q(\Omega^\downarrow_1) & \ldots & Y_q(\Omega^\downarrow_{N_\downarrow}) \end{pmatrix}. \tag{4.21}$$

We are using the shorthand $Y_m(\Omega) \equiv Y_{q,0,m}(\Omega)$. Using (4.6) this results in

$$\Psi_{111}(\{\Omega^\uparrow\}, \{\Omega^\downarrow\}) = \prod_{i<j} \left(u^\uparrow_i v^\uparrow_j - u^\uparrow_j v^\uparrow_i\right) \prod_{i<j} \left(u^\downarrow_i v^\downarrow_j - u^\downarrow_j v^\downarrow_i\right) \prod_{i,j} \left(u^\uparrow_i v^\downarrow_j - u^\downarrow_j v^\uparrow_i\right) \tag{4.22}$$

$$= \prod_{i<j} (\Omega^\uparrow_i - \Omega^\uparrow_j) \prod_{i<j} (\Omega^\downarrow_i - \Omega^\downarrow_j) \prod_{i,j} (\Omega^\uparrow_i - \Omega^\downarrow_j), \tag{4.23}$$

where in the last line we introduced the shorthand notation again. The 111 wavefunction is an $L^2 = 0$ state on the sphere and hence $|\Psi_{111}(\mathcal{R}\Omega^\uparrow, \mathcal{R}\Omega^\downarrow)| = |\Psi_{111}(\Omega^\uparrow, \Omega^\downarrow)|$, where $\mathcal{R}$ is a rotation. To see that note that we have filled all the angular momentum states

(the fact that we have two layers is irrelevant for this argument). The parity under layer exchange for the balanced case is $(-1)^{N_1}$. To see that note that last term in (4.22) is a product of N_1^2 terms and will hence be even or odd under layer exchange, depending on whether N_1^2 (and hence N_1) is even or odd.

The 111 state can also be re-written as

$$|\Psi_{111}\rangle = \prod_m (1 + e^{-i\theta} c^\dagger_{m\uparrow} c_{m\downarrow})|0'\rangle, \tag{4.24}$$

where $|0'\rangle$ is the vacuum where the top layer is empty and the bottom layer is a filled LLL. In terms of electron coordinates in the top layer and hole operators in the bottom layer, we find

$$\Psi_{111}(\{\Omega^\uparrow\}, \{\varpi^\downarrow\}) = \det\left[\sum_{m=-q}^{q} Y_{q,0,m}(\Omega_i^\uparrow) Y^*_{q,0,m}(\varpi_j^\downarrow) \right]. \tag{4.25}$$

4.4.6 Hamiltonian

We will now derive the Hamiltonian, which we will then diagonalize using ED. Two useful references are [227, 244]. The kinetic energy is quenched in the LLL and therefore the Hamiltonian contains only the Coulomb interaction term. The Coulomb interaction between an electron in layer σ with position $\mathbf{r}$ and an electron in layer σ' with position $\mathbf{r}'$ is

$$V_{\sigma\sigma'}(\mathbf{r}, \mathbf{r}') = \frac{e^2}{4\pi\epsilon\sqrt{|\mathbf{r} - \mathbf{r}'|^2 + (1 - \delta_{\sigma\sigma'})d^2}}, \tag{4.26}$$

where $|\mathbf{r} - \mathbf{r}'|$ is the arc distance on the sphere. This expression covers both the intralayer ($\sigma = \sigma'$) and the interlayer interaction ($\sigma \neq \sigma'$). The Hamiltonian is then

$$H =: \mathcal{P}_{\text{LLL}} \frac{1}{2} \sum_{\sigma,\sigma'} \int d^2\mathbf{r} \int d^2\mathbf{r}' \rho_\sigma(\mathbf{r}) V_{\sigma\sigma'}(\mathbf{r}, \mathbf{r}') \rho_{\sigma'}(\mathbf{r}') \mathcal{P}_{\text{LLL}} :, \tag{4.27}$$

where $\rho_\sigma(\mathbf{r}) = \psi^\dagger_\sigma(\mathbf{r})\psi_\sigma(\mathbf{r})$ is the electron number density in layer $\mathbf{r}$ and

$$\psi^\dagger_\sigma(\mathbf{r}) = \sum_{nm} Y_{qnm}(\Omega) c^\dagger_{nm\sigma}, \tag{4.28}$$

where $c^\dagger_{nm\sigma}$ creates an electron in the orbital labelled by (n, m) in layer σ. After projecting to the LLL

$$H = \frac{1}{2}\sum_{\sigma,\sigma'}\sum_{m_1,m_2,m_3,m_4} c^\dagger_{m_1\sigma}c^\dagger_{m_2\sigma'}c_{m_4\sigma'}c_{m_3\sigma}\left\langle m_1, m_2|V_{\sigma\sigma'}|m_3, m_4\right\rangle, \tag{4.29}$$

where $c^\dagger_{m\sigma} \equiv c^\dagger_{0m\sigma}$ are the LLL electron operators. Since the Coulomb interaction only depends on the relative coordinates and is rotationally invariant, we can fully specify the interaction in terms of the Haldane pseudopotentials V_L, where $L = 0, \ldots, 2q$. Using

$$\langle L'M'|V_{\sigma\sigma'}|LM\rangle = \delta_{MM'}\delta_{LL'}V^L_{\sigma\sigma'} \tag{4.30}$$

the interaction matrix element is then

$$\langle m'_1, m'_2|V_{\sigma\sigma'}|m_1, m_2\rangle = \sum_{L=0}^{2q}\sum_{M=-L}^{L}\langle qm'_1, qm'_2|LM\rangle\, V^L_{\sigma\sigma'}\,\langle LM|qm_1, qm_2\rangle, \tag{4.31}$$

where $\langle LM|qm_1, qm_2\rangle$ are the Clebsch-Gordan coefficients and the Haldane pseudopotentials are[245]

$$V^L_{\sigma\sigma'} = \frac{\int d\Omega_1 \int d\Omega_2 \left|u_1\right|^{2L}\left|u_2\right|^{2L}\left|u_1v_2 - u_2v_1\right|^{4q-2L} V_{\sigma\sigma'}(u_1, v_1, u_2, v_2)}{\int d\Omega_1 \int d\Omega_2 \left|u_1\right|^{2L}\left|u_2\right|^{2L}\left|u_1v_2 - u_2v_1\right|^{4q-2L}} \tag{4.32}$$

where

$$V_{\sigma\sigma'}(u_1, v_1, u_2, v_2) = \frac{1}{\sqrt{(2R\left|u_1v_2 - u_2v_1\right|)^2 + (1-\delta_{\sigma\sigma'})d^2}} \tag{4.33}$$

and $R = \sqrt{q}\ell_B$. We need to evaluate this interaction Hamiltonian (4.29) in the basis of many-body states

$$|m_1\sigma_1, m_2\sigma_2, \ldots, m_N\sigma_N\rangle = c^\dagger_{m_1\sigma_1}\ldots c^\dagger_{m_N\sigma_N}|0\rangle. \tag{4.34}$$

We work in a sector with fixed pseudospin $S_z = \frac{1}{2}\sum_i \sigma_i$. For the ground state, we can focus on the $L_z = \sum_i m_i = 0$ sector of the many-body basis. So we write down the

matrix elements

$$\langle \widetilde{m}_1\sigma_1, \widetilde{m}_2\sigma_2, \ldots, \widetilde{m}_N\sigma_N | \, H \, | m_1\sigma_1, m_2\sigma_2, \ldots, m_N\sigma_N \rangle \tag{4.35}$$

and diagonalize the corresponding matrix either exactly or using the Lanczos algorithm. This is done using the package DiagHam.

4.5 Paired states

4.5.1 p-wave BCS state

Let us first recap the p-wave paired BCS state from Refs. [238, 239], pictured in Fig. 4.5(a). We work in the sector $N = 2q + 1$, where q is a half-integer, such that N is even and we can have $N_\uparrow = N_\downarrow = \frac{N}{2} = q + \frac{1}{2}$. Now we attach flux to the electrons, and an electron does not feel flux attached to itself, thus the additional flux an electron feels due to flux attachment is $2(N_{\uparrow,\downarrow} - 1) = 2q - 1$. This partially cancels the flux $2q$ due to the external magnetic field. Therefore, the CFs still feel one unit of flux i.e. their single-particle states will be the monopole harmonics with $Q = \frac{1}{2}$. For the p-wave pairing of CFs as in[38, 39] the pairing wavefunction is

$$G(\Omega_i^\uparrow, \Omega_j^\downarrow) = \sum_{n=0}^{N_{\mathrm{LL}}-1} g_n \sum_{m=-(n+1/2)}^{n+1/2} (-1)^{\frac{1}{2}+m} Y_{\frac{1}{2},n,m}\left(\Omega_i^\uparrow\right) Y_{\frac{1}{2},n,-m}\left(\Omega_j^\downarrow\right), \tag{4.36}$$

where g_n are variational parameters describing the BCS paired wavefunction and N_{LL} is the number of CF LLs that we choose to fill. The LLL wavefunction is then

$$\Psi_{\mathrm{BCS},p}(\{\Omega^\uparrow\}, \{\Omega^\downarrow\}) = \mathcal{P}_{\mathrm{LLL}} \prod_{i<j} [(\Omega_i^\uparrow - \Omega_j^\uparrow)^2 (\Omega_i^\downarrow - \Omega_j^\downarrow)^2] \det[G(\Omega_i^\uparrow, \Omega_j^\downarrow)]. \tag{4.37}$$

However, performing the LLL projection when computing this wavefunction will be too expensive numerically and hence we resort to the procedure described in[240]. The wave-

function is then

$$\tilde{\Psi}_{\mathrm{BCS},p}(\{\Omega^{\uparrow}\},\{\Omega^{\downarrow}\}) = \prod_{i<j}[(\Omega_i^{\uparrow}-\Omega_j^{\uparrow})^2(\Omega_i^{\downarrow}-\Omega_j^{\downarrow})^2]\det[\tilde{G}(\Omega_i^{\uparrow},\Omega_j^{\downarrow})] \tag{4.38}$$

with

$$\tilde{G}(\Omega_i^{\uparrow},\Omega_j^{\downarrow}) = \left[\sum_{n=0}^{N_{\mathrm{LL}}-1}\sum_{m=-(n+1/2)}^{n+1/2}(-1)^{\frac{1}{2}+m}g_n\tilde{Y}_{\frac{1}{2},n,m}\left(\Omega_i^{\uparrow}\right)\tilde{Y}_{\frac{1}{2},n,-m}\left(\Omega_j^{\downarrow}\right)\right]. \tag{4.39}$$

Note that the p-wave wavefunctions described here are putatively the same as those Ref. [39]. However, detailed comparison will show that the overlaps with exact diagonalization we obtain here are somewhat better, particularly at small d, given the same number (or even fewer) variational parameters. In the present work we use a global optimization algorithm (dual annealing[246]) to optimize the overlaps. Ref. [39] used a gradient descent algorithm, which may only find a local optimum of the overlap.

When we have a filled shell configuration, the p-wave state reproduces the large d CFL, if we set $g_n \neq 0$ for occupied shells and $g_n = 0$ for empty shells. If we are one CF away from a filled shell configuration, we also reproduce the Hund's rule state by picking $g_n \neq 0$ for filled shells, $g_r \ll g_0,\ldots,g_{r-1}$ for the rth shell which is partially filled and $g_n = 0$ for $n > r$. If we are more than one CF away from a filled shell configuration however, the trial state does not capture the large d limit. The number of CFs in the valence shell is sub-extensive and hence this effect will become less important for larger system sizes.

4.5.2 New s-wave paired BCS state

Recently, there has been renewed attention on the problem of particle-hole symmetry in the half-filled LLL[247]. The HLR theory of composite fermions manifestly breaks particle-hole symmetry, since we attach flux to the electrons but not to the holes. We can create a different composite particle, the anti-composite fermion, by attaching flux to the holes instead. The question then arises, should we view the half-filled LLL as a CFL or an ACFL? In light of this question, we consider particle-hole transforming one of the two layers of the bilayer system. We think of a CFL in the top layer and an ACFL

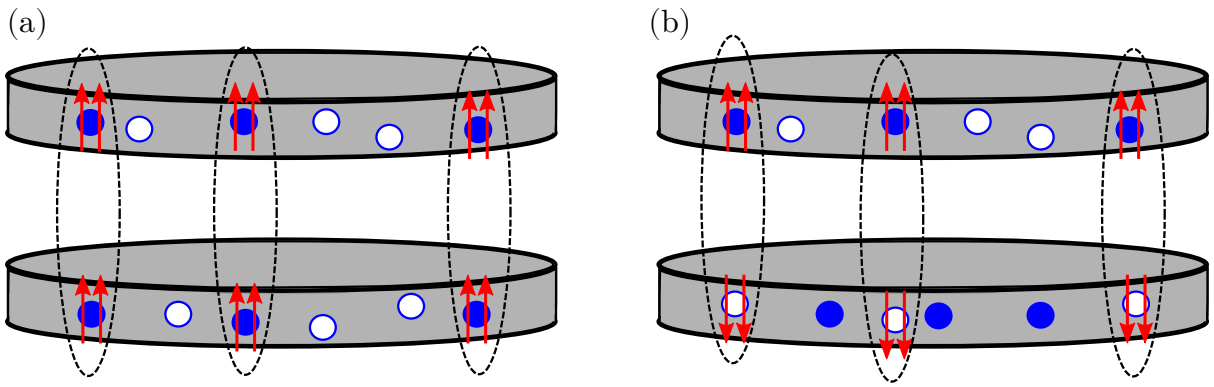

Figure 4.5: BCS trial wavefunctions for the bilayer quantum Hall system. (a) p-wave pairing of CFs in one layer with CFs in the opposite layer. (b) s-wave pairing of CFs in one layer with ACFs in the opposite layer.

in the bottom layer, and again we can consider a BCS-type pairing instability.

We consider the new state shown in Fig. 4.5(b). The pairing function for pairing the CFs in the top layer with the ACFs in the bottom layer in the s-wave channel is

$$G(\Omega_i^{\uparrow}, \varpi_j^{\downarrow}) = \sum_{n=0}^{N_{\rm LL}-1} g_n \sum_{m=-(n+1/2)}^{n+1/2} Y_{\frac{1}{2},n,m}\left(\Omega_i^{\uparrow}\right) Y^*_{\frac{1}{2},n,m}\left(\varpi_j^{\downarrow}\right). \tag{4.40}$$

and the trial wavefunction is obtained by adding the Jastrow factors and performing the LLL projection

$$\Psi_{{\rm BCS},s}(\{\Omega^{\uparrow}\},\{\varpi^{\downarrow}\}) = \mathcal{P}_{\rm LLL}\prod_{i<j}[(\Omega_i^{\uparrow}-\Omega_j^{\uparrow})^2(\varpi_i^{\downarrow}-\varpi_j^{\downarrow})^{*2}]\det[G(\Omega_i^{\uparrow},\varpi_j^{\downarrow})]. \tag{4.41}$$

This wavefunction describes pairing of CFs and ACFs. This time after the Jain and Kamilla procedure

$$\tilde{\Psi}_{{\rm BCS},s}(\{\Omega^{\uparrow}\},\{\varpi^{\downarrow}\}) = \prod_{i<j}[(\Omega_i^{\uparrow}-\Omega_j^{\uparrow})^2(\varpi_i^{\downarrow}-\varpi_j^{\downarrow})^{*2}]\det[\tilde{G}(\Omega_i^{\uparrow},\varpi_j^{\downarrow})] \tag{4.42}$$

with

$$\tilde{G}(\Omega_i^{\uparrow}, \varpi_j^{\downarrow}) = \left[\sum_{n=0}^{N_{\rm LL}-1} \sum_{m=-(n+1/2)}^{n+1/2} g_n \tilde{Y}_{\frac{1}{2},n,m}\left(\Omega_i^{\uparrow}\right) \tilde{Y}^*_{\frac{1}{2},n,m}\left(\varpi_j^{\downarrow}\right)\right]. \tag{4.43}$$

In practice we will have to truncate the number of variational parameters. Note that the variational parameters $\{g_n\}$ can always be chosen real.

We can also consider the imbalanced case, where we have $N_1 = N_\uparrow$ electrons in the top layer and $N_\downarrow$ electrons in the bottom layer. The total number of electrons still satisfies $N = N_\uparrow + N_\downarrow = N_\phi + 1$. We define the pseudospin as $2S_z = N_\uparrow - N_\downarrow$. Again we perform a particle-hole transformation on the bottom layer, such that $\Omega_1^\uparrow, \cdots, \Omega_{N_1}^\uparrow$ are coordinates of electrons in the top layer and $\varpi_1^\downarrow, \cdots, \varpi_{N_1}^\downarrow$ are coordinates of holes in the bottom layer. After the flux attachment procedure, the CFs in the top layer and the anti-CFs in the bottom layer feel an effective flux $Q = \frac{1}{2} - S_z$. The trial state is then

$$\tilde{\Psi}_{\mathrm{BCS},s}(\{\Omega^\uparrow\},\{\varpi^\downarrow\}) = \prod_{i<j}[(\Omega_i^\uparrow - \Omega_j^\uparrow)^2(\varpi_i^\downarrow - \varpi_j^\downarrow)^{*2}]\det[\tilde{G}(\Omega_i^\uparrow, \varpi_j^\downarrow)] \tag{4.44}$$

with

$$\tilde{G}(\Omega_i^\uparrow, \Omega_j^\downarrow) = \left[\sum_{n=0}^{N_{\mathrm{LL}}-1}\sum_{m=-(n+Q)}^{n+Q} g_n \tilde{Y}_{Q,n,m}\left(\Omega_i^\uparrow\right)\tilde{Y}^*_{Q,n,m}\left(\varpi_j^\downarrow\right)\right]. \tag{4.45}$$

We note that depending on whether we particle-hole conjugate the majority or minority layer, we may have $Q < 0$ in which case we need to use the expression for $\tilde{Y}$ from Ref. [248]. In this approach, we composite-fermionize the minority carriers in each layer, consistent with the experimental observation that the density of the minority carriers set the Fermi wavevector away from half-filling[249].

One reason to introduce the s-wave paired state is that it makes the connection to the exciton condensate at small d/ℓ_B more clear. At $d/\ell_B = 0$ we know that the Halperin 111 state is the exact ground state. It is an exciton condensate of excitons formed of electrons and holes. The s-wave paired state is an excitonic superconductor formed by pairing CFs and ACFs and it can be modified to reproduce the 111 state. First we imagine that instead of multiplying the wavefunction by the Jastrow factors, we just multiply by the phase of the Jastrow factors. If we consider short-range pairing (in momentum-space this will consist of pairing up to high momenta), then a CF in one layer will sit exactly on top of an ACF in the opposite layer and the phase factors will cancel[250]. The bosons formed by the CFs and ACFs will be uncorrelated excitons as appropriate for the 111 state. This connection to the 111 state is not all all clear for the p-wave trial state, although in [235] it is argued that the p-wave trial state is in fact smoothly connected to the 111 state. The CFs and ACFs are neutral particles with non-zero dipole moment. Due to the flux

attachment procedure, CFs and ACFs feel an attractive interaction and hence it makes sense to pair them up in the s-wave channel.

4.5.3 Symmetry considerations

We use the identities for the monopole harmonics from[251]. In particular

$$Y^*_{q,n,m} = (-1)^{q+m} Y_{-q,n,-m} \tag{4.46}$$

and

$$\sum_m Y_{q,n,m}\left(\theta',\varphi'\right) Y^*_{q',n,m}(\theta,\varphi) = \sqrt{\frac{2(q+n)+1}{4\pi}} Y_{q,n,-q'}(\theta_{12},0) e^{i(q\varphi'-q'\varphi)} e^{-i(q\gamma'+q'\gamma-q'\pi)}, \tag{4.47}$$

where θ_{12} is the chord distance between the two particles and the angle γ is as defined in[38]. First let us consider the symmetry properties of the p-wave paired state. Using these two identities, one can show (after setting $q=-q'=Q$ and doing some relabelling) that

$$\sum_m (-1)^{Q+m} Y_{Q,n,m}\left(\theta',\varphi'\right) Y_{Q,n,-m}(\theta,\varphi) = \sqrt{\frac{2(Q+n)+1}{4\pi}} Y_{Q,n,-Q}\left(\theta_{12},0\right) e^{iQ(\varphi+\varphi')} e^{-iQ(\gamma-\gamma'+\pi)}. \tag{4.48}$$

Now exchange the two particles. Under the exchange (equivalently a half-rotation)

$$\gamma \to \gamma - \pi \qquad \text{and} \qquad \gamma' \to \gamma' + \pi \tag{4.49}$$

such that the pairing wavefunction picks up a phase of $e^{2\pi i Q} = (-1)^{2Q}$ under the exchange. For the balanced bilayer, we have $Q=\frac{1}{2}$ and so the sign is consistent with what one would require for a pairing wavefunction with odd ℓ. $Y_{Q,n,-Q}\left(\theta_{12},0\right) \sim \theta_{12}^{2Q}$ when $\theta_{12}\to 0$ and so when the pair comes together, the wavefunction indeed vanishes in the correct way for $\ell = 2Q = 1$.

Now let us consider the proposed s-wave paired state. To do that set $q'=q=Q$ in

(4.47) such that

$$\sum_m Y_{Q,n,m}(\theta',\varphi')\, Y^*_{Q,n,m}(\theta,\varphi) = \sqrt{\frac{2(Q+n)+1}{4\pi}} Y_{Q,n,Q}(\theta_{12},0) e^{iQ(\varphi'-\varphi)} e^{-iQ(\gamma'+\gamma-\pi)}. \tag{4.50}$$

Under the exchange (4.49), there is no additional phase picked up. In addition $Y_{Q,n,Q}(\theta_{12},0) \to$ const. as $\theta_{12} \to 0$. So indeed this is consistent with s-wave pairing.

4.5.4 Paired CB state

In this section we consider a further trial state. We attach one flux quantum to electrons in the top layer to form composite bosons (CBs) and attach one flux quantum to holes in the bottom layer to form anti-CBs and then we pair the CBs and anti-CBs in the s-wave channel. This is similar to the construction proposed in [34], except that we write the state on the sphere and introduce a larger number of variational parameters. As before, we perform a particle-hole transformation on the bottom layer, such that $\Omega_1^\uparrow, \cdots, \Omega_{N_1}^\uparrow$ are coordinates of electrons in the top layer and $\varpi_1^\downarrow, \cdots, \varpi_{N_1}^\downarrow$ are coordinates of holes in the bottom layer. After flux attachment, the CBs will experience flux $\mathcal{Q} = N_1$ in the balanced case. The pairing function for pairing CBs in the top layer and anti-CBs in the bottom layer in the s-wave channel is

$$G(\Omega_i^\uparrow, \varpi_j^\downarrow) = \sum_{n=0}^{N_{\rm LL}-1} g_n \sum_{m=-(n+\mathcal{Q})}^{n+\mathcal{Q}} Y_{\mathcal{Q},n,m}\left(\Omega_i^\uparrow\right) Y^*_{\mathcal{Q},n,m}\left(\varpi_j^\downarrow\right). \tag{4.51}$$

and including the Jastrow factors and performing the LLL projection we find the trial wavefunction

$$\Psi_{\rm CB}(\{\Omega^\uparrow\},\{\varpi^\downarrow\}) = \mathcal{P}_{\rm LLL} \prod_{i<j} [(\Omega_i^\uparrow - \Omega_j^\uparrow)(\varpi_i^\downarrow - \varpi_j^\downarrow)^*] \mathrm{perm}[G(\Omega_i^\uparrow, \varpi_j^\downarrow)]. \tag{4.52}$$

This wavefunction describes pairing of CBs and anti-CBs. This time after the Jain and Kamilla procedure

$$\tilde{\Psi}_{\rm CB}(\{\Omega^\uparrow\},\{\varpi^\downarrow\}) = \prod_{i<j} [(\Omega_i^\uparrow - \Omega_j^\uparrow)(\varpi_i^\downarrow - \varpi_j^\downarrow)^*] \mathrm{perm}[\tilde{G}(\Omega_i^\uparrow, \varpi_j^\downarrow)] \tag{4.53}$$

with

$$\tilde{G}(\Omega_i^{\uparrow}, \varpi_j^{\downarrow}) = \left[\sum_{n=0}^{N_{\mathrm{LL}}-1} \sum_{m=-(n+\mathcal{Q})}^{n+\mathcal{Q}} g_n \tilde{Y}_{\mathcal{Q},n,m}\left(\Omega_i^{\uparrow}\right) \tilde{Y}^*_{\mathcal{Q},n,m}\left(\varpi_j^{\downarrow}\right) \right]. \tag{4.54}$$

Strictly speaking the Jain-Kamilla procedure is not valid for the LLL projection of CB orbitals, however it has been suggested [252] that this remains a good approximation to the correct LLL projection procedure even in this case.

4.5.5 ICCFL

We can write down the ICCFL state of Ref. [36] for a particle number consistent with a filled shell configuration of CF bonding orbitals. For example, for $N_{\uparrow} = N_{\downarrow} = 6$, we have a total of $N = 12$ CFs and hence enough to fill the first three CF shells with $n = 0, 1, 2$. The CFs experience flux $Q = \frac{1}{2}$. The Jain-Kamilla LLL projected wavefunction is then

$$\tilde{\Psi}_{\mathrm{ICCFL}}(\{\Omega^{\uparrow}\}, \{\Omega^{\downarrow}\}) = \prod_{i<j} [(\Omega_i^{\uparrow} - \Omega_j^{\uparrow})^2 (\Omega_i^{\downarrow} - \Omega_j^{\downarrow})^2] \det[\tilde{Y}_i(\Omega_1^{\uparrow}) \dots \tilde{Y}_i(\Omega_{N_{\downarrow}}^{\downarrow})], \tag{4.55}$$

where $i = (Q, n, m)$ runs over the N indices of filled CF orbitals and we take the determinant of an $N \times N$ matrix corresponding to filling the N orbitals with CFs from either layer. This wavefunction has no free variational parameters since we have assumed all CFs are in the bonding orbitals in this state, as predicted by mean-field theory[36]. We also considered the ICCFL wavefunction for the case where we have both bonding and anti-bonding orbitals, however this does not yield significantly improved overlaps.

4.6 Balanced case

We now present the numerical results for the paired states discussed in the previous section. Let us focus on the case where the two layers are balanced, i.e. $\nu_{\uparrow} = \nu_{\downarrow} = 1/2$ and on the sphere the number of electrons per layer is $N_{\uparrow}$. We show the overlaps (Fig. 4.6) and energies (Fig. 4.7) of the two variational BCS states with the ED ground state in for $N_{\uparrow} = 8, 10, 12, 14$ and different numbers of variational parameters. The optimal variational parameters that maximize the overlap are found using a dual annealing algorithm[246].

Given that the Hilbert space dimension of the $L^2 = 0$ subspace in which the ground state and the trial wavefunctions lie is $D(L^2 = 0) = 12, 38, 252, 1599$ respectively, the high overlaps obtained are significant (see App. D for the calculation of $D(L^2 = 0)$). In order to compute the overlaps, we use the position space representation of the exact diagonalization ground state and evaluate the overlap integrals using Monte Carlo, the corresponding Monte Carlo errors are shown as errorbars. For the overlaps, we perform importance sampling using the probability distribution of the 111 state as a sampling function (see App. D for details of the Monte-Carlo procedure). In the figure we also examine the 111 state, as well as the CF Fermi liquid state (two uncoupled CF liquids).

In Figs. 4.6 and 4.7 we show results for different system sizes and different numbers of variational parameters. At small interlayer distances, the 111 state is the exact ground state as expected. At very large distances the CF Fermi liquid (Hund's rule) state is essentially exact. Both the p-wave and the s-wave variational wavefunctions recover the CF Fermi liquid or Hund's rule state for a suitable choice of variational parameters at least when N is such that there are a filled number of shells of CFs, or there is only a single CF in the valence shell or single missing CF in the valence shell. For $N_\uparrow = 4, 8, 9, 10...$ where we have more than one electron in an unfilled shell our trial states do not recover the Hund's rule state.

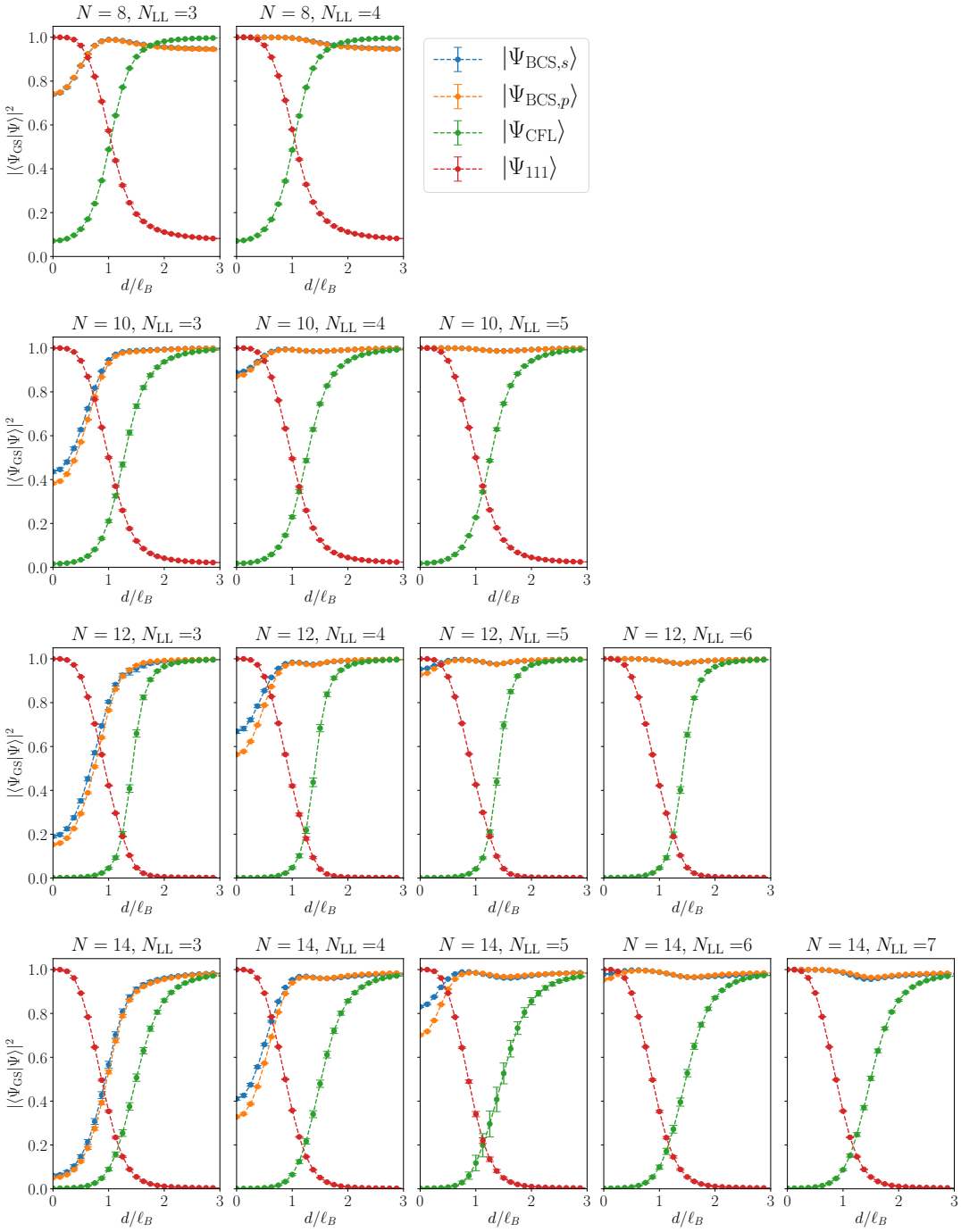

Figure 4.6: Exact diagonalization results for the overlap of the trial wavefunctions with the true ground state for different system sizes and different numbers of variational parameters. We include variational parameters g_n for $n = 0, \ldots, N_{\mathrm{LL}} - 1$, such that the number of variational parameters is $N_{\mathrm{LL}} - 1$ (since an overall rescaling of all g_n results in the same trial wavefunction after normalization). We compare the overlap of our s-wave BCS state with the previously proposed p-wave BCS state of Refs. [38, 39]. The s-wave and p-wave states are taken to have the same number of variational parameters. We also show the overlaps with the CFL state and the 111 state. By CFL we denote either a CF Fermi sea (for $N = 12$) or a Hund's rule state (for other N). Both BCS states can reproduce the CFL at large d, except when there is more than one CF in a partially filled shell (this happens for the $4 + 4$ system size for example).

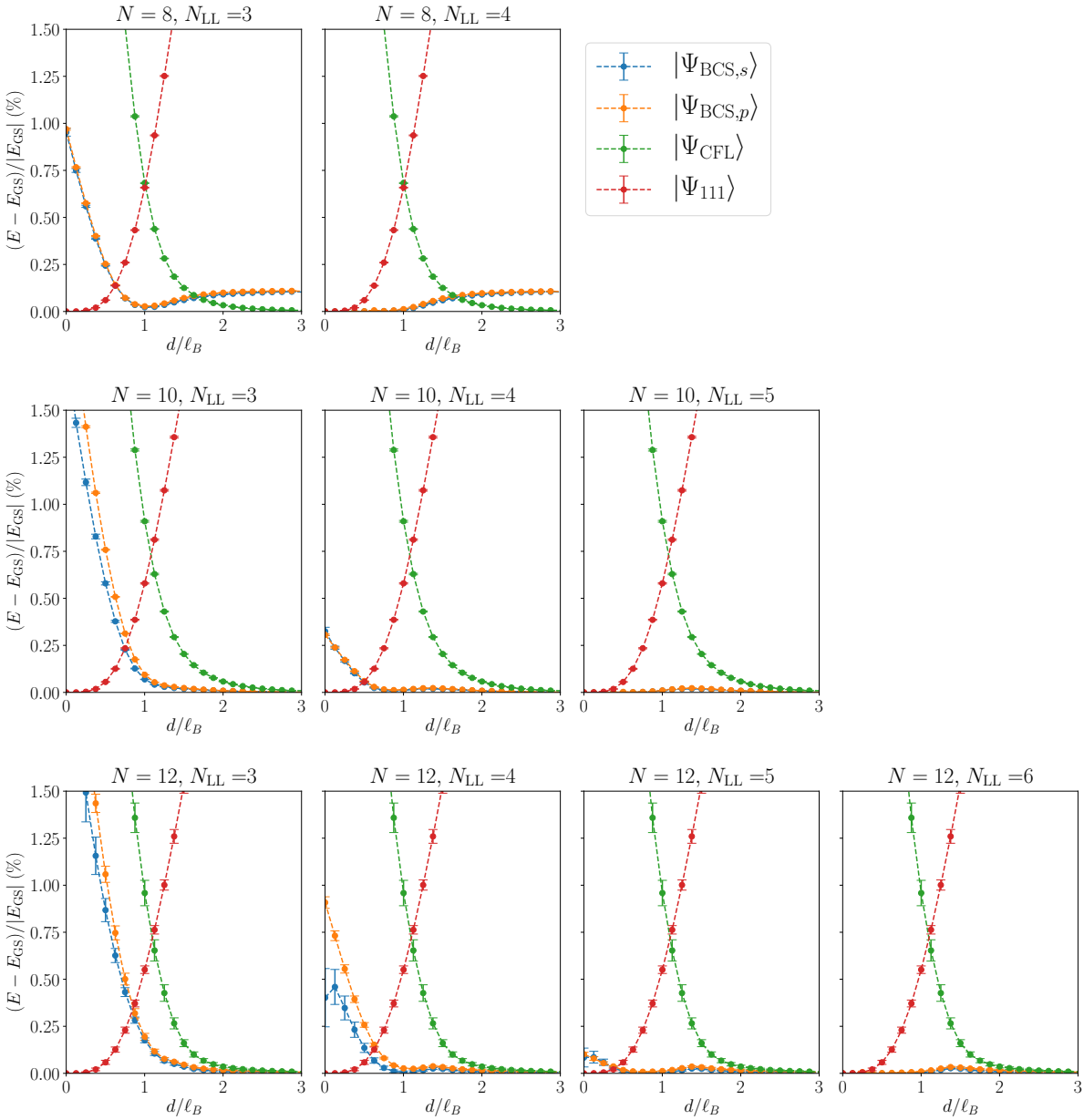

Figure 4.7: Exact diagonalization results for the energy of the trial wavefunctions compared with the true ground state energy for different system sizes and different numbers of variational parameters. We compute the energy of the trial state which has the best overlap with the ED ground state. We also compute the energy of the 111 and the CFL states.

At small interlayer distances, the (111)-state is the exact ground state as expected. Both the p-wave and the s-wave capture this limit as well. As the number of variational parameters is increased, both the s-wave and p-wave overlaps rapidly improve at small d. (In the s-wave picture including more variational parameters allows us to form more tightly bound excitons, hence recovering the (111)-state.) Our s-wave trial wavefunctions

outperform the previous p-wave trial state for an equal number of variational parameters.

In Figs. 4.8 and 4.9 we show the same overlaps and energies for the maximum number of variational parameters employed to show that both trial states capture the 111 state accurately when sufficiently many variational parameters are included.

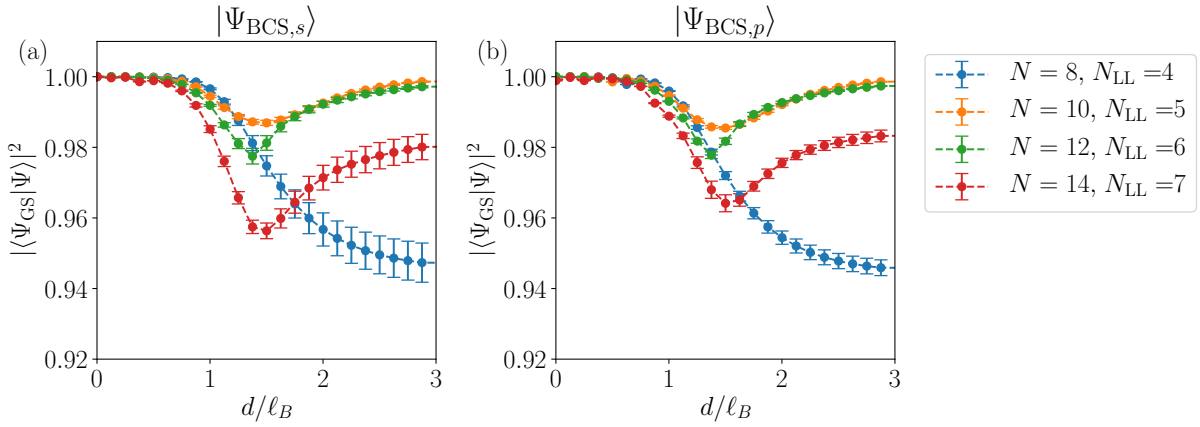

Figure 4.8: Same data as Fig. 4.6, but only for the largest number of variational parameters employed for a given N.

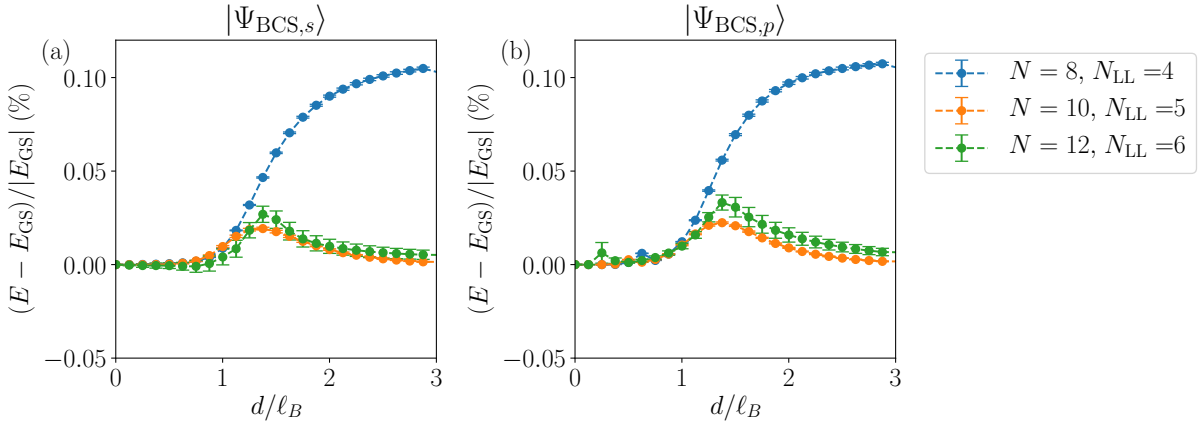

Figure 4.9: Same data as Fig. 4.7, but only for the largest number of variational parameters employed for a given N.

We note that although the s-wave CF/ACF paired state and the p-wave CF/CF paired state have very similar overlaps, they are quite distinct wavefunctions. In the absence of tunnelling, both the total number of electrons and the electron imbalance are conserved separately, giving us a $U_+(1) \times U_-(1)$ symmetry. Let $f^\dagger_{\mathbf{k}\sigma}$ create a CF of momentum $\mathbf{k}$ in layer σ and let $a_{\mathbf{k}\sigma}$ create an anti-CF of momentum $\mathbf{k}$ in layer σ. The p-wave state has an order parameter $\langle f^\dagger_{\mathbf{k}\uparrow} f^\dagger_{-\mathbf{k}\downarrow}\rangle$ which breaks $U_+(1)$, whereas the s-wave state has an order

parameter $\langle f^\dagger_{\mathbf{k}\uparrow} a_{\mathbf{k}\downarrow}\rangle$ which breaks $U_-(1)$. The order parameter for the Halperin 111 state is $\langle \psi^\dagger_\uparrow(\mathbf{r})\psi_\downarrow(\mathbf{r})\rangle$ where $\psi^\dagger$ is the *electron* creation operator. This also breaks $U_-(1)$ but differs from the s-wave order parameter in not having the same Jastrow factors attached. We note that the proposed order parameter from Ref. [36] is $\langle f^\dagger_{\mathbf{k}\uparrow} f_{\mathbf{k}\downarrow}\rangle$ which also breaks $U_-(1)$ but attaches Jastrow factors differently from our s-wave wavefunction and has poor overlap with exact diagonalization for all values of d. In Fig. 4.10a we show the overlap with the ICCFL state of Ref. [36]. The ICCFL states appears to capture some of the relevant correlations around $d \sim \ell_B$, however the overlap does not reach order unity anywhere (this wavefunction has no free variational parameters). In Fig. 4.10b we show the overlap with a paired state of composite bosons described in the section above. This trial state of paired CBs performs well at intermediate distances $d \sim \ell_B$, but does not have high overlaps with the 111 state (consistent with the findings of [34]) and does not capture the CFL at large distances.

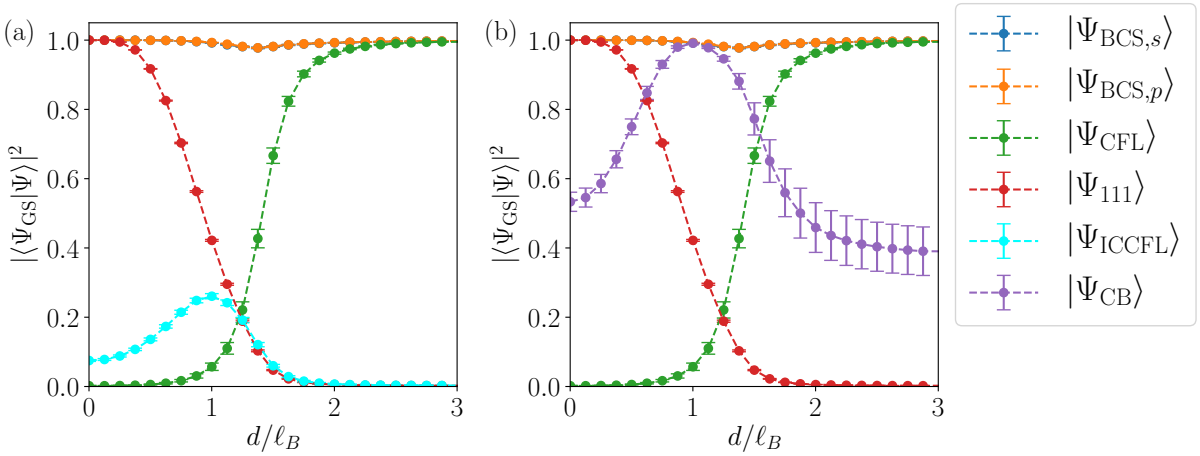

Figure 4.10: Exact diagonalization results for the overlap of the trial wavefunctions with the true ground state for $6+6$ electrons. We compare the overlap of our s-wave BCS state with the previously proposed p-wave BCS state of Refs. [38, 39], the ICCFL state[36] and a paired state of composite bosons/anti-composite bosons similar to the trial state proposed in Ref. [34]. We consider the ICCFL where all CFs are in the bonding orbitals and therefore this wavefunction has no variational parameters. The BCS and CB trial states both have five variational parameters. We also show the overlaps with the CFL state and the 111 state.

4.7 BCS parameters

If we define the CF orbitals including the Jastrow factors as

$$\mathcal{Y}_{Q,n,m}(\Omega_i) = J_i(\{\Omega\})\tilde{Y}_{Q,n,m}(\Omega_i) \tag{4.56}$$

then we can write the trial wavefunction

$$\tilde{\Psi}_{\mathrm{BCS},s}(\{\Omega^{\uparrow}\},\{\varpi^{\downarrow}\}) = \det\Big[\sum_{n=0}^{N_{\mathrm{LL}}-1}\sum_{m=-(n+Q)}^{n+Q} g_n \mathcal{Y}_{Q,n,m}(\Omega_i^{\uparrow})\mathcal{Y}^{*}_{Q,n,m}(\varpi_j^{\downarrow})\Big] \tag{4.57}$$

One subtlety arises regarding the normalization of the CF orbitals $\mathcal{Y}_{Q,n,m}(\Omega_i)$, since these are no longer single-particle wavefunctions. We need to extract the relative normalization of the orbitals with different n. To do so, for example for $N_{\uparrow} = N_{\downarrow} = 4$ we write down the CFL wavefunctions filling the four orbitals in each layer with n given by $(0,0,1,1)$, $(0,0,2,2)$ and $(1,1,2,2)$. We compute the normalization of the CF orbitals $\mathcal{Y}_{Q,n,m}(\Omega_i)$ by computing the ratio of the norm of these many-body CFL wavefunction.

We can translate from angular momentum $l = Q + n$ to linear momentum $k = l/R$, where $R = \sqrt{q}\ell_B$ is the radius of the sphere. Recall the second quantized BCS wavefunction

$$|\Psi_{\mathrm{BCS}}\rangle = \prod_{\mathbf{k}}\left(1 + g_{\mathbf{k}} c^{\dagger}_{\mathbf{k},\uparrow} d^{\dagger}_{\mathbf{k},\downarrow}\right)|0\rangle \tag{4.58}$$

where $|0\rangle$ is the state with the upper layer empty and the LLL of the lower layer filled. Note that we need to project this wavefunction to a definite S_z sector in order to be able to write down the real-space representation. Let us focus on the balanced case, i.e. we choose a set $\{g_{\mathbf{k}}\}$ of orbitals to fill:

$$|\Psi_{\mathrm{BCS}}\rangle = \sum_{\{g_{\mathbf{k}}\}}\prod_{\mathbf{k}}\left(g_{\mathbf{k}} c^{\dagger}_{\mathbf{k},\uparrow} d^{\dagger}_{\mathbf{k},\downarrow}\right)|0\rangle \tag{4.59}$$

where $|\{g_{\mathbf{k}}\}| = N_{\uparrow}$. And now we can calculate the occupation of each orbital according to

$$n_{\mathbf{k}} = \langle c^{\dagger}_{\mathbf{k},\uparrow} c_{\mathbf{k},\uparrow}\rangle = \langle d^{\dagger}_{\mathbf{k},\downarrow} d_{\mathbf{k},\downarrow}\rangle = \frac{\sum_{\{g_{\mathbf{q}}\}\ni g_{\mathbf{k}}}\prod_{\mathbf{q}}(g_{\mathbf{q}})^2}{\sum_{\{g_{\mathbf{q}}\}}\prod_{\mathbf{q}}(g_{\mathbf{q}})^2} \tag{4.60}$$

For an s-wave superconductor, BCS theory predicts

$$n_{\mathbf{k}} = \frac{1}{2}\left(1 - \frac{\varepsilon_{\mathbf{k}}}{\sqrt{\varepsilon_{\mathbf{k}}^2 + \Delta^2}}\right) = \frac{1}{2}\left(1 - \frac{(k\ell_B)^2 - 1}{\sqrt{((k\ell_B)^2 - 1)^2 + (\Delta/E_F)^2}}\right) \tag{4.61}$$

where $\varepsilon_{\mathbf{k}} = \frac{k^2}{2m} - E_F = \frac{(k^2 - k_F)^2}{2m}$, $k_F = \ell_B^{-1}$ and Δ is the superconducting order parameter. The typical size of a Cooper pair is set by the coherence length

$$\xi = \frac{v_F}{\Delta} = \frac{k_F/m}{\Delta} = \frac{2E_F}{\Delta}\ell_B. \tag{4.62}$$

We note that the formulae for $n_{\mathbf{k}}$ and ξ depend only on the ratio Δ/E_F and do not require any assumption about the value of the CF effective mass. We show results for $n_{\mathbf{k}}$ in Fig. 4.11 and extract the BCS parameters as a function of distance in Fig. 4.12. We can interpret these figures as evidence of a BEC-BCS crossover (illustrated in Fig. 4.2). Eq. (4.58) can equally be interpreted as a BEC wavefunction, by re-writing it as

$$|\Psi_{\mathrm{BEC}}\rangle = e^{\sum_{\mathbf{k}} g_{\mathbf{k}} c^\dagger_{\mathbf{k},\uparrow} d^\dagger_{\mathbf{k},\downarrow}}|0\rangle. \tag{4.63}$$

This motivates us to consider a smooth crossover between a BCS-like regime at large interlayer separation and a BEC-like regime at small interlayer separation[250]. At $d/\ell_B \gg 1$, $n_{\mathbf{k}}$ is a sharp step function and the order parameter satisfies $\Delta \ll E_F$. This is the BCS limit. One the other hand, at $d/\ell_B \ll 1$, $n_{\mathbf{k}}$ is a smeared out step function and the order parameter satisfies $\Delta \gg E_F$, which is the BEC limit.

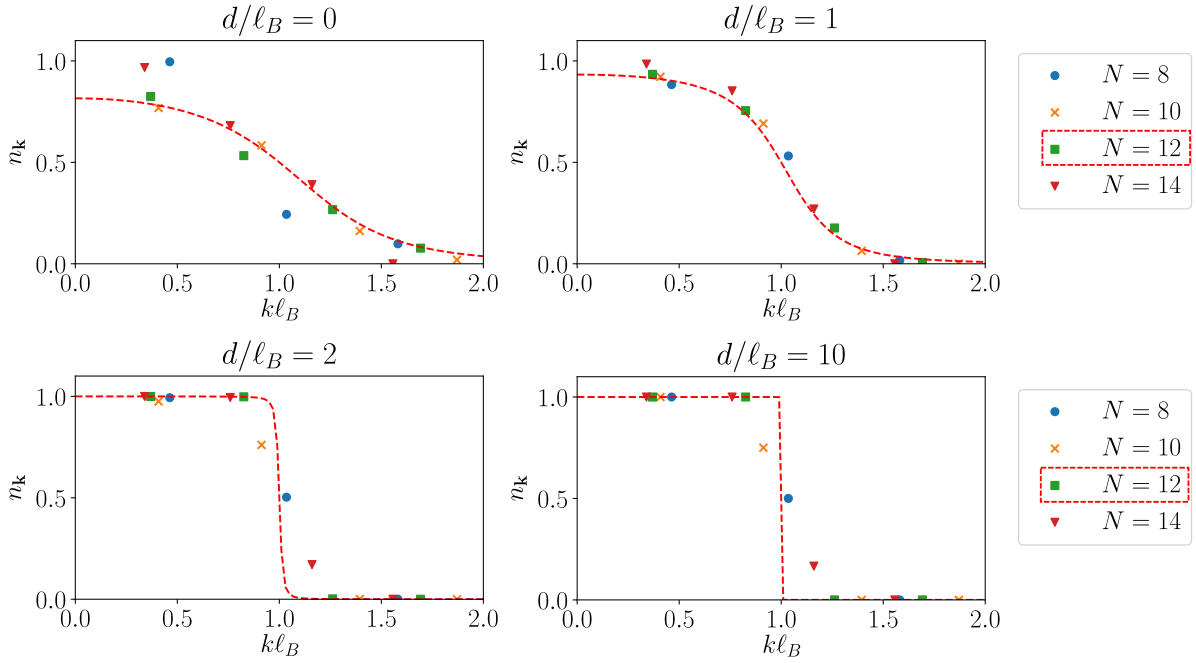

Figure 4.11: Values of the BCS parameters $n_{\mathbf{k}}$ for the best s-wave trial state at four selected interlayer separations d. At large d we have a sharp Fermi surface, whereas at small d we have significant pairing in a large momentum range, which corresponds to tightly bound CF/anti-CF pairs. The dashed line shows the best fit of the BCS form Eq. (4.61). For the fit we only use the $N = 12$ data, since this is a closed shell configuration at large d/ℓ_B. For all N we use 3 variational parameters (i.e. $N_{\mathrm{LL}} = 4$).

4.8 Charge imbalance

We now add a charge imbalance to the two layers, while keeping the total filling fraction constant. The filling fractions of the individual layers are now $\nu_\uparrow = \frac{1+\Delta\nu}{2}$ and $\nu_\downarrow = \frac{1-\Delta\nu}{2}$. After a particle-hole transformation of the bottom layer, we have $N_\uparrow$ CFs in the top layer and $N_\uparrow$ anti-CFs in the bottom layer. We can then pair them up in the s-wave channel. On the other hand, in the imbalanced case the p-wave CF/CF paired state will have a different number of composite fermions in both layers and a pairing wavefunction based on this approach is less natural.

We show the overlaps of our trial state with the ED ground state in Fig. 4.14. For small layer imbalances, our trial wavefunction performs less well at small distances than in the balanced case, however considering the dimension of the Hilbert space, the high overlaps obtained even in the imbalanced case are significant. At large d/ℓ_B, we expect the layers

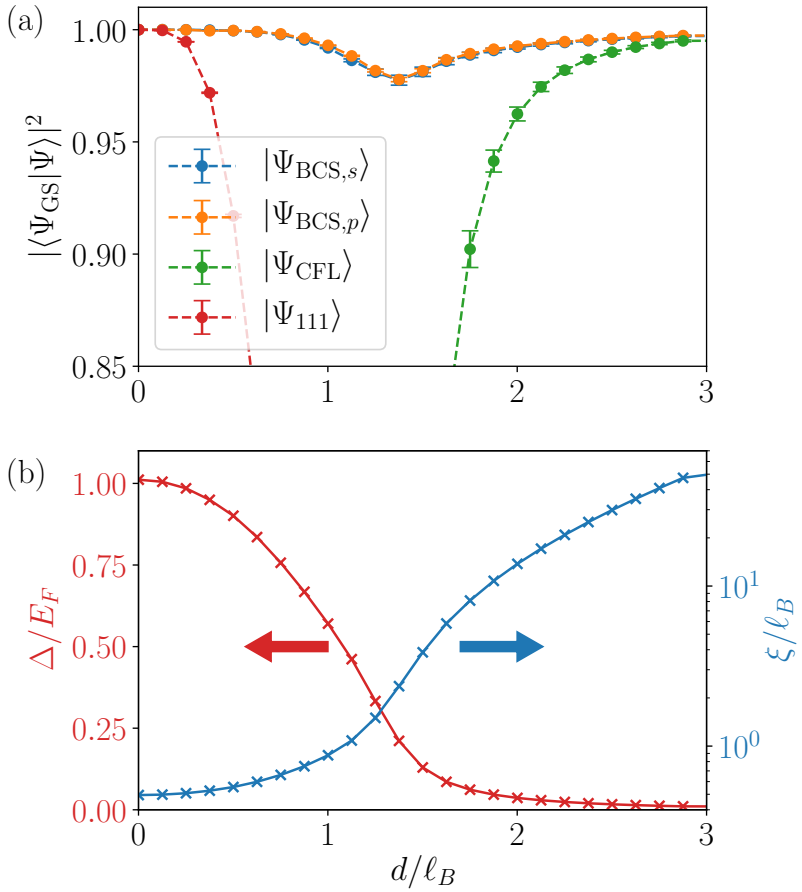

Figure 4.12: Exact diagonalization results for a balanced system with $6+6$ electrons on the sphere. (a) We plot the overlap of the trial wavefunctions with the true ground state $|\Psi_{\rm GS}\rangle$ as a function of the interlayer distance d. We compare the overlap of our s-wave BCS state with the previously proposed p-wave BCS state of [38, 39]. We also show the overlaps with the composite Fermi liquid (CFL) state and the 111 state, which are accurate descriptions of the state in the large and small d limits respectively. The errorbars denote the errors of the Monte-Carlo integration. (b) BCS parameters Δ/E_F and ξ/ℓ_B extracted from the s-wave variational wavefunction from (a). Δ is the s-wave superconducting order parameter, E_F is the Fermi energy and ξ is the coherence length. The evolution of the BCS parameters as a function of the interlayer separation d is consistent with a BEC-BCS crossover.

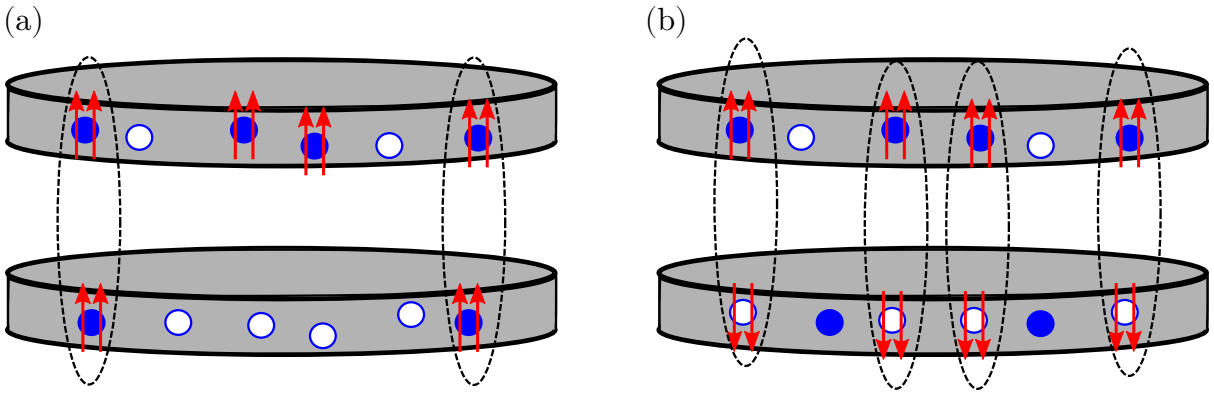

Figure 4.13: Trial wavefunctions in the imbalanced case. (a) The p-wave pairing of CFs in one layer with CFs in the opposite layer. In the imbalanced case we cannot pair up all CFs in Cooper pairs. (b) The s-wave pairing of CFs in one layer with ACFs in the opposite layer. We have an equal density of CFs in the top layer and ACFs in the bottom layer and hence can pair all them up.

to form independent layers of CFs, which will successively fill angular-momentum shells. As mentioned above, our trial wavefunction can describe this accurately as long as the shells are either filled, or have a single CF in them, or are one CF short of being filled. This largely explains why some of the values of $(N_\uparrow, N_\downarrow)$ in Fig. 4.14 are very accurate at large d/ℓ_B and some are inaccurate in this limit.

One can also consider the extension of the p-wave paired state to the imbalanced layer case for certain fillings. In particular, if the states fall on the Jain sequence, viz. $\nu_\uparrow = \frac{p}{2p+1}$ and $\nu_\downarrow = \frac{p+1}{2p+1}$, then we can view the top layer as CFs filling the first p LLs and the bottom layer as CFs filling the first $p+1$ LLs in an opposite effective magnetic field. We can now pair up CFs in the nth CF LL of the bottom layer with CFs in the $(n+1)$th LL of the top layer. In this way, we pair up all the CFs in the bottom layer with CFs in the top layer, for $n = 0$ up to $n = p$, leaving unpaired CFs in the $n = 0$ CF LL of the top layer. This absence of pairing should have little effect on the total energy, (for large p) since these electrons are far from the Fermi energy. We have not investigated this proposal numerically so far and we leave this to future work.

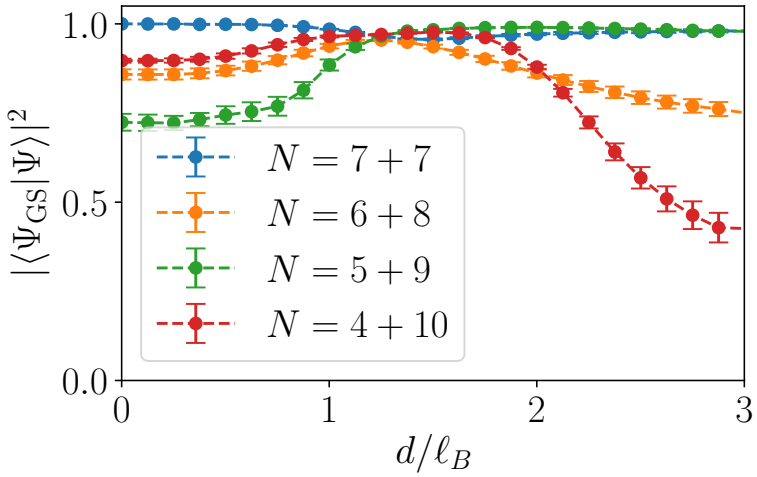

Figure 4.14: Exact diagonalization results for the overlap of the s-wave BCS trial wavefunctions with the true ground state for imbalanced layers. The $L^2 = 0$ Hilbert space dimensions are 1599, 1319, 614, 205 for $7 + 7$, $6 + 8$, $5 + 9$, and $4 + 10$ respectively and we use six variational parameters in all cases.

4.9 Relation to experiment

The experimental results on double layer graphene reported in Ref. [250] support the BEC-BCS crossover picture for the bilayer quantum Hall system that we presented in this chapter. In particular, they explore the finite-temperature physics and see signatures of two distinct temperature scales. The first temperature scale $T_{\rm pair}$ is the temperature below which the Hall drag is quantized. This is the temperature at which the CFs start to pair up into excitons. There is a second temperature T_c which is the temperature below which the counterflow resistance vanishes. This is the temperature below which the excitons condense. At small d/ℓ_B, the experiments observe $T_{\rm pair} \gg T_c$, this is the BEC limit. At large d/ℓ_B, the experiments observe $T_{\rm pair} \sim T_c$, this is the BCS limit.

Experiments have been performed on imbalanced layers in GaAs heterostructures and they observe enhanced superfluid behavior with layer imbalance[196, 195, 194]. We can conjecture the following natural explanation for this. At half-filling the CFs (or anti-CFs) are neutral quasiparticles. Away from half-filling the CFs in the top layer develop charge $e(1 - 2\nu_\uparrow) = e\Delta\nu$, while the anti-CFs in the bottom layer develop charge $e(1 - 2\nu_\downarrow) = -e\Delta\nu$. In the imbalanced case, these two charges can attract to improve

the BCS pairing.

4.10 Conclusion

We proposed a new trial wavefunction for the bilayer quantum Hall system, where CFs and anti-CFs pair up in the s-wave channel. This trial state has high overlaps with the exact ground state for any interlayer separation. In this language, the bilayer system undergoes a BEC-BCS crossover as the interlayer separation is varied. At large d the system is in the BCS limit, with weakly bound CF/anti-CF Cooper pairs, whereas at small d, the system enters the BEC regime with tightly bound CF/anti-CF excitons (which are equivalent to electron/hole excitons in the tightly bound limit, since the phases of the Jastrow factors cancel in the tightly bound limit where the CFs and anti-CFs are at the same position). Our trial state also performs well for imbalanced layers.

It would interesting to extend the numerical study of this problem to larger numbers of electrons. With our system sizes we are reaching the limits of ED and hitting the exponential wall. To go beyond 20 electrons, ED is no longer sufficient and one needs to turn to alternative methods. For example, one could consider using DMRG on a cylinder geometry. In the Landau gauge, we are left with an effectively 1d problem in the orbital basis albeit with long-range interactions. The Coulomb interaction can be approximated as a sum of short-range terms to circumvent this problem. One could consider using the scaling of the entanglement entropy to determine the central charge of the different phases as in [253].

It would be interesting to compute the BCS order parameter for the paired composite fermions directly from the ED (second-quantized) wavefunction. This is a difficult problem due to the fact that the order parameter is written in terms of composite fermions and thus not readily available from the ED results. However, this question should be amenable to the technique used in [254] for the $\nu = 5/2$ state.

The p-wave pairing of HLR CFs corresponds to s-wave pairing of Dirac CFs, due to the Berry phase of the Dirac CFs. In Ref. [235], the authors investigate this picture of s-wave pairing of Dirac CFs to study the problem of BQH. From our work's success, we suggest one can think of a new mechanism of pairing the Dirac composite electrons and

Dirac composite holes. This Dirac composite fermion-Dirac composite hole pairing may provide a new approach to understanding BQH in GaAs and the quantum Hall states of double-layer graphene [255, 256].

In this chapter we considered composite fermions formed by attaching two flux quanta to an electron. These CFs feel no magnetic field when $\nu = 1/2$. However, we could also consider forming an CF by attaching four flux quanta to an electron, these CFs will feel no field when $\nu = 1/4$ and therefore when describing the $3/4 + 1/4$ bilayer QH system these may be the natural degrees of freedom. Similarly we can consider $7/8 + 1/8$ and so on.

Chapter 5

Conclusions

In this thesis we have investigated different types of strongly correlated electronic quantum fluids in two spatial dimensions. We started off by studying graphene. In particular, we were interested in computing the transport properties such as the electrical conductivity and thermal conductivity in bilayer graphene. We used two complementary approaches to describe the transport in bilayer graphene: Kinetic theory and hydrodynamics. In the kinetic theory formalism, we consider the collisions of electrons with each other and with impurities and phonons and hence compute the response of the electrons to an applied electric field or thermal gradient. In the hydrodynamic formalism, we take a more coarse-grained approach and consider a two-fluid model where we have a fluid of electrons and a fluid of holes and they interact with each other via the Coulomb drag. We find that both the kinetic theory and hydrodynamic formalism are good descriptions of bilayer graphene near charge neutrality.

In the second part of the thesis, we considered a different type of quantum fluid. We still consider a two-dimensional electron gas, but this time we switch on a large magnetic field, bringing us into the regime of the quantum Hall effect. This is a different type of quantum fluid, where interaction effects are important. We studied ripples on the edge of this quantum Hall fluid and saw that one can use a quantum dot to excite these modes. However, interaction effects destroyed the precise charge quantization of the current pulses, casting doubt on their use as single-particle sources.

Finally, we turned to the bilayer quantum Hall system, where we couple two quantum Hall fluids and observe the change in the correlations between the layers as the interlayer

separation is tuned. We understand the transition in this system in terms of the BEC-BCS crossover. At larger interlayer separation, we have weakly coupled composite fermion Cooper pairs, as the interlayer separation decreases, the correlations between the layers increase and we reach the BEC limit, where we have tightly bound composite fermion-anti composite fermion excitons.

In the grand scheme of things, we are still in the midst of the challenge of understanding strongly correlated systems. Strongly correlated systems cannot be simply understood from the non-interacting limit and traditional methods such a mean-field theory fail. Many familiar notions such as the presence of long-lived quasiparticles simply do not hold in these systems and therefore they require a paradigm shift in order to be understood.

One starting point to understanding such systems is reduced dimensionality, for example in 1d there are techniques such as integrability or bosonization that are at our disposition. Powerful entanglement-based methods such as DMRG, which exploit the fact that ground states are often weakly entangled have proved enormously useful as well[257].

Another powerful tool is dualities. Certain strongly coupled phases can be mapped to weakly coupled phases that we can understand more easily. A famous example of a duality is the AdS/CFT duality, which relates a quantum CFT on the boundary to a classical string theory in the bulk. AdS/CFT can be used to derived hydrodynamic equations and as we have seen, hydrodynamics is a useful tool to understand strongly correlated phases[258].

At the end of the day, it is likely that to gain a deeper understanding, it will not be sufficient to have a single method. Instead, we will have to use a cornucopia of different approaches—both theoretical methods and experimental probes—, each of them shedding light on a different part of the problem. It is like exploring a dark room at night, we can only illuminate small parts of the room at the same time with our torch and we have piece this information together like a puzzle in order to build a consistent picture of what the room looks like during the day in bright sunlight.

Many challenges still lie ahead and many strongly correlated phases still lie shrouded in mystery. After decades of work, high temperature superconductors like the cuprates

are still poorly understood, they are believed to be described by the Hubbard model, but solving the Hubbard model in 2d is a stupendous problem in itself.

Appendix A

Solving the Boltzmann equation

In this section, we explain how to turn the QBE into a matrix equation. We follow [72]. The linearized Boltzmann equation is

$$-\lambda\beta\frac{e\mathbf{E}\cdot\mathbf{p}}{m}f^0_\lambda(\mathbf{p})[1-f^0_\lambda(\mathbf{p})] = -I_\lambda(\mathbf{p}). \tag{A.1}$$

The suggested ansatz in this calculation is

$$h_\lambda(\mathbf{p}) = \beta\frac{e\mathbf{E}}{m}\cdot\mathbf{p}\chi_\lambda(p). \tag{A.2}$$

We expand in terms of basis functions

$$\chi_\lambda(k) = \beta\sum_n a_n g_n(\lambda,k) \tag{A.3}$$

such that a is dimensionless. Here the basis functions are taken to be

$$g_n(\lambda,k) = 1,\lambda,K,\lambda K,K^2,\lambda K^2,K^3e^{-K/2},\lambda K^3e^{-K/2}...K^Ne^{-K/2},\lambda K^Ne^{-K/2} \tag{A.4}$$

where $K=\sqrt{\beta/m}k$ is the dimensionless momentum. For all powers $n>2$ we multiply by an exponential factor so the basis function is $K^ne^{-K/2}$. We expand in up to 16 basis functions. Increasing the number of basis function changes the results only marginally. Use the fact that this must be valid for all $\mathbf{E}$, sum over λ, multiply by $\hat{\mathbf{p}}g_m(\lambda,p)$ and

integrate over $\mathbf{p}$. This yields an equation that can be summarized in matrix form as

$$M\mathbf{a} = \mathbf{F}, \tag{A.5}$$

where we defined the dimensionless matrices

$$M_{mn} = \beta\left(\frac{\beta}{m}\right)^{3/2} \sum_{\lambda} \int \frac{d^2\mathbf{p}}{(2\pi)^2} g_m(\lambda, p) I_\lambda \Big[h_\lambda(\mathbf{k}) = \hat{\mathbf{p}} \cdot \mathbf{k} g_n(\lambda, k) \Big](\mathbf{p}) \tag{A.6}$$

and the dimensionless vector

$$F_m = \left(\frac{\beta}{m}\right)^{3/2} \sum_{\lambda} \int \frac{d^2\mathbf{p}}{(2\pi)^2} \lambda p f^0_\lambda(p)[1 - f^0_\lambda(p)] g_m(\lambda, p). \tag{A.7}$$

(A.5) can be inverted to yield

$$\mathbf{a} = M^{-1}\mathbf{F}. \tag{A.8}$$

The charge current is

$$\begin{aligned} \mathbf{J} &= \frac{e}{m} N_f \sum_{\lambda} \int \frac{d^2\mathbf{p}}{(2\pi)^2} \lambda \mathbf{p} f_\lambda(\mathbf{p}) \\ &= \beta N_f \sum_{\lambda} \int \frac{d^2\mathbf{p}}{(2\pi)^2} \lambda \mathbf{p} f^0_\lambda(\mathbf{p})[1 - f^0_\lambda(\mathbf{p})] \frac{e^2\mathbf{E}}{m^2} \cdot \mathbf{p} \chi_\lambda(p). \end{aligned} \tag{A.9}$$

The DC conductivity is read off as

$$\sigma_{xx} = \beta N_f \sum_{\lambda} \int \frac{d^2\mathbf{p}}{(2\pi)^2} \lambda f^0_\lambda(p)[1 - f^0_\lambda(p)] \frac{e^2 p_x^2}{m^2} \chi_\lambda(p) = \frac{N_f e^2}{2\hbar} \mathbf{G} \cdot M^{-1}\mathbf{F}, \tag{A.10}$$

where we have exceptionally restored $\hbar$ and where the dimensionless vector

$$G_m = \left(\frac{\beta}{m}\right)^{2} \sum_{\lambda} \int \frac{d^2\mathbf{p}}{(2\pi)^2} \lambda p^2 f^0_\lambda(p)[1 - f^0_\lambda(p)] g_m(\lambda, p) \tag{A.11}$$

Appendix B

Two-fluid model details

We defined the electron and hole velocities as

$$\mathbf{u}^e = \frac{\int \frac{d^2\mathbf{p}}{(2\pi)^2} \frac{\mathbf{p}}{m} f_+(\mathbf{p})}{\int \frac{d^2\mathbf{p}}{(2\pi)^2} f_+^0(\mathbf{p})}, \qquad \mathbf{u}^h = -\frac{\int \frac{d^2\mathbf{p}}{(2\pi)^2} \frac{\mathbf{p}}{m} (1 - f_-(\mathbf{p}))}{\int \frac{d^2\mathbf{p}}{(2\pi)^2} (1 - f_-^0(\mathbf{p}))}. \tag{B.1}$$

The coefficients $\Lambda^{e,h}$ account for the fact that the average entropy per particle is Λk_B

$$k_B T \Lambda^e = \frac{\int \frac{d^2\mathbf{p}}{(2\pi)^2} p^2 (\epsilon_+(p) - \mu) f_+^0(\mathbf{p})[1 - f_+^0(\mathbf{p})]}{\int \frac{d^2\mathbf{p}}{(2\pi)^2} f_+^0(\mathbf{p})} \tag{B.2}$$

$$k_B T \Lambda^h = \frac{\int \frac{d^2\mathbf{p}}{(2\pi)^2} p^2 (-\epsilon_-(p) + \mu) f_-^0(\mathbf{p})[1 - f_-^0(\mathbf{p})]}{\int \frac{d^2\mathbf{p}}{(2\pi)^2} (1 - f_-^0(\mathbf{p}))}. \tag{B.3}$$

One can derive explicitly equations (B.2) and (B.3) from the ∇T term in Boltzmann's equation (2.73). It is easy to show that these integrals are in fact the entropy per particle

$$\Lambda^e = -\frac{\int \frac{d^2\mathbf{p}}{(2\pi)^2} \left[\left(1 - f_+^0(\mathbf{p})\right) \ln \left(1 - f_+^0(\mathbf{p})\right) + f_+^0(\mathbf{p}) \ln f_+^0(\mathbf{p}) \right]}{\int \frac{d^2\mathbf{p}}{(2\pi)^2} f_+^0(\mathbf{p})}, \tag{B.4}$$

$$\Lambda^h = -\frac{\int \frac{d^2\mathbf{p}}{(2\pi)^2} \left[\left(1 - f_-^0(\mathbf{p})\right) \ln \left(1 - f_-^0(\mathbf{p})\right) + f_-^0(\mathbf{p}) \ln f_-^0(\mathbf{p}) \right]}{\int \frac{d^2\mathbf{p}}{(2\pi)^2} [1 - f_-^0(\mathbf{p})]}, \tag{B.5}$$

which were used previously in [105]. The Coulomb drag term can be derived explicitly from the collision integral

$$\int \frac{d^2\mathbf{p}}{(2\pi)^2}\frac{\lambda\mathbf{p}}{m} I^{(1)}_{\lambda,\text{e-e}}\left[h_{\lambda_i}(\mathbf{k}_i) = \lambda_i\beta\mathbf{k}_i\cdot\left(\frac{\mathbf{u}^e-\mathbf{u}^h}{2}\right)\right](\mathbf{p}) = \begin{cases} -\frac{mn^e}{\tau_{\text{e-h}}}(\mathbf{u}^e-\mathbf{u}^{\mathbf{h}}) & \lambda = + \\ \frac{mn^h}{\tau_{\text{h-e}}}(\mathbf{u}^e-\mathbf{u}^{\mathbf{h}}) & \lambda = -. \end{cases} \tag{B.6}$$

This allows us to calculate $\tau_{\text{e-h}}$ and $\tau_{\text{h-e}}$. We perform the calculation at charge neutrality and then use (2.65) to extrapolate.

Appendix C

Mapping to the spin-boson model

C.1 Mapping to the spin-boson model

We start with the full Hamiltonian (3.9)

$$\hat{H}(t) = \hat{H}_0(t) + \hat{H}_{\text{tun}}(t) + \hat{H}_{\text{int}}. \tag{C.1}$$

Writing out all terms from the main text in full,

$$\hat{H}(t) = \varepsilon(t)\hat{S}_z + \frac{v}{2}\int \frac{dx}{2\pi}\,(\partial_x\hat{\varphi})^2 + \lambda(t)\Big(\hat{\psi}^\dagger(0)\hat{S}^- + h.c.\Big) - \gamma\frac{g}{2\pi}\partial_x\hat{\varphi}(0)\hat{S}_z. \tag{C.2}$$

The bosonic field is given in the eigenmode expansion with momenta $k = 2\pi m/L$, $m \in \mathbb{Z}$ as

$$\hat{\varphi}(x) = -\sum_{k>0}\sqrt{\frac{2\pi}{kL}}(\hat{b}_k e^{ikx} + \hat{b}_k^\dagger e^{-ikx})e^{-ka/2}. \tag{C.3}$$

In the bosonization formalism, the fermion operator is a vertex operator of the form

$$\hat{\psi}(x) = \frac{1}{\sqrt{2\pi a\gamma}}e^{-i\gamma\hat{\varphi}(x)}. \tag{C.4}$$

We apply the unitary transformation

$$\hat{U}_1 = \exp\Big[-i\gamma\hat{\varphi}(0)\hat{S}_z\Big] \tag{C.5}$$

to obtain the transformed Hamiltonian

$$\hat{H}_1 = \hat{U_1}^\dagger \hat{H} \hat{U_1}. \tag{C.6}$$

We use the identity from [7] for operators A, B valid if $[A, C] = [B, C] = 0$ where $C = [A, B]$

$$e^{-B} A e^{B} = A + C. \tag{C.7}$$

Since $[\hat{S}_z, \hat{U_1}] = 0$, the first term in (C.2) is clearly unchanged by the unitary transformation:

$$\hat{U_1}^\dagger \varepsilon(t) \hat{S}_z \hat{U_1} = \varepsilon(t) \hat{S}_z. \tag{C.8}$$

Now using (C.7)

$$\begin{aligned} \hat{U_1}^\dagger (\partial_x \hat{\varphi}(x))^2 \hat{U_1} &= e^{i\gamma\hat{\varphi}(0)\hat{S}_z} (\partial_x \hat{\varphi}(x))^2 e^{-i\gamma\hat{\varphi}(0)\hat{S}_z} \\ &= (\partial_x \hat{\varphi}(x))^2 + [(\partial_x \hat{\varphi}(x))^2, -i\gamma\hat{\varphi}(0)\hat{S}_z] \\ &= (\partial_x \hat{\varphi}(x))^2 - 2i\gamma \hat{S}_z \partial_x \hat{\varphi}(x) [\partial_x \hat{\varphi}(x), \hat{\varphi}(0)] \\ &= (\partial_x \hat{\varphi}(x))^2 - 4\pi\gamma \hat{S}_z \partial_x \hat{\varphi}(0) \delta(x) \end{aligned} \tag{C.9}$$

using $[\partial_x \hat{\varphi}(x), \hat{\varphi}(0)] = -2\pi i \delta(x)$. So

$$\hat{U_1}^\dagger \left(\frac{v}{2} \int \frac{dx}{2\pi} \, (\partial_x \hat{\varphi})^2 \right) \hat{U_1} = \frac{v}{2} \int \frac{dx}{2\pi} \, (\partial_x \hat{\varphi})^2 - 4\pi\gamma v \hat{S}_z \partial_x \hat{\varphi}(0). \tag{C.10}$$

Next, consider the first part of the tunnelling term

$$\hat{U_1}^\dagger \hat{\psi}^\dagger(0) \hat{S}^- \hat{U_1} = e^{i\gamma\hat{\varphi}(0)\hat{S}_z} \frac{1}{\sqrt{2\pi a \gamma}} e^{i\gamma\hat{\varphi}(0)} \hat{S}^- e^{-i\gamma\hat{\varphi}(0)\hat{S}_z}. \tag{C.11}$$

Since the states $|\uparrow\rangle$ and $|\downarrow\rangle$ where $\hat{S}_z |\uparrow,\downarrow\rangle = \pm\frac{1}{2} |\uparrow,\downarrow\rangle$ form a basis, it is sufficient to evaluate the equation when acting on the eigenstates of $\hat{S}_z$. Since $\hat{S}^-$ annihilates $|\downarrow\rangle$, we only need to consider the effect on $|\uparrow\rangle$.

$$e^{i\gamma\hat{\varphi}(0)\hat{S}_z} e^{i\gamma\hat{\varphi}(0)} \hat{S}^- e^{-i\gamma\hat{\varphi}(0)\hat{S}_z} |\uparrow\rangle = e^{-i\gamma\hat{\varphi}(0)/2} e^{i\gamma\hat{\varphi}(0)} e^{-i\gamma\hat{\varphi}(0)/2} \hat{S}^- |\uparrow\rangle = \hat{S}^- |\uparrow\rangle \tag{C.12}$$

Therefore

$$\hat{U_1}^\dagger \hat{\psi}^\dagger(0)\hat{S}^- \hat{U_1} = \frac{1}{\sqrt{2\pi a\gamma^2}}\hat{S}^- \tag{C.13}$$

and similarly

$$\hat{U_1}^\dagger \hat{\psi}^\dagger(0)\hat{S}^+ \hat{U_1} = \frac{1}{\sqrt{2\pi a\gamma^2}}\hat{S}^+. \tag{C.14}$$

so the full tunnelling term transforms as

$$\hat{U_1}^\dagger \lambda(t)\left(\hat{\psi}^\dagger(0)\hat{S}^+ + \text{h.c.}\right)\hat{U_1} = 2\lambda(t)\frac{1}{\sqrt{2\pi a\gamma^2}}\hat{S}_x. \tag{C.15}$$

The last term in (C.2) commutes with $\hat{U}_1$ and is hence unchanged by the transformation

$$\hat{U_1}^\dagger \gamma\frac{g}{2\pi}\partial_x\hat{\varphi}(0)\hat{S}_z\hat{U_1} = \gamma\frac{g}{2\pi}\partial_x\hat{\varphi}(0)\hat{S}_z. \tag{C.16}$$

Putting all the pieces (C.8),(C.10),(C.15) and (C.16) together, the transformed Hamiltonian is

$$\hat{H}_1 = \varepsilon(t)\hat{S}_z + \frac{v}{2}\int\frac{dx}{2\pi}(\partial_x\hat{\varphi})^2 + \lambda(t)\sqrt{\frac{2}{\pi a\gamma^2}}\hat{S}_x + v\tilde{\gamma}\hat{S}_z\partial_x\hat{\varphi}(0), \tag{C.17}$$

where

$$\tilde{\gamma} = \gamma\left(1 - \frac{g}{2\pi v}\right). \tag{C.18}$$

To make the connection with the spin-boson model, define

$$\Delta(t) = \lambda(t)\sqrt{\frac{2}{\pi a\gamma^2}}, \quad \eta_k = v\tilde{\gamma}\sqrt{\frac{2\pi k}{L}}e^{-ka/2} \tag{C.19}$$

and use the expansion of the bosonic field in terms of ladder operators (C.3) to obtain

$$\hat{H}_1 = \varepsilon(t)\hat{S}_z + \Delta(t)\hat{S}_x + \sum_{k>0}\omega_k\hat{b}_k^\dagger\hat{b}_k - i\hat{S}_z\sum_{k>0}\eta_k(\hat{b}_k - \hat{b}_k^\dagger), \tag{C.20}$$

this is precisely the spin-boson model.

C.2 Current calculation

C.2.1 Derivation from transformed Hamiltonian

We can now refermionize (C.17). To this end we introduce the new vertex operator with renormalized exponent $\tilde{\gamma}$

$$\hat{\tilde{\psi}}(x) = \frac{1}{\sqrt{2\pi a\tilde{\gamma}^2}} e^{-i\tilde{\gamma}\hat{\varphi}(x)}. \tag{C.21}$$

and the unitary transformation

$$\hat{U}_2 = \exp\left[i\tilde{\gamma}\hat{\varphi}(0)\hat{S}_z\right] \tag{C.22}$$

We perform another unitary transformation

$$\hat{H}_2 = \hat{U_2}^{\dagger}\hat{H}_1\hat{U}_2. \tag{C.23}$$

Just as $\hat{U}_1$ created an additional term that renormalized the Coulomb interactions, $\hat{U}_2$ will absorb the entire last term and yield

$$\hat{H}_2 = \varepsilon(t)\hat{S}_z + \frac{v}{2}\int \frac{dx}{2\pi}\,(\partial_x\hat{\varphi})^2 + \tilde{\lambda}(t)\left(\hat{\tilde{\psi}}^{\dagger}(0)\hat{S}^{-} + h.c.\right) \tag{C.24}$$

where

$$\tilde{\lambda}(t) = \frac{\tilde{\gamma}}{\gamma}\lambda(t). \tag{C.25}$$

Thus we have entirely eliminated the Coulomb interaction term, by renormalizing the charge of the tunnelling particle from q to $\tilde{q}$ and renormalizing the tunnelling amplitude.

In order to calculate the current, we need to calculate the equations of motion of the Hamiltonian. The operator $\hat{N}$ transforms trivially

$$\hat{N}_2 = \hat{U}_2^{\dagger}\hat{U}_1^{\dagger}\hat{N}\hat{U}_1\hat{U}_2 = \hat{N}. \tag{C.26}$$

Therefore, the Heisenberg equation of motion for $\hat{N}$ is

$$\frac{d\hat{N}}{dt} = \frac{d\hat{N}_2}{dt} = i[\hat{H}_2, \hat{N}_2] = i[\hat{H}_2, \hat{S}_z] = i\tilde{\lambda}(t)\left(\hat{\tilde{\psi}}^{\dagger}(0)\hat{S}^{-} - h.c.\right). \tag{C.27}$$

The operator $\hat{\varphi}(x)$ transforms as

$$\hat{\varphi}_2(x) = \hat{U}_2^\dagger \hat{U}_1^\dagger \hat{\varphi}(x) \hat{U}_1 \hat{U}_2 = \hat{\varphi}(x) + \pi(\gamma - \tilde{\gamma})\text{sgn}(x)\hat{S}_z. \tag{C.28}$$

The Heisenberg equation of motion for $\hat{\varphi}_2(x)$ is

$$\partial_t \hat{\varphi}_2(x) = i[\hat{H}_2, \hat{\varphi}_2(x)] = i[\hat{H}_2, \hat{\varphi}(x) + \pi(\gamma - \tilde{\gamma})\text{sgn}(x)\hat{S}_z] = i[\hat{H}_2, \hat{\varphi}(x)] + \pi(\gamma - \tilde{\gamma})\text{sgn}(x)\frac{d\hat{N}}{dt} \tag{C.29}$$

$$\partial_t(\hat{\varphi}(x) + \pi(\gamma - \tilde{\gamma})\text{sgn}(x)\hat{S}_z) = i[\hat{H}_2, \hat{\varphi}(x)] + \pi(\gamma - \tilde{\gamma})\text{sgn}(x)\frac{d\hat{N}}{dt}. \tag{C.30}$$

Cancelling terms on both sides

$$\partial_t \hat{\varphi}(x) = i[\hat{H}_2, \hat{\varphi}(x)] = -v\partial_x \hat{\varphi}(x) + i\pi\tilde{\gamma}\text{sgn}(x)\tilde{\lambda}(t)\left(\hat{\tilde{\psi}}^\dagger(0)\hat{S}^- - h.c.\right) = -v\partial_x \hat{\varphi}(x) + \pi\tilde{\gamma}\text{sgn}(x)\frac{d\hat{N}}{dt} \tag{C.31}$$

$$(\partial_t + v\partial_x)\hat{\varphi}(x) = +\pi\tilde{\gamma}\text{sgn}(x)\frac{d\hat{N}}{dt}. \tag{C.32}$$

The solution to the differential equation (C.32) imposing that $\hat{\varphi}(x)$ is continuous at $x = 0$[1] is

$$\hat{\varphi}(x,t) = \begin{cases} \pi\tilde{\gamma}(\hat{N}(t) - 2\hat{N}(t - x/v)) + \hat{f}(t - x/v) & x > 0 \\ -\pi\tilde{\gamma}\hat{N}(t - x/v) + \hat{f}(t - x/v) & x < 0 \end{cases} \tag{C.33}$$

where $\hat{f}(t - x/v)$ is an arbitrary function. This yields

$$\frac{v}{2\pi}(\partial_x \hat{\varphi}(+0) - \partial_x \hat{\varphi}(-0)) = \tilde{\gamma}\frac{d\hat{N}}{dt}. \tag{C.34}$$

Now the charge density is $\hat{\rho}(x) = +e\sqrt{\nu}\partial_x\hat{\varphi}/2\pi$ and since the excitations move with velocity v, the current is $\hat{I} = v\hat{\rho}$. Thus (C.34) becomes

$$\hat{I}(+0) - \hat{I}(-0) = -\tilde{q}\frac{d\hat{N}}{dt}, \tag{C.35}$$

so there is a jump in the current at $x = 0$ due to the charge leaking off the dot, however note the prefactor is $\tilde{q}$ not q. We now set the boundary condition that there is no incoming

[1] The continuity on $\hat{\varphi}(x)$ comes from its derivatives being finite in (C.32).

current on the left of the QPC, then $\partial_x \hat{\varphi}(x<0) = 0$. This requires

$$\hat{f}(t - x/v) = \pi\tilde{\gamma}\hat{N}(t - x/v) \tag{C.36}$$

and hence

$$\hat{\varphi}(x,t) = \begin{cases} \pi\tilde{\gamma}(\hat{N}(t) - \hat{N}(t - x/v)) & x > 0 \\ 0 & x < 0 \end{cases} \tag{C.37}$$

This yields the result quoted in the main text

$$\hat{I}(x,t) = -\tilde{q}\frac{d\hat{N}(t - x/v)}{dt}. \tag{C.38}$$

where $\tilde{q} = -\tilde{\gamma}\sqrt{\nu}e$.

Appendix D

Bilayer quantum Hall details

D.1 Monte-Carlo procedure

We follow the approach outlined in Ref. [259]. For the calculation of the overlaps we use the probability distribution of the 111 state as a sampling distribution for the Monte-Carlo (MC) algorithm. This choice guarantees that we are sampling from the part of the Hilbert space in which the ground state lies for small d/ℓ_B. For large d/ℓ_B, we find that the MC errors lie within an acceptable range, even for this choice of sampling.

For the overlaps of the ED ground state with the 111 state, the CFL and the p-wave BCS state, we work in terms of electron coordinates in both layers. We start with a random distribution of the electron coordinates $(\{\Omega^{\uparrow}\}, \{\Omega^{\downarrow}\})$ and perform a random walk on the sphere according to [259]. At each MC step, we propose a move of one particle to a new position and accept or reject the move based on the Metropolis algorithm for the probability distribution

$$\rho(\{\Omega^{\uparrow}\}, \{\Omega^{\downarrow}\}) = |\Psi_{111}(\{\Omega^{\uparrow}\}, \{\Omega^{\downarrow}\})|^2. \tag{D.1}$$

After a suitable equilibration period, the electron coordinates will be distributed according to the probability distribution $\rho(\{\Omega^{\uparrow}\}, \{\Omega^{\downarrow}\})$ and we can generate MC samples $(\{\Omega^{\uparrow}\}_I, \{\Omega^{\downarrow}\}_I)$ where $I = 0, \ldots, N_{\mathrm{MC}} - 1$. The number of MC samples N_{MC} was chosen up to 10^8 depending on system size. Then, for example, the overlap of the ED ground

state with the CFL will be

$$\langle \Psi_{\rm GS} | \Psi_{\rm CFL} \rangle = \int \mathrm{d}\Omega_1^\uparrow \ldots \mathrm{d}\Omega_{N_\uparrow}^\uparrow \, \mathrm{d}\Omega_1^\downarrow \ldots \mathrm{d}\Omega_{N_\downarrow}^\downarrow \Psi_{\rm GS}^*(\{\Omega^\uparrow\},\{\Omega^\downarrow\}) \Psi_{\rm CFL}(\{\Omega^\uparrow\},\{\Omega^\downarrow\}) \tag{D.2}$$

$$= \frac{1}{N_{\rm MC}} \sum_{I=0}^{N_{\rm MC}-1} \frac{\Psi_{\rm GS}^*(\{\Omega^\uparrow\}_I,\{\Omega^\downarrow\}_I)\Psi_{\rm CFL}(\{\Omega^\uparrow\}_I,\{\Omega^\downarrow\}_I)}{\rho(\{\Omega^\uparrow\}_I,\{\Omega^\downarrow\}_I)} j(\{\Omega^\uparrow\}_I,\{\Omega^\downarrow\}_I) \tag{D.3}$$

where

$$j(\{\Omega^\uparrow\},\{\Omega^\downarrow\}) = \prod_{n=1}^{N_\uparrow} \sin\theta_n^\uparrow \prod_{n=1}^{N_\downarrow} \sin\theta_n^\downarrow \tag{D.4}$$

is the Jacobian for the area element on the sphere. We proceed similarly for the overlap with the s-wave trial state, except that we work in terms of electron coordinates in the top layer and hole coordinates in the bottom layer, i.e. $(\{\Omega^\uparrow\},\{\varpi^\downarrow\})$ and use the probability distribution

$$\rho(\{\Omega^\uparrow\},\{\varpi^\downarrow\}) = |\Psi_{111}(\{\Omega^\uparrow\},\{\varpi^\downarrow\})|^2. \tag{D.5}$$

D.2 Finding $D(L=0)$

First consider one individual layer, such that the single particle states have $m = -q, \ldots, q$. Now work out the $\binom{2q+1}{(2q+1)/2}$ many-body states $(m_1, \ldots, m_N)$. For each of these states, compute $M = \sum_i m_i$. By looking at the highest M state, we deduce there must be a multiplet with $J = M$. We then take away the $2J+1$ states in that multiplet and iterate. Once we know all the possible values of J for an individual layer, we can add the momenta in the two layers. We know that $J_\uparrow$ and $J_\downarrow$ must be the same. Then

$$D(L=0) = \sum_{J_\uparrow} N_{J_\uparrow}^2 \tag{D.6}$$

where $N_{J_\uparrow}$ is the number of times that the $J_\uparrow$ multiplet appears in the single-layer many-body states. Using the Clebsch-Gordan coefficient

$$\langle j_1 m_1; j_2 m_2 | 00 \rangle = \delta_{j_1,j_2}\delta_{m_1,-m_2} \frac{(-1)^{j_1-m_1}}{\sqrt{2j_1+1}} \tag{D.7}$$

we deduce that

$$\langle J_\uparrow M_\uparrow; J_\uparrow - M_\uparrow | 00 \rangle = (-1)^{2M_\uparrow} \langle J_\uparrow - M_\uparrow; J_\uparrow M_\uparrow | 00 \rangle \tag{D.8}$$

and since $(-1)^{2M_\uparrow} = (-1)^{2J_\uparrow}$, the states have even parity under layer exchange if $J_\uparrow$ is an integer (and hence when there are an even number of particles per layer) and odd parity if $J_\uparrow$ is a half-integer (and hence there are an odd number of particles per layer). However, we need to remember that if $N_{J_\uparrow} > 1$, then we can form both symmetric and antisymmetric combinations. In particular if we have states $\{|J_\uparrow\rangle_1, \ldots, |J_\uparrow\rangle_{N_{J_\uparrow}}\}$, then there will be $N_{J_\uparrow}$ diagonal pairings which have symmetry $(-1)^{N_1}$ and $N_{J_\uparrow}(N_{J_\uparrow} - 1)/2$ off-diagonal pairings that have symmetry $(-1)^{N_1}$ as well as $N_{J_\uparrow}(N_{J_\uparrow} - 1)/2$ off-diagonal pairings that have symmetry $-(-1)^{N_1}$.

Bibliography

[1] Peter J. Mohr, David B. Newell, and Barry N. Taylor. Codata recommended values of the fundamental physical constants: 2014. *Rev. Mod. Phys.*, 88:035009, Sep 2016. URL: https://link.aps.org/doi/10.1103/RevModPhys.88.035009, doi:10.1103/RevModPhys.88.035009.

[2] Glenn Wagner, Fernando de Juan, and Dung X. Nguyen. Quantum Hall effect in curved space realized in strained graphene. *arXiv e-prints*, page arXiv:1911.02028, November 2019. arXiv:1911.02028.

[3] Yves H. Kwan, Glenn Wagner, Nilotpal Chakraborty, Steven H. Simon, and S. A. Parameswaran. Domain wall competition in the Chern insulating regime of twisted bilayer graphene. *arXiv e-prints*, page arXiv:2007.07903, July 2020. arXiv:2007.07903.

[4] Glenn Wagner, Henrik S. Røising, Felix Flicker, and Steven H. Simon. A microscopic Ginzburg–Landau theory and singlet ordering in Sr_2RuO_4. *arXiv e-prints*, page arXiv:2012.09866, December 2020. arXiv:2012.09866.

[5] Ernst Ising. Beitrag zur theorie des ferromagnetismus. *Zeitschrift für Physik*, 31(1):253–258, 1925.

[6] Lars Onsager. Crystal statistics. i. a two-dimensional model with an order-disorder transition. *Phys. Rev.*, 65:117–149, Feb 1944. URL: https://link.aps.org/doi/10.1103/PhysRev.65.117, doi:10.1103/PhysRev.65.117.

[7] Jan von Delft and Herbert Schoeller. Bosonization for beginners — refermionization for experts. *Ann. Phys. (Berl.)*, 7(4):225–305, 1998. doi:10.1002/(SICI)1521-3889(199811)7:4<225::AID-ANDP225>3.0.CO;2-L.

[8] U. Schollwöck. The density-matrix renormalization group. *Rev. Mod. Phys.*, 77:259–315, Apr 2005. URL: https://link.aps.org/doi/10.1103/RevModPhys.77.259, doi:10.1103/RevModPhys.77.259.

[9] J M Kosterlitz and D J Thouless. Ordering, metastability and phase transitions in two-dimensional systems. *Journal of Physics C: Solid State Physics*, 6(7):1181–1203, apr 1973. URL: https://doi.org/10.1088/0022-3719/6/7/010, doi:10.1088/0022-3719/6/7/010.

[10] Klaus von Klitzing, Tapash Chakraborty, Philip Kim, Vidya Madhavan, Xi Dai, James McIver, Yoshinori Tokura, Lucile Savary, Daria Smirnova, Ana Maria Rey, Claudia Felser, Johannes Gooth, and Xiaoliang Qi. 40 years of the quantum hall effect. *Nature Reviews Physics*, 2(8):397–401, Aug 2020. URL: https://doi.org/10.1038/s42254-020-0209-1, doi:10.1038/s42254-020-0209-1.

[11] A. K. Geim and K. S. Novoselov. The rise of graphene. *Nature Materials*, 6(3):183–191, Mar 2007. URL: https://doi.org/10.1038/nmat1849, doi:10.1038/nmat1849.

[12] K. S. Novoselov, D. Jiang, F. Schedin, T. J. Booth, V. V. Khotkevich, S. V. Morozov, and A. K. Geim. Two-dimensional atomic crystals. *Proceedings of the National Academy of Sciences*, 102(30):10451–10453, 2005. URL: https://www.pnas.org/content/102/30/10451, arXiv:https://www.pnas.org/content/102/30/10451.full.pdf, doi:10.1073/pnas.0502848102.

[13] Youngwoo Nam, Dong-Keun Ki, David Soler-Delgado, and Alberto F. Morpurgo. Electron-hole collision limited transport in charge-neutral bilayer graphene. *Nature Physics*, 13:1207 EP –, Aug 2017. Article. URL: http://dx.doi.org/10.1038/nphys4218.

[14] Robert Herman and Ilya Prigogine. A two-fluid approach to town traffic. *Science*, 204(4389):148–151, 1979. URL: https://science.sciencemag.org/content/204/4389/148, arXiv:https://science.sciencemag.org/content/204/4389/148.full.pdf, doi:10.1126/science.204.4389.148.

[15] L. TISZA. Transport phenomena in helium ii. *Nature*, 141(3577):913–913, May 1938. URL: https://doi.org/10.1038/141913a0, doi:10.1038/141913a0.

[16] L. Landau. Theory of the superfluidity of helium ii. *Phys. Rev.*, 60:356–358, Aug 1941. URL: https://link.aps.org/doi/10.1103/PhysRev.60.356, doi:10.1103/PhysRev.60.356.

[17] A. V. Andreev, Steven A. Kivelson, and B. Spivak. Hydrodynamic description of transport in strongly correlated electron systems. *Phys. Rev. Lett.*, 106:256804, Jun 2011. URL: https://link.aps.org/doi/10.1103/PhysRevLett.106.256804, doi:10.1103/PhysRevLett.106.256804.

[18] Andrew Lucas. Hydrodynamic transport in strongly coupled disordered quantum field theories. *New Journal of Physics*, 17(11):113007, oct 2015. URL: https://doi.org/10.1088/1367-2630/17/11/113007, doi:10.1088/1367-2630/17/11/113007.

[19] Glenn Wagner, Dung X. Nguyen, and Steven H. Simon. Transport in bilayer graphene near charge neutrality: Which scattering mechanisms are important? *Phys. Rev. Lett.*, 124:026601, Jan 2020. URL: https://link.aps.org/doi/10.1103/PhysRevLett.124.026601, doi:10.1103/PhysRevLett.124.026601.

[20] Dung X. Nguyen, Glenn Wagner, and Steven H. Simon. Quantum boltzmann equation for bilayer graphene. *Phys. Rev. B*, 101:035117, Jan 2020. URL: https://link.aps.org/doi/10.1103/PhysRevB.101.035117, doi:10.1103/PhysRevB.101.035117.

[21] Glenn Wagner, Dung X. Nguyen, and Steven H. Simon. Transport properties of multilayer graphene. *Phys. Rev. B*, 101:245438, Jun 2020. URL: https://link.aps.org/doi/10.1103/PhysRevB.101.245438, doi:10.1103/PhysRevB.101.245438.

[22] Yuanbo Zhang, Yan-Wen Tan, Horst L. Stormer, and Philip Kim. Experimental observation of the quantum hall effect and berry's phase in graphene. *Nature*, 438(7065):201–204, Nov 2005. URL: https://doi.org/10.1038/nature04235, doi:10.1038/nature04235.

[23] Chetan Nayak, Steven H. Simon, Ady Stern, Michael Freedman, and Sankar Das Sarma. Non-abelian anyons and topological quantum computation. *Rev. Mod. Phys.*, 80:1083–1159, Sep 2008. URL: https://link.aps.org/doi/10.1103/RevModPhys.80.1083, doi:10.1103/RevModPhys.80.1083.

[24] R. B. Laughlin. Anomalous quantum hall effect: An incompressible quantum fluid with fractionally charged excitations. *Phys. Rev. Lett.*, 50:1395–1398, May 1983. URL: https://link.aps.org/doi/10.1103/PhysRevLett.50.1395, doi:10.1103/PhysRevLett.50.1395.

[25] Glenn Wagner, Dung X. Nguyen, Dmitry L. Kovrizhin, and Steven H. Simon. Interaction effects and charge quantization in single-particle quantum dot emitters. *Phys. Rev. Lett.*, 122:127701, Mar 2019. URL: https://link.aps.org/doi/10.1103/PhysRevLett.122.127701, doi:10.1103/PhysRevLett.122.127701.

[26] Glenn Wagner, Dung X. Nguyen, Dmitry L. Kovrizhin, and Steven H. Simon. Driven quantum dot coupled to a fractional quantum hall edge. *Phys. Rev. B*, 100:245111, Dec 2019. URL: https://link.aps.org/doi/10.1103/PhysRevB.100.245111, doi:10.1103/PhysRevB.100.245111.

[27] B. I. Halperin. Theory of the quantized Hall conductance. *Helv. Phys. Acta*, 56:75–102, 1983.

[28] Jinwu Ye. Fractional charges and quantum phase transitions in imbalanced bilayer quantum hall systems. *Phys. Rev. Lett.*, 97:236803, Dec 2006. URL: https://link.aps.org/doi/10.1103/PhysRevLett.97.236803, doi:10.1103/PhysRevLett.97.236803.

[29] Jinwu Ye and Longhua Jiang. Quantum phase transitions in bilayer quantum hall systems at a total filling factor $\nu_T = 1$. *Phys. Rev. Lett.*, 98:236802, Jun 2007. URL: https://link.aps.org/doi/10.1103/PhysRevLett.98.236802, doi:10.1103/PhysRevLett.98.236802.

[30] Longhua Jiang. *Quantum phase transition in strongly correlated systems.* PhD thesis, The Pennsylvania State University, 2008.

[31] Steven H. Simon, E. H. Rezayi, and Milica V. Milovanovic. Coexistence of composite bosons and composite fermions in $\nu = \frac{1}{2} + \frac{1}{2}$ quantum hall bilayers. *Phys. Rev. Lett.*, 91:046803, Jul 2003. URL: https://link.aps.org/doi/10.1103/PhysRevLett.91.046803, doi:10.1103/PhysRevLett.91.046803.

[32] R. L. Doretto, C. Morais Smith, and A. O. Caldeira. Finite-momentum condensate of magnetic excitons in a bilayer quantum hall system. *Phys. Rev. B*, 86:035326, Jul 2012. URL: https://link.aps.org/doi/10.1103/PhysRevB.86.035326, doi:10.1103/PhysRevB.86.035326.

[33] Ya-Hui Zhang and Itamar Kimchi. Paired exciton condensate and topological charge-4e composite fermion pairing in half-filled quantum Hall bilayers. *arXiv e-prints*, page arXiv:1810.02809, Oct 2018. arXiv:1810.02809.

[34] Biao Lian and Shou-Cheng Zhang. Wave function and emergent su(2) symmetry in the $\nu_T = 1$ quantum hall bilayer. *Phys. Rev. Lett.*, 120:077601, Feb 2018. URL: https://link.aps.org/doi/10.1103/PhysRevLett.120.077601, doi:10.1103/PhysRevLett.120.077601.

[35] M. V. Milovanović, E. Dobardžić, and Z. Papić. Meron deconfinement in the quantum hall bilayer at intermediate distances. *Phys. Rev. B*, 92:195311, Nov 2015. URL: https://link.aps.org/doi/10.1103/PhysRevB.92.195311, doi:10.1103/PhysRevB.92.195311.

[36] Jason Alicea, Olexei I. Motrunich, G. Refael, and Matthew P. A. Fisher. Interlayer coherent composite fermi liquid phase in quantum hall bilayers. *Phys. Rev. Lett.*, 103:256403, Dec 2009. URL: https://link.aps.org/doi/10.1103/PhysRevLett.103.256403, doi:10.1103/PhysRevLett.103.256403.

[37] Robert Cipri. *Gauge Fields and Composite Fermions in Bilayer Quantum Hall Systems*. PhD thesis, Florida State University, 2014.

[38] Gunnar Möller, Steven H. Simon, and Edward H. Rezayi. Trial wave functions for $\nu = \frac{1}{2} + \frac{1}{2}$ quantum hall bilayers. *Phys. Rev. B*, 79:125106, Mar 2009. URL: https://link.aps.org/doi/10.1103/PhysRevB.79.125106, doi:10.1103/PhysRevB.79.125106.

[39] Gunnar Möller, Steven H. Simon, and Edward H. Rezayi. Paired composite fermion phase of quantum hall bilayers at $\nu = \frac{1}{2} + \frac{1}{2}$. *Phys. Rev. Lett.*, 101:176803, Oct 2008. URL: https://link.aps.org/doi/10.1103/PhysRevLett.101.176803, doi:10.1103/PhysRevLett.101.176803.

[40] P. Drude. Zur elektronentheorie der metalle. *Annalen der Physik*, 306(3):566–613, 1900. URL: https://onlinelibrary.wiley.com/doi/abs/10.1002/andp.19003060312, arXiv:https://onlinelibrary.wiley.com/doi/pdf/10.1002/andp.19003060312, doi:https://doi.org/10.1002/andp.19003060312.

[41] Neil W Ashcroft, N David Mermin, et al. *Solid state physics*, volume 2005. holt, rinehart and winston, new york London, 1976.

[42] R. N. Gurzhi. Minimum of resistance in impurity-free conductors. *Journal of Experimental and Theoretical Physics*, 17(2):521, 1962. URL: http://www.jetp.ac.ru/cgi-bin/e/index/e/17/2/p521?a=list, doi:10.1063/1.4942216.

[43] Martin Knudsen. Die gesetze der molekularströmung und der inneren reibungsströmung der gase durch röhren. *Annalen der Physik*, 333(1):75–130, 1909. URL: https://onlinelibrary.wiley.com/doi/abs/10.1002/andp.19093330106, arXiv:https://onlinelibrary.wiley.com/doi/pdf/10.1002/andp.19093330106, doi:https://doi.org/10.1002/andp.19093330106.

[44] L. W. Molenkamp and M. J. M. de Jong. Electron-electron-scattering-induced size effects in a two-dimensional wire. *Phys. Rev. B*, 49:5038–5041, Feb 1994. URL: https://link.aps.org/doi/10.1103/PhysRevB.49.5038, doi:10.1103/PhysRevB.49.5038.

[45] M. J. M. de Jong and L. W. Molenkamp. Hydrodynamic electron flow in high-mobility wires. *Phys. Rev. B*, 51:13389–13402, May 1995. URL: https://link.aps.org/doi/10.1103/PhysRevB.51.13389, doi:10.1103/PhysRevB.51.13389.

[46] L.W. Molenkamp and M.J.M. de Jong. Observation of knudsen and gurzhi transport regimes in a two-dimensional wire. *Solid-State Electronics*, 37(4):551 – 553, 1994. URL: http://www.sciencedirect.com/science/article/pii/0038110194902445, doi:https://doi.org/10.1016/0038-1101(94)90244-5.

[47] Michael Dyakonov and Michael Shur. Shallow water analogy for a ballistic field effect transistor: New mechanism of plasma wave generation by dc current. *Phys. Rev. Lett.*, 71:2465–2468, Oct 1993. URL: https://link.aps.org/doi/10.1103/PhysRevLett.71.2465, doi:10.1103/PhysRevLett.71.2465.

[48] Edmond Chow, H. P. Wei, S. M. Girvin, and M. Shayegan. Phonon emission from a 2d electron gas: Evidence of transition to the hydrodynamic regime. *Phys. Rev. Lett.*, 77:1143–1146, Aug 1996. URL: https://link.aps.org/doi/10.1103/PhysRevLett.77.1143, doi:10.1103/PhysRevLett.77.1143.

[49] Daniel Gall. Electron mean free path in elemental metals. *Journal of Applied Physics*, 119(8):085101, 2016. URL: https://doi.org/10.1063/1.4942216, arXiv:https://doi.org/10.1063/1.4942216, doi:10.1063/1.4942216.

[50] Luca Banszerus, Michael Schmitz, Stephan Engels, Matthias Goldsche, Kenji Watanabe, Takashi Taniguchi, Bernd Beschoten, and Christoph Stampfer. Ballistic transport exceeding 28 μm in cvd grown graphene. *Nano Letters*, 16(2):1387–1391, Feb 2016. URL: https://doi.org/10.1021/acs.nanolett.5b04840, doi:10.1021/acs.nanolett.5b04840.

[51] K. S. Novoselov, A. Mishchenko, A. Carvalho, and A. H. Castro Neto. 2d materials and van der waals heterostructures. *Science*, 353(6298), 2016. URL: https://science.sciencemag.org/content/353/6298/aac9439, doi:10.1126/science.aac9439.

[52] Leonid Levitov and Gregory Falkovich. Electron viscosity, current vortices and negative nonlocal resistance in graphene. *Nature Physics*, 12:672, Feb 2016. URL: https://doi.org/10.1038/nphys3667.

[53] D. A. Bandurin, I. Torre, R. Krishna Kumar, M. Ben Shalom, A. Tomadin, A. Principi, G. H. Auton, E. Khestanova, K. S. Novoselov, I. V. Grigorieva, L. A. Ponomarenko, A. K. Geim, and M. Polini. Negative local resistance caused by viscous electron backflow in graphene. *Science*, 351(6277):1055–1058, 2016. URL: http://science.sciencemag.org/content/351/6277/1055, doi:10.1126/science.aad0201.

[54] Jesse Crossno, Jing K. Shi, Ke Wang, Xiaomeng Liu, Achim Harzheim, Andrew Lucas, Subir Sachdev, Philip Kim, Takashi Taniguchi, Kenji Watanabe, Thomas A. Ohki, and Kin Chung Fong. Observation of the dirac fluid and the breakdown of the wiedemann-franz law in graphene. *Science*, 351(6277):1058–1061, 2016. URL: https://science.sciencemag.org/content/351/6277/1058.

[55] Zhe Luo, Jifa Tian, Shouyuan Huang, Mithun Srinivasan, Jesse Maassen, Yong P. Chen, and Xianfan Xu. Large enhancement of thermal conductivity and lorenz number in topological insulator thin films. *ACS Nano*, 12(2):1120–1127, Feb 2018. URL: https://doi.org/10.1021/acsnano.7b06430, doi:10.1021/acsnano.7b06430.

[56] R. Krishna Kumar, D. A. Bandurin, F. M. D. Pellegrino, Y. Cao, A. Principi, H. Guo, G. H. Auton, M. Ben Shalom, L. A. Ponomarenko, G. Falkovich, K. Watanabe, T. Taniguchi, I. V. Grigorieva, L. S. Levitov, M. Polini, and A. K. Geim. Superballistic flow of viscous electron fluid through graphene constrictions. *Nature Physics*, 13(12):1182–1185, Dec 2017. URL: https://doi.org/10.1038/nphys4240, doi:10.1038/nphys4240.

[57] Haoyu Guo, Ekin Ilseven, Gregory Falkovich, and Leonid S. Levitov. Higher-than-ballistic conduction of viscous electron flows. *Proceedings of the National Academy of Sciences*, 114(12):3068–3073, 2017. URL: https://www.pnas.org/content/114/12/3068, arXiv:https://www.pnas.org/content/114/12/3068.full.pdf, doi:10.1073/pnas.1612181114.

[58] Joseph A. Sulpizio, Lior Ella, Asaf Rozen, John Birkbeck, David J. Perello, Debarghya Dutta, Moshe Ben-Shalom, Takashi Taniguchi, Kenji Watanabe, Tobias Holder, Raquel Queiroz, Alessandro Principi, Ady Stern, Thomas Scaffidi, Andre K. Geim, and Shahal Ilani. Visualizing poiseuille flow of hydrodynamic electrons. *Nature*, 576(7785):75–79, Dec 2019. URL: https://doi.org/10.1038/s41586-019-1788-9, doi:10.1038/s41586-019-1788-9.

[59] Mark J. H. Ku, Tony X. Zhou, Qing Li, Young J. Shin, Jing K. Shi, Claire Burch, Laurel E. Anderson, Andrew T. Pierce, Yonglong Xie, Assaf Hamo, Uri Vool, Huiliang Zhang, Francesco Casola, Takashi Taniguchi, Kenji Watanabe, Michael M. Fogler, Philip Kim, Amir Yacoby, and Ronald L. Walsworth. Imaging viscous flow of the dirac fluid in graphene. *Nature*, 583(7817):537–541, Jul 2020. URL: https://doi.org/10.1038/s41586-020-2507-2, doi:10.1038/s41586-020-2507-2.

[60] Nuno Peres. The transport properties of graphene: an introduction. rev. mod. phys. 82, 2673. *Reviews of Modern Physics*, 82, 07 2010. doi:10.1103/RevModPhys.82.2673.

[61] K.I. Bolotin, K.J. Sikes, Z. Jiang, M. Klima, G. Fudenberg, J. Hone, P. Kim, and H.L. Stormer. Ultrahigh electron mobility in suspended graphene. *Solid State Communications*, 146(9):351 – 355, 2008. URL: http://www.sciencedirect.com/science/article/pii/S0038109808001178, doi:https://doi.org/10.1016/j.ssc.2008.02.024.

[62] S. V. Morozov, K. S. Novoselov, M. I. Katsnelson, F. Schedin, D. C. Elias, J. A. Jaszczak, and A. K. Geim. Giant intrinsic carrier mobilities in graphene and its bilayer. *Phys. Rev. Lett.*, 100:016602, Jan 2008. URL: https://link.aps.org/doi/10.1103/PhysRevLett.100.016602, doi:10.1103/PhysRevLett.100.016602.

[63] Dong-Keun Ki, Vladimir I. Fal'ko, Dmitry A. Abanin, and Alberto F. Morpurgo. Observation of even denominator fractional quantum hall effect in suspended bilayer graphene. *Nano Letters*, 14(4):2135–2139, 2014. URL: https://doi.org/10.1021/nl5003922, doi:10.1021/nl5003922.

[64] R. T. Weitz, M. T. Allen, B. E. Feldman, J. Martin, and A. Yacoby. Broken-symmetry states in doubly gated suspended bilayer graphene. *Science*, 330(6005):812–816, 2010. URL: https://science.sciencemag.org/content/330/6005/812.

[65] Benjamin E. Feldman, Jens Martin, and Amir Yacoby. Broken-symmetry states and divergent resistance in suspended bilayer graphene. *Nature Physics*, 5:889, Sep 2009. URL: https://doi.org/10.1038/nphys1406.

[66] Michael Thompson Pettes, Insun Jo, Zhen Yao, and Li Shi. Influence of polymeric residue on the thermal conductivity of suspended bilayer graphene. *Nano Letters*, 11(3):1195–1200, 2011. URL: https://doi.org/10.1021/nl104156y, doi:10.1021/nl104156y.

[67] Dong-Keun Ki and Alberto F. Morpurgo. High-quality multiterminal suspended graphene devices. *Nano Letters*, 13(11):5165–5170, 2013. URL: https://doi.org/10.1021/nl402462q, doi:10.1021/nl402462q.

[68] F. Freitag, J. Trbovic, M. Weiss, and C. Schönenberger. Spontaneously gapped ground state in suspended bilayer graphene. *Phys. Rev. Lett.*, 108:076602, Feb 2012. URL: https://link.aps.org/doi/10.1103/PhysRevLett.108.076602, doi:10.1103/PhysRevLett.108.076602.

[69] J. Velasco Jr, L. Jing, W. Bao, Y. Lee, P. Kratz, V. Aji, M. Bockrath, C. N. Lau, C. Varma, R. Stillwell, D. Smirnov, Fan Zhang, J. Jung, and A. H. MacDonald. Transport spectroscopy of symmetry-broken insulating states in bilayer graphene. *Nature Nanotechnology*, 7:156, Jan 2012. URL: https://doi.org/10.1038/nnano.2011.251.

[70] Youngwoo Nam, Dong-Keun Ki, Mikito Koshino, Edward McCann, and Alberto F Morpurgo. Interaction-induced insulating state in thick multilayer graphene. *2D Materials*, 3(4):045014, oct 2016. URL: https://doi.org/10.1088%2F2053-1583%2F3%2F4%2F045014, doi:10.1088/2053-1583/3/4/045014.

[71] Lars Fritz, Jörg Schmalian, Markus Müller, and Subir Sachdev. Quantum critical transport in clean graphene. *Phys. Rev. B*, 78:085416, Aug 2008. URL: https://link.aps.org/doi/10.1103/PhysRevB.78.085416, doi:10.1103/PhysRevB.78.085416.

[72] Markus Müller, Lars Fritz, and Subir Sachdev. Quantum-critical relativistic magnetotransport in graphene. *Phys. Rev. B*, 78:115406, Sep 2008. URL: https://link.aps.org/doi/10.1103/PhysRevB.78.115406, doi:10.1103/PhysRevB.78.115406.

[73] Jonathan Lux and Lars Fritz. Kinetic theory of coulomb drag in two monolayers of graphene: From the dirac point to the fermi liquid regime. *Phys. Rev. B*, 86:165446, Oct 2012. URL: https://link.aps.org/doi/10.1103/PhysRevB.86.165446, doi:10.1103/PhysRevB.86.165446.

[74] Jonathan Lux and Lars Fritz. Interaction-dominated transport and coulomb drag in bilayer graphene. *Phys. Rev. B*, 87:075423, Feb 2013. URL: https://link.aps.org/doi/10.1103/PhysRevB.87.075423, doi:10.1103/PhysRevB.87.075423.

[75] Mohammad Zarenia, Giovanni Vignale, Thomas Benjamin Smith, and Alessandro Principi. Breakdown of the Wiedemann-Franz law in AB-stacked bilayer graphene. *arXiv e-prints*, Jan 2019. arXiv:1901.05077.

[76] Dung X. Nguyen, Glenn Wagner, and Steven H. Simon. Quantum Boltzmann equation for bilayer graphene. *arXiv e-prints*, January 2019. arXiv:1901.07039.

[77] E. Mostaani, N. D. Drummond, and V. I. Fal'ko. Quantum monte carlo calculation of the binding energy of bilayer graphene. *Phys. Rev. Lett.*, 115:115501, Sep 2015. URL: https://link.aps.org/doi/10.1103/PhysRevLett.115.115501, doi:10.1103/PhysRevLett.115.115501.

[78] Irina V. Lebedeva, Andrey A. Knizhnik, Andrey M. Popov, Yurii E. Lozovik, and Boris V. Potapkin. Interlayer interaction and relative vibrations of bilayer graphene. *Phys. Chem. Chem. Phys.*, 13:5687–5695, 2011. URL: http://dx.doi.org/10.1039/C0CP02614J, doi:10.1039/C0CP02614J.

[79] Edward McCann and Vladimir I. Fal'ko. Landau-level degeneracy and quantum hall effect in a graphite bilayer. *Phys. Rev. Lett.*, 96:086805, Mar 2006. URL: https://link.aps.org/doi/10.1103/PhysRevLett.96.086805, doi:10.1103/PhysRevLett.96.086805.

[80] T. Misumi and K. Shizuya. Electromagnetic response and pseudo-zero-mode landau levels of bilayer graphene in a magnetic field. *Physical Review B*, 77(19), may 2008. doi:10.1103/physrevb.77.195423.

[81] Edward McCann and Mikito Koshino. The electronic properties of bilayer graphene. *Reports on Progress in Physics*, 76(5):056503, 2013. URL: http://stacks.iop.org/0034-4885/76/i=5/a=056503.

[82] Youngwoo Nam, Dong-Keun Ki, David Soler-Delgado, and Alberto F. Morpurgo. A family of finite-temperature electronic phase transitions in graphene multilayers. *Science*, 362(6412):324–328, 2018. URL: http://science.sciencemag.org/content/362/6412/324, arXiv:http://science.sciencemag.org/content/362/6412/324.full.pdf, doi:10.1126/science.aar6855.

[83] Mikito Koshino and Tsuneya Ando. Transport in bilayer graphene: Calculations within a self-consistent born approximation. *Phys. Rev. B*, 73:245403, Jun 2006. URL: https://link.aps.org/doi/10.1103/PhysRevB.73.245403, doi:10.1103/PhysRevB.73.245403.

[84] Min Lv and Shaolong Wan. Screening-induced transport at finite temperature in bilayer graphene. *Phys. Rev. B*, 81:195409, May 2010. URL: https://link.aps.org/doi/10.1103/PhysRevB.81.195409, doi:10.1103/PhysRevB.81.195409.

[85] L.P. Kadanoff and G. Baym. *Quantum Statistical Mechanics*. W.A. Benjamin, New York, 1962.

[86] J. K. Viljas and T. T. Heikkilä. Electron-phonon heat transfer in monolayer and bilayer graphene. *Phys. Rev. B*, 81:245404, Jun 2010. URL: https://link.aps.org/doi/10.1103/PhysRevB.81.245404, doi:10.1103/PhysRevB.81.245404.

[87] Eros Mariani and Felix von Oppen. Temperature-dependent resistivity of suspended graphene. *Phys. Rev. B*, 82:195403, Nov 2010. URL: https://link.aps.org/doi/10.1103/PhysRevB.82.195403, doi:10.1103/PhysRevB.82.195403.

[88] H. Ochoa, Eduardo V. Castro, M. I. Katsnelson, and F. Guinea. Temperature-dependent resistivity in bilayer graphene due to flexural phonons. *Phys. Rev. B*, 83:235416, Jun 2011. URL: https://link.aps.org/doi/10.1103/PhysRevB.83.235416, doi:10.1103/PhysRevB.83.235416.

[89] Yangsu Xie, Zaoli Xu, Shen Xu, Zhe Cheng, Nastaran Hashemi, Cheng Deng, and Xinwei Wang. The defect level and ideal thermal conductivity of graphene uncovered by residual thermal reffusivity at the 0 k limit. *Nanoscale*, 7:10101–10110, 2015. URL: http://dx.doi.org/10.1039/C5NR02012C, doi:10.1039/C5NR02012C.

[90] J. K. Viljas and T. T. Heikkilä. Electron-phonon heat transfer in monolayer and bilayer graphene. *Phys. Rev. B*, 81:245404, Jun 2010. URL: https://link.aps.org/doi/10.1103/PhysRevB.81.245404, doi:10.1103/PhysRevB.81.245404.

[91] S. S. Kubakaddi. Interaction of massless dirac electrons with acoustic phonons in graphene at low temperatures. *Phys. Rev. B*, 79:075417, Feb 2009. URL: https://link.aps.org/doi/10.1103/PhysRevB.79.075417, doi:10.1103/PhysRevB.79.075417.

[92] R. Bistritzer and A. H. MacDonald. Electronic cooling in graphene. *Phys. Rev. Lett.*, 102:206410, May 2009. URL: https://link.aps.org/doi/10.1103/PhysRevLett.102.206410, doi:10.1103/PhysRevLett.102.206410.

[93] Hidekatsu Suzuura and Tsuneya Ando. Phonons and electron-phonon scattering in carbon nanotubes. *Phys. Rev. B*, 65:235412, May 2002. URL: https://link.aps.org/doi/10.1103/PhysRevB.65.235412, doi:10.1103/PhysRevB.65.235412.

[94] H. Ochoa, Eduardo V. Castro, M. I. Katsnelson, and F. Guinea. Temperature-dependent resistivity in bilayer graphene due to flexural phonons. *Phys. Rev. B*, 83:235416, Jun 2011. URL: https://link.aps.org/doi/10.1103/PhysRevB.83.235416, doi:10.1103/PhysRevB.83.235416.

[95] K. M. Borysenko, J. T. Mullen, X. Li, Y. G. Semenov, J. M. Zavada, M. Buongiorno Nardelli, and K. W. Kim. Electron-phonon interactions in bilayer graphene. *Phys. Rev. B*, 83:161402, Apr 2011. URL: https://link.aps.org/doi/10.1103/PhysRevB.83.161402, doi:10.1103/PhysRevB.83.161402.

[96] Dong-Keun Ki and Alberto F. Morpurgo. High-quality multiterminal suspended graphene devices. *Nano Letters*, 13(11):5165–5170, 2013. URL: https://doi.org/10.1021/nl402462q, doi:10.1021/nl402462q.

[97] James C. Garland and R. Bowers. Evidence for electron-electron scattering in the low-temperature resistivity of simple metals. *Phys. Rev. Lett.*, 21:1007–1009, Sep 1968. URL: https://link.aps.org/doi/10.1103/PhysRevLett.21.1007, doi:10.1103/PhysRevLett.21.1007.

[98] D. Svintsov, V. Vyurkov, S. Yurchenko, T. Otsuji, and V. Ryzhii. Hydrodynamic model for electron-hole plasma in graphene. *Journal of Applied Physics*, 111(8):083715, 2012. URL: https://doi.org/10.1063/1.4705382, doi:10.1063/1.4705382.

[99] Francesco M. D. Pellegrino, Iacopo Torre, and Marco Polini. Nonlocal transport and the hall viscosity of two-dimensional hydrodynamic electron liquids. *Phys. Rev. B*, 96:195401, Nov 2017. URL: https://link.aps.org/doi/10.1103/PhysRevB.96.195401, doi:10.1103/PhysRevB.96.195401.

[100] R. Bistritzer and A. H. MacDonald. Hydrodynamic theory of transport in doped graphene. *Phys. Rev. B*, 80:085109, Aug 2009. URL: https://link.aps.org/doi/10.1103/PhysRevB.80.085109, doi:10.1103/PhysRevB.80.085109.

[101] Markus Müller, Jörg Schmalian, and Lars Fritz. Graphene: A nearly perfect fluid. *Phys. Rev. Lett.*, 103:025301, Jul 2009. URL: https://link.aps.org/doi/10.1103/PhysRevLett.103.025301, doi:10.1103/PhysRevLett.103.025301.

[102] A. V. Andreev, Steven A. Kivelson, and B. Spivak. Hydrodynamic description of transport in strongly correlated electron systems. *Phys. Rev. Lett.*, 106:256804, Jun 2011. URL: https://link.aps.org/doi/10.1103/PhysRevLett.106.256804, doi:10.1103/PhysRevLett.106.256804.

[103] B. N. Narozhny, I. V. Gornyi, M. Titov, M. Schütt, and A. D. Mirlin. Hydrodynamics in graphene: Linear-response transport. *Phys. Rev. B*, 91:035414, Jan 2015. URL: https://link.aps.org/doi/10.1103/PhysRevB.91.035414, doi:10.1103/PhysRevB.91.035414.

[104] Markus Müller and Subir Sachdev. Collective cyclotron motion of the relativistic plasma in graphene. *Phys. Rev. B*, 78:115419, Sep 2008. URL: https://link.aps.org/doi/10.1103/PhysRevB.78.115419, doi:10.1103/PhysRevB.78.115419.

[105] J. C. W. Song, D. A. Abanin, and L. S. Levitov. Coulomb drag mechanisms in graphene. *Nano Letters*, 13(8):3631–3637, 2013. URL: https://doi.org/10.1021/nl401475u, doi:10.1021/nl401475u.

[106] D. A. Abanin, R. V. Gorbachev, K. S. Novoselov, A. K. Geim, and L. S. Levitov. Giant spin-hall effect induced by the zeeman interaction in graphene. *Phys. Rev. Lett.*, 107:096601, Aug 2011. URL: https://link.aps.org/doi/10.1103/PhysRevLett.107.096601, doi:10.1103/PhysRevLett.107.096601.

[107] M. Titov, R. V. Gorbachev, B. N. Narozhny, T. Tudorovskiy, M. Schütt, P. M. Ostrovsky, I. V. Gornyi, A. D. Mirlin, M. I. Katsnelson, K. S. Novoselov, A. K. Geim, and L. A. Ponomarenko. Giant magnetodrag in graphene at charge neutrality. *Phys. Rev. Lett.*, 111:166601, Oct 2013. URL: https://link.aps.org/doi/10.1103/PhysRevLett.111.166601, doi:10.1103/PhysRevLett.111.166601.

[108] V.F. Gantmakher and I.B. Levinson. Effect of collisions between carriers on the dissipative conductivity. *Sov. Phys. JETP*, page 133, 1978.

[109] Philipp T. Dumitrescu. Shear viscosity in a non-fermi-liquid phase of a quadratic semimetal. *Phys. Rev. B*, 92:121102, Sep 2015. URL: https://link.aps.org/doi/10.1103/PhysRevB.92.121102, doi:10.1103/PhysRevB.92.121102.

[110] Lyman Spitzer and Richard Härm. Transport phenomena in a completely ionized gas. *Phys. Rev.*, 89:977–981, Mar 1953. URL: https://link.aps.org/doi/10.1103/PhysRev.89.977, doi:10.1103/PhysRev.89.977.

[111] Kitinan Pongsangangan, Simonas Grubinskas, and Lars Fritz. Thermo-electric response close to the Dirac point: The role of particle-hole pairs. *arXiv e-prints*, page arXiv:2005.12790, May 2020. arXiv:2005.12790.

[112] Mohammad Zarenia, Shaffique Adam, and Giovanni Vignale. Temperature collapse of the electric conductivity in bilayer graphene. *Phys. Rev. Research*, 2:023391, Jun 2020. URL: https://link.aps.org/doi/10.1103/PhysRevResearch.2.023391, doi:10.1103/PhysRevResearch.2.023391.

[113] Cheng Tan, Derek Y. H. Ho, Lei Wang, J. I. A. Li, Indra Yudhistira, Daniel A. Rhodes, Takashi Taniguchi, Kenji Watanabe, Kenneth Shepard, Paul L. McEuen, Cory R. Dean, Shaffique Adam, and James Hone. Realization of a universal hydrodynamic semiconductor in ultra-clean dual-gated bilayer graphene. *arXiv e-prints*, page arXiv:1908.10921, August 2019. arXiv:1908.10921.

[114] Youngwoo Nam, Dong-Keun Ki, Mikito Koshino, Edward McCann, and Alberto F Morpurgo. Interaction-induced insulating state in thick multilayer graphene. *2D Materials*, 3(4):045014, oct 2016. URL: https://doi.org/10.1088%2F2053-1583%2F3%2F4%2F045014, doi:10.1088/2053-1583/3/4/045014.

[115] Youngwoo Nam, Dong-Keun Ki, David Soler-Delgado, and Alberto F. Morpurgo. A family of finite-temperature electronic phase transitions in graphene multilayers. *Science*, 362(6412):324–328, 2018. URL: https://science.sciencemag.org/content/362/6412/324, doi:10.1126/science.aar6855.

[116] H. M. Wang, Y. H. Wu, Z. H. Ni, and Z. X. Shen. Electronic transport and layer engineering in multilayer graphene structures. *Applied Physics Letters*, 92(5):053504, 2008. URL: https://doi.org/10.1063/1.2840713, doi:10.1063/1.2840713.

[117] Jianting Ye, Monica F. Craciun, Mikito Koshino, Saverio Russo, Seiji Inoue, Hongtao Yuan, Hidekazu Shimotani, Alberto F. Morpurgo, and Yoshihiro Iwasa. Accessing the transport properties of graphene and its multilayers at high carrier density. *Proceedings of the National Academy of Sciences of the United States of America*, 108(32):13002–13006, Aug 2011. URL: https://www.ncbi.nlm.nih.gov/pubmed/21828007, doi:10.1073/pnas.1018388108.

[118] Andrew Lucas and Kin Chung Fong. Hydrodynamics of electrons in graphene. *Journal of Physics: Condensed Matter*, 30(5):053001, jan 2018. URL: https://doi.org/10.1088%2F1361-648x%2Faaa274, doi:10.1088/1361-648x/aaa274.

[119] Uri Vool, Assaf Hamo, Georgios Varnavides, Yaxian Wang, Tony X. Zhou, Nitesh Kumar, Yuliya Dovzhenko, Ziwei Qiu, Christina A. C. Garcia, Andrew T. Pierce, Johannes Gooth, Polina Anikeeva, Claudia Felser, Prineha Narang, and Amir Yacoby. Imaging phonon-mediated hydrodynamic flow in WTe2 with cryogenic quantum magnetometry. *arXiv e-prints*, page arXiv:2009.04477, September 2020. arXiv:2009.04477.

[120] Chenguang Fu, Satya N. Guin, Thomas Scaffidi, Yan Sun, Rana Saha, Sarah J. Watzman, Abhay K. Srivastava, Guowei Li, Walter Schnelle, Stuart S. P. Parkin, Claudia Felser, and Johannes Gooth. Largely suppressed magneto-thermal conductivity and enhanced magneto-thermoelectric properties in ptsn¡sub¿4¡/sub¿. *Research*, 2020:4643507, Apr 2020. URL: https://doi.org/10.34133/2020/4643507, doi:10.34133/2020/4643507.

[121] Alexandre Jaoui, Benoît Fauqué, Carl Willem Rischau, Alaska Subedi, Chenguang Fu, Johannes Gooth, Nitesh Kumar, Vicky Süß, Dmitrii L. Maslov, Claudia Felser, and Kamran Behnia. Departure from the wiedemann–franz law in wp2 driven by mismatch in t-square resistivity prefactors. *npj Quantum Materials*, 3(1):64, Dec 2018. URL: https://doi.org/10.1038/s41535-018-0136-x, doi:10.1038/s41535-018-0136-x.

[122] J. Gooth, F. Menges, N. Kumar, V. Süβ, C. Shekhar, Y. Sun, U. Drechsler, R. Zierold, C. Felser, and B. Gotsmann. Thermal and electrical signatures of a hydrodynamic electron fluid in tungsten diphosphide. *Nature Communications*, 9(1):4093, Oct 2018. URL: https://doi.org/10.1038/s41467-018-06688-y, doi:10.1038/s41467-018-06688-y.

[123] A P Mackenzie. The properties of ultrapure delafossite metals. *Reports on Progress in Physics*, 80(3):032501, jan 2017. URL: https://doi.org/10.1088/1361-6633/aa50e5, doi:10.1088/1361-6633/aa50e5.

[124] Philip J. W. Moll, Pallavi Kushwaha, Nabhanila Nandi, Burkhard Schmidt, and Andrew P. Mackenzie. Evidence for hydrodynamic electron flow in pdcoo2. *Science*, 351(6277):1061–1064, 2016. URL: https://science.sciencemag.org/content/351/6277/1061, arXiv:https://science.sciencemag.org/content/351/6277/1061.full.pdf, doi:10.1126/science.aac8385.

[125] Tjacco Koskamp. *Viscous electron systems with coupling tothe spin degree of freedom*. PhD thesis, TU Eindhoven, 2020.

[126] E. Knill, R. Laflamme, and G. J. Milburn. A scheme for efficient quantum computation with linear optics. *Nature*, 409:46 EP –, Jan 2001. Article. URL: http://dx.doi.org/10.1038/35051009.

[127] Michael Moskalets. Single-particle emission at finite temperatures. *Low Temperature Physics*, 43(7):865–876, 2017. doi:https://doi.org/10.1063/1.4995639.

[128] FD Parmentier, Erwann Bocquillon, Adrien Mahé, J-M Berroir, DC Glattli, Bernard Plaçais, Gwendal Fève, A Cavanna, and Yong Jin. Noise of a single electron emitter: Experiment. In *21st International Conference on Noise and Fluctuations (ICNF) 2011*, pages 94–99. doi:10.1109/ICNF.2011.5994394.

[129] Ch Grenier, Rémy Hervé, Erwann Bocquillon, François D Parmentier, Bernard Plaçais, Jean-Marc Berroir, Gwendal Fève, and Pascal Degiovanni. Single-electron quantum tomography in quantum hall edge channels. *New J. Phys*, 13(9):093007, 2011. URL: http://stacks.iop.org/1367-2630/13/i=9/a=093007.

[130] FD Parmentier, Erwann Bocquillon, J-M Berroir, DC Glattli, Bernard Plaçais, Gwendal Fève, Mathias Albert, Christian Flindt, and Markus Büttiker. Current noise spectrum of a single-particle emitter: Theory and experiment. *Phys. Rev. B*, 85(16):165438, 2012. doi:https://doi.org/10.1103/PhysRevB.85.165438.

[131] Erwann Bocquillon, FD Parmentier, Charles Grenier, J-M Berroir, Pascal Degiovanni, DC Glattli, Bernard Plaçais, A Cavanna, Yong Jin, and Gwendal Fève. Electron quantum optics: partitioning electrons one by one. *Phys. Rev. Lett.*, 108(19):196803, 2012. doi:10.1103/PhysRevLett.108.196803.

[132] Michael Moskalets, Géraldine Haack, and Markus Büttiker. Single-electron source: Adiabatic versus nonadiabatic emission. *Phys. Rev. B*, 87(12):125429, 2013. doi:https://doi.org/10.1103/PhysRevB.87.125429.

[133] Michael Moskalets and Markus Büttiker. Heat production and current noise for single-and double-cavity quantum capacitors. *Phys. Rev. B*, 80(8):081302, 2009. doi:10.1103/PhysRevB.80.081302.

[134] Vyacheslavs Kashcheyevs and Janis Timoshenko. Quantum fluctuations and coherence in high-precision single-electron capture. *Phys. Rev. Lett.*, 109(21):216801, 2012. doi:10.1103/PhysRevLett.109.216801.

[135] Daniel Loss and David P. DiVincenzo. Quantum computation with quantum dots. *Phys. Rev. A*, 57:120–126, Jan 1998. URL: https://link.aps.org/doi/10.1103/PhysRevA.57.120, doi:10.1103/PhysRevA.57.120.

[136] K. K. Likharev. Single-electron devices and their applications. *Proceedings of the IEEE*, 87(4):606–632, 1999. doi:10.1109/5.752518.

[137] Jukka P. Pekola, Olli-Pentti Saira, Ville F. Maisi, Antti Kemppinen, Mikko Möttönen, Yuri A. Pashkin, and Dmitri V. Averin. Single-electron current sources: Toward a refined definition of the ampere. *Rev. Mod. Phys.*, 85:1421–1472, Oct 2013. URL: https://link.aps.org/doi/10.1103/RevModPhys.85.1421, doi:10.1103/RevModPhys.85.1421.

[138] H. Bartolomei, M. Kumar, R. Bisognin, A. Marguerite, J.-M. Berroir, E. Bocquillon, B. Plaçais, A. Cavanna, Q. Dong, U. Gennser, Y. Jin, and G. Fève. Fractional statistics in anyon collisions. *Science*, 368(6487):173–177, 2020. URL: https://science.sciencemag.org/content/368/6487/173, arXiv:https://science.sciencemag.org/content/368/6487/173.full.pdf, doi:10.1126/science.aaz5601.

[139] J. Nakamura, S. Liang, G. C. Gardner, and M. J. Manfra. Direct observation of anyonic braiding statistics. *Nature Physics*, 16(9):931–936, Sep 2020. URL: https://doi.org/10.1038/s41567-020-1019-1, doi:10.1038/s41567-020-1019-1.

[140] Leonid S. Levitov, Hyunwoo Lee, and Gordey B. Lesovik. Electron counting statistics and coherent states of electric current. *J. Math. Phys*, 37(10):4845–4866, 1996. doi:10.1063/1.531672.

[141] D. A. Ivanov, H. W. Lee, and L. S. Levitov. Coherent states of alternating current. *Phys. Rev. B*, 56(11):6839–6850, Sep 1997. doi:10.1103/physrevb.56.6839.

[142] J. Keeling, I. Klich, and L. S. Levitov. Minimal excitation states of electrons in one-dimensional wires. *Phys. Rev. Lett.*, 97:116403, Sep 2006. URL: https://link.aps.org/doi/10.1103/PhysRevLett.97.116403, doi:10.1103/PhysRevLett.97.116403.

[143] Luca Vannucci, Flavio Ronetti, Dario Ferraro, Jérôme Rech, Thibaut Jonckheere, Thierry Martin, and Maura Sassetti. Photoassisted shot noise spectroscopy at fractional filling factor. *J. Phys. Conf. Ser*, 969(1):012143, 2018. URL: http://stacks.iop.org/1742-6596/969/i=1/a=012143.

[144] Luca Vannucci, Flavio Ronetti, Jérôme Rech, Dario Ferraro, Thibaut Jonckheere, Thierry Martin, and Maura Sassetti. Minimal excitation states for heat transport in driven quantum hall systems. *Phys. Rev. B*, 95:245415, Jun 2017. URL: https://link.aps.org/doi/10.1103/PhysRevB.95.245415, doi:10.1103/PhysRevB.95.245415.

[145] D. Chevallier, J. Rech, T. Jonckheere, C. Wahl, and T. Martin. Poissonian tunneling through an extended impurity in the quantum hall effect. *Phys. Rev. B*, 82:155318, Oct 2010. URL: https://link.aps.org/doi/10.1103/PhysRevB.82.155318, doi:10.1103/PhysRevB.82.155318.

[146] F. Ronetti, L. Vannucci, D. Ferraro, T. Jonckheere, J. Rech, T. Martin, and M. Sassetti. Crystallization of levitons in the fractional quantum hall regime. *Phys. Rev. B*, 98:075401, Aug 2018. URL: https://link.aps.org/doi/10.1103/PhysRevB.98.075401, doi:10.1103/PhysRevB.98.075401.

[147] D. Ferraro, J. Rech, T. Jonckheere, and T. Martin. Single quasiparticle and electron emitter in the fractional quantum hall regime. *Phys. Rev. B*, 91:205409, May 2015. URL: https://link.aps.org/doi/10.1103/PhysRevB.91.205409, doi:10.1103/PhysRevB.91.205409.

[148] Gwendal Fève, Adrien Mahé, J-M Berroir, Takis Kontos, Bernard Placais, DC Glattli, A Cavanna, Bernard Etienne, and Yong Jin. An on-demand coherent single-electron source. *Science*, 316(5828):1169–1172, 2007. doi:10.1126/science.1141243.

[149] J Keeling, AV Shytov, and LS Levitov. Coherent particle transfer in an on-demand single-electron source. *Phys. Rev. Lett.*, 101(19):196404, 2008. doi:https://doi.org/10.1103/PhysRevLett.101.196404.

[150] A. Furusaki and K. A. Matveev. Occupation of a Resonant Level Coupled to a Chiral Luttinger Liquid. *Phys. Rev. Lett.*, 88(22):226404, June 2002. arXiv:cond-mat/0112426, doi:10.1103/PhysRevLett.88.226404.

[151] A. J. Leggett, S. Chakravarty, A. T. Dorsey, Matthew P. A. Fisher, Anupam Garg, and W. Zwerger. Dynamics of the dissipative two-state system. *Rev. Mod. Phys.*, 59:1–85, Jan 1987. URL: https://link.aps.org/doi/10.1103/RevModPhys.59.1, doi:10.1103/RevModPhys.59.1.

[152] Gordon Baym and Christopher Pethick. *Landau Fermi-liquid theory*, volume 1. Wiley Online Library, 1991.

[153] Thierry Giamarchi. *Quantum physics in one dimension*, volume 121. Oxford university press, 2004.

[154] D. C. Tsui, H. L. Stormer, and A. C. Gossard. Two-dimensional magnetotransport in the extreme quantum limit. *Phys. Rev. Lett.*, 48:1559–1562, May 1982. URL: https://link.aps.org/doi/10.1103/PhysRevLett.48.1559, doi:10.1103/PhysRevLett.48.1559.

[155] R. B. Laughlin. Anomalous quantum hall effect: An incompressible quantum fluid with fractionally charged excitations. *Phys. Rev. Lett.*, 50:1395–1398, May 1983. URL: https://link.aps.org/doi/10.1103/PhysRevLett.50.1395, doi:10.1103/PhysRevLett.50.1395.

[156] R. B. Laughlin. Anomalous quantum hall effect: An incompressible quantum fluid with fractionally charged excitations. *Phys. Rev. Lett.*, 50:1395–1398, May 1983. URL: https://link.aps.org/doi/10.1103/PhysRevLett.50.1395, doi:10.1103/PhysRevLett.50.1395.

[157] X.-G. Wen. Theory of the edge states in fractional quantum hall effects. *Int. J. Mod. Phys. B*, 06(10):1711–1762, May 1992. doi:10.1142/s0217979292000840.

[158] Marc A Kastner. Artificial atoms. *Physics today*, 46:24–24, 1993.

[159] Tapash Chakraborty. *Quantum Dots: A survey of the properties of artificial atoms*. Elsevier, 1999.

[160] Sven Rühle, Menny Shalom, and Arie Zaban. Quantum-dot-sensitized solar cells. *ChemPhysChem*, 11(11):2290–2304, 2010.

[161] Moshe Goldstein and Richard Berkovits. Capacitance of a resonant level coupled to Luttinger liquids. *Phys. Rev. B*, 82:161307, 2010. arXiv:1101.3723, doi:10.1103/PhysRevB.82.161307.

[162] Moshe Goldstein and Richard Berkovits. Density of states of a dissipative quantum dot coupled to a quantum wire. *Phys. Rev. B.*, 82:235315. doi:10.1103/PhysRevB.82.235315.

[163] Moshe Goldstein and Richard Berkovits. Duality between different geometries of a resonant level in a luttinger liquid. *Phys. Rev. Lett*, 104:106403, 2010. arXiv:0907.0424, doi:10.1103/PhysRevLett.104.106403.

[164] Entanglement entropy and quantum phase transitions in quantum dots coupled to Luttinger liquid wires. *Phys. Rev. B.*, 83:245112, 2011. doi:10.1103/PhysRevB.83.245112.

[165] P. Wächter, V. Meden, and K. Schönhammer. Charging of a quantum dot coupled to Luttinger-liquid leads. *Phys. Rev. B*, 76:125316, 2007. doi:10.1103/PhysRevB.76.125316.

[166] Gregory A. Fiete, Waheb Bishara, and Chetan Nayak. Exotic resonant level models in non-Abelian quantum Hall states coupled to quantum dots. *Phys. Rev. B*, 82:035301, 2010. doi:10.1103/PhysRevB.82.035301.

[167] A Komnik and A O Gogolin. Transport, optical properties, and quantum ratchet effects for quantum dots and molecules coupled to Luttinger liquids. *Phys. Rev. B*, 68:23523. doi:10.1103/PhysRevB.68.235323.

[168] Karyn Le Hur and Mei-Rong Li. Unification of electromagnetic noise and luttinger liquid via a quantum dot. *Phys. Rev. B*, 72:073305, Aug 2005. URL: https://link.aps.org/doi/10.1103/PhysRevB.72.073305, doi:10.1103/PhysRevB.72.073305.

[169] Colin Rylands, Natan Andrei, M Goldstein, Y Weiss, and R Berkovits. Interacting resonant level coupled to a luttinger liquid: Universality of thermodynamic properties. *EPL*, 86:67012, 2009. URL: www.epljournal.org, doi:10.1209/0295-5075/86/67012.

[170] A. Galda, I. V. Yurkevich, and I. V. Lerner. Effect of electron-phonon coupling on transmission through luttinger liquid hybridized with resonant level. *EPL*, 93:17009, 2011. doi:10.1209/0295-5075/93/17009.

[171] Kai Hua Yang, Yang Chen, Huai Yu Wang, and Bei Yun Liu. Density of states of a strongly correlated quantum dot coupled to Luttinger liquid leads. *Phys. Lett. A*, 377:687–693, 2013. doi:10.1016/j.physleta.2013.01.020.

[172] G. Wagner, D. X. Nguyen, D. L. Kovrizhin, and S. H. Simon. Interaction effects and charge quantization in single-particle quantum dot emitters. *ArXiv e-prints*, August 2018. arXiv:1808.08240.

[173] Glenn Wagner, Dung Xuan Nguyen, Dmitry Kovrizhin, and Steven H. Simon. *to be published*, 2018.

[174] R. A. J. van Elburg and K. Schoutens. Quasiparticles in fractional quantum hall effect edge theories. *Phys. Rev. B*, 58:15704–15716, Dec 1998. URL: https://link.aps.org/doi/10.1103/PhysRevB.58.15704, doi:10.1103/PhysRevB.58.15704.

[175] RJ Schoelkopf, AA Clerk, SM Girvin, KW Lehnert, and MH Devoret. Qubits as spectrometers of quantum noise. In *Quantum noise in mesoscopic physics*, pages 175–203. Springer, 2003.

[176] Yuriy Makhlin, Gerd Schön, and Alexander Shnirman. Dissipation in josephson qubits. In *New Directions in Mesoscopic Physics (Towards Nanoscience)*, pages 197–224. Springer, 2003.

[177] Ludwig Hartmann, Igor Goychuk, Milena Grifoni, and Peter Hänggi. Driven tunneling dynamics: Bloch-redfield theory versus path-integral approach. *Phys. Rev. E*, 61(5):R4687, 2000. doi:10.1103/PhysRevE.61.R4687.

[178] Peter P Orth, Adilet Imambekov, and Karyn Le Hur. Nonperturbative stochastic method for driven spin-boson model. *Phys. Rev. B*, 87(1):014305, 2013. doi:10.1103/PhysRevB.87.014305.

[179] Pascal Cedraschi and Markus Büttiker. Quantum coherence of the ground state of a mesoscopic ring. *Annals of Physics*, 289(1):1 – 23, 2001. URL: http://www.sciencedirect.com/science/article/pii/S0003491601961160, doi:https://doi.org/10.1006/aphy.2001.6116.

[180] Ralf Bulla, Hyun-Jung Lee, Ning-Hua Tong, and Matthias Vojta. Numerical renormalization group for quantum impurities in a bosonic bath. *Phys. Rev. B*, 71:045122, Jan 2005. URL: https://link.aps.org/doi/10.1103/PhysRevB.71.045122, doi:10.1103/PhysRevB.71.045122.

[181] Frithjof B. Anders and Avraham Schiller. Real-time dynamics in quantum-impurity systems: A time-dependent numerical renormalization-group approach. *Phys. Rev. Lett.*, 95:196801, Oct 2005. URL: https://link.aps.org/doi/10.1103/PhysRevLett.95.196801, doi:10.1103/PhysRevLett.95.196801.

[182] Michael L. Wall, Arghavan Safavi-Naini, and Ana Maria Rey. Simulating generic spin-boson models with matrix product states. *Phys. Rev. A*, 94:053637, Nov 2016. URL: https://link.aps.org/doi/10.1103/PhysRevA.94.053637, doi:10.1103/PhysRevA.94.053637.

[183] A. Strathearn, P. Kirton, D. Kilda, J. Keeling, and B. W. Lovett. Efficient non-markovian quantum dynamics using time-evolving matrix product operators. *Nature Communications*, 9(1):3322, 2018. URL: https://doi.org/10.1038/s41467-018-05617-3, doi:10.1038/s41467-018-05617-3.

[184] M. Grifoni, E. Paladino, and U. Weiss. Dissipation, decoherence and preparation effects in the spin-boson system. *Eur. Phys. J. B*, 10(4):719–729, Jun 1999. URL: https://doi.org/10.1007/s100510050903, doi:10.1007/s100510050903.

[185] R. Görlich, M. Sassetti, and U. Weiss. Low-temperature properties of biased two-level systems: Effects of frequency-dependent damping. *EPL*, 10(6):507, 1989. URL: http://stacks.iop.org/0295-5075/10/i=6/a=001.

[186] Martijn Wubs, Keiji Saito, Sigmund Kohler, Peter Hänggi, and Yosuke Kayanuma. Gauging a quantum heat bath with dissipative landau-zener transitions. *Phys. Rev. Lett.*, 97:200404, Nov 2006. URL: https://link.aps.org/doi/10.1103/PhysRevLett.97.200404, doi:10.1103/PhysRevLett.97.200404.

[187] Keiji Saito, Martijn Wubs, Sigmund Kohler, Yosuke Kayanuma, and Peter Hänggi. Dissipative landau-zener transitions of a qubit: Bath-specific and universal behavior. *Phys. Rev. B*, 75:214308, Jun 2007. URL: https://link.aps.org/doi/10.1103/PhysRevB.75.214308, doi:10.1103/PhysRevB.75.214308.

[188] Steven H. Simon. Proposal for a quantum hall pump. *Phys. Rev. B*, 61:R16327–R16330, Jun 2000. URL: https://link.aps.org/doi/10.1103/PhysRevB.61.R16327, doi:10.1103/PhysRevB.61.R16327.

[189] J. Keeling. Private communication.

[190] J.P. Eisenstein. Exciton condensation in bilayer quantum hall systems. *Annual Review of Condensed Matter Physics*, 5(1):159–181, 2014. URL: https://doi.org/10.1146/annurev-conmatphys-031113-133832, arXiv:https://doi.org/10.1146/annurev-conmatphys-031113-133832, doi:10.1146/annurev-conmatphys-031113-133832.

[191] Z F Ezawa and G Tsitsishvili. Quantum hall ferromagnets. *Reports on Progress in Physics*, 72(8):086502, jul 2009. URL: https://doi.org/10.1088%2F0034-4885%2F72%2F8%2F086502, doi:10.1088/0034-4885/72/8/086502.

[192] K. Moon, H. Mori, Kun Yang, S. M. Girvin, A. H. MacDonald, L. Zheng, D. Yoshioka, and Shou-Cheng Zhang. Spontaneous interlayer coherence in double-layer quantum hall systems: Charged vortices and kosterlitz-thouless phase transitions. *Phys. Rev. B*, 51:5138–5170, Feb 1995. URL: https://link.aps.org/doi/10.1103/PhysRevB.51.5138, doi:10.1103/PhysRevB.51.5138.

[193] Debanjan Chowdhury, Brian Skinner, and Patrick A. Lee. Effect of magnetization on the tunneling anomaly in compressible quantum hall states. *Phys. Rev. Lett.*, 120:266601, Jun 2018. URL: https://link.aps.org/doi/10.1103/PhysRevLett.120.266601, doi:10.1103/PhysRevLett.120.266601.

[194] I. B. Spielman, M. Kellogg, J. P. Eisenstein, L. N. Pfeiffer, and K. W. West. Onset of interlayer phase coherence in a bilayer two-dimensional electron system: Effect of layer density imbalance. *Phys. Rev. B*, 70:081303, Aug 2004. URL: https://link.aps.org/doi/10.1103/PhysRevB.70.081303, doi:10.1103/PhysRevB.70.081303.

[195] W.R. Clarke, A.P. Micolich, A.R. Hamilton, M.Y. Simmons, M. Pepper, and D.A. Ritchie. Stability of the bilayer $\nu = 1$ quantum hall state under charge imbalance. *Physica E: Low-dimensional Systems and Nanostructures*, 22(1):40 – 43, 2004. 15th International Conference on Electronic Propreties of Two-Dimensional Systems (EP2DS-15). URL: http://www.sciencedirect.com/science/article/pii/S1386947703007847, doi:https://doi.org/10.1016/j.physe.2003.11.211.

[196] A. R. Champagne, A. D. K. Finck, J. P. Eisenstein, L. N. Pfeiffer, and K. W. West. Charge imbalance and bilayer two-dimensional electron systems at $\nu_T = 1$. *Phys. Rev. B*, 78:205310, Nov 2008. URL: https://link.aps.org/doi/10.1103/PhysRevB.78.205310, doi:10.1103/PhysRevB.78.205310.

[197] J. P. Eisenstein, L. N. Pfeiffer, and K. W. West. Precursors to exciton condensation in quantum hall bilayers. *Phys. Rev. Lett.*, 123:066802, Aug 2019. URL: https://link.aps.org/doi/10.1103/PhysRevLett.123.066802, doi:10.1103/PhysRevLett.123.066802.

[198] J. P. Eisenstein, L. N. Pfeiffer, and K. W. West. Interlayer interactions and the fermi energy of bilayer composite-fermion metals. *Phys. Rev. B*, 98:201406, Nov 2018. URL: https://link.aps.org/doi/10.1103/PhysRevB.98.201406, doi:10.1103/PhysRevB.98.201406.

[199] A. D. K. Finck, J. P. Eisenstein, L. N. Pfeiffer, and K. W. West. Exciton transport and andreev reflection in a bilayer quantum hall system. *Phys. Rev. Lett.*, 106:236807, Jun 2011. URL: https://link.aps.org/doi/10.1103/PhysRevLett.106.236807, doi:10.1103/PhysRevLett.106.236807.

[200] M. Kellogg, J. P. Eisenstein, L. N. Pfeiffer, and K. W. West. Bilayer quantum hall systems at $\nu_T = 1$: Coulomb drag and the transition from weak to strong interlayer coupling. *Phys. Rev. Lett.*, 90:246801, Jun 2003. URL: https://link.aps.org/doi/10.1103/PhysRevLett.90.246801, doi:10.1103/PhysRevLett.90.246801.

[201] J P Eisenstein, A D K Finck, D Nandi, L N Pfeiffer, and K W West. Exciton transport in a bilayer quantum hall superfluid. *Journal of Physics: Conference Series*, 456:012009, aug 2013. URL: https://doi.org/10.1088%2F1742-6596%2F456%2F1%2F012009, doi:10.1088/1742-6596/456/1/012009.

[202] J. P. Eisenstein, T. Khaire, D. Nandi, A. D. K. Finck, L. N. Pfeiffer, and K. W. West. Spin and the coulomb gap in the half-filled lowest landau level. *Phys. Rev. B*, 94:125409, Sep 2016. URL: https://link.aps.org/doi/10.1103/PhysRevB.94.125409, doi:10.1103/PhysRevB.94.125409.

[203] A. R. Champagne, J. P. Eisenstein, L. N. Pfeiffer, and K. W. West. Evidence for a finite-temperature phase transition in a bilayer quantum hall system. *Phys. Rev. Lett.*, 100:096801, Mar 2008. URL: https://link.aps.org/doi/10.1103/PhysRevLett.100.096801, doi:10.1103/PhysRevLett.100.096801.

[204] I. B. Spielman, J. P. Eisenstein, L. N. Pfeiffer, and K. W. West. Observation of a linearly dispersing collective mode in a quantum hall ferromagnet. *Phys. Rev. Lett.*, 87:036803, Jul 2001. URL: https://link.aps.org/doi/10.1103/PhysRevLett.87.036803, doi:10.1103/PhysRevLett.87.036803.

[205] A. R. Champagne, J. P. Eisenstein, L. N. Pfeiffer, and K. W. West. Evidence for a finite-temperature phase transition in a bilayer quantum hall system. *Phys. Rev. Lett.*, 100:096801, Mar 2008. URL: https://link.aps.org/doi/10.1103/PhysRevLett.100.096801, doi:10.1103/PhysRevLett.100.096801.

[206] Stefano Luin, Vittorio Pellegrini, Aron Pinczuk, Brian S. Dennis, Loren N. Pfeiffer, and Ken W. West. Resonant rayleigh scattering from bilayer quantum hall phases. *Phys. Rev. Lett.*, 97:216802, Nov 2006. URL: https://link.aps.org/doi/10.1103/PhysRevLett.97.216802, doi:10.1103/PhysRevLett.97.216802.

[207] J. I. A. Li, T. Taniguchi, K. Watanabe, J. Hone, and C. R. Dean. Excitonic superfluid phase in double bilayer graphene. *Nature Physics*, 13(8):751–755, Aug 2017. URL: https://doi.org/10.1038/nphys4140, doi:10.1038/nphys4140.

[208] J. K. Jain. Composite-fermion approach for the fractional quantum hall effect. *Phys. Rev. Lett.*, 63:199–202, Jul 1989. URL: https://link.aps.org/doi/10.1103/PhysRevLett.63.199, doi:10.1103/PhysRevLett.63.199.

[209] J.K. Jain. Microscopic theory of the fractional quantum hall effect. *Advances in Physics*, 41(2):105–146, 1992. URL: https://doi.org/10.1080/00018739200101483, doi:10.1080/00018739200101483.

[210] S. C. Zhang, T. H. Hansson, and S. Kivelson. Effective-field-theory model for the fractional quantum hall effect. *Phys. Rev. Lett.*, 62:82–85, Jan 1989. URL: https://link.aps.org/doi/10.1103/PhysRevLett.62.82, doi:10.1103/PhysRevLett.62.82.

[211] Ana Lopez and Eduardo Fradkin. Fractional quantum hall effect and chern-simons gauge theories. *Phys. Rev. B*, 44:5246–5262, Sep 1991. URL: https://link.aps.org/doi/10.1103/PhysRevB.44.5246, doi:10.1103/PhysRevB.44.5246.

[212] Jainendra K. Jain. *Composite Fermions*. Cambridge University Press, 2007.

[213] O. Heinonen, editor. *Composite Fermions: A Unified View of the Quantum Hall Regime*. World Scientific, 1998.

[214] W. Kang, H. L. Stormer, L. N. Pfeiffer, K. W. Baldwin, and K. W. West. How real are composite fermions? *Phys. Rev. Lett.*, 71:3850–3853, Dec 1993. URL: https://link.aps.org/doi/10.1103/PhysRevLett.71.3850, doi:10.1103/PhysRevLett.71.3850.

[215] R. L. Willett, R. R. Ruel, K. W. West, and L. N. Pfeiffer. Experimental demonstration of a fermi surface at one-half filling of the lowest landau level. *Phys. Rev. Lett.*, 71:3846–3849, Dec 1993. URL: https://link.aps.org/doi/10.1103/PhysRevLett.71.3846, doi:10.1103/PhysRevLett.71.3846.

[216] J. K. Jain and P. W. Anderson. Beyond the fermi liquid paradigm: Hidden fermi liquids. *Proceedings of the National Academy of Sciences*, 106(23):9131–9134, 2009. URL: https://www.pnas.org/content/106/23/9131, doi:10.1073/pnas.0902901106.

[217] B. I. Halperin, Patrick A. Lee, and Nicholas Read. Theory of the half-filled landau level. *Phys. Rev. B*, 47:7312–7343, Mar 1993. URL: https://link.aps.org/doi/10.1103/PhysRevB.47.7312, doi:10.1103/PhysRevB.47.7312.

[218] Dam Thanh Son. Is the composite fermion a dirac particle? *Phys. Rev. X*, 5:031027, Sep 2015. URL: https://link.aps.org/doi/10.1103/PhysRevX.5.031027, doi:10.1103/PhysRevX.5.031027.

[219] Dung Xuan Nguyen, Siavash Golkar, Matthew M. Roberts, and Dam Thanh Son. Particle-hole symmetry and composite fermions in fractional quantum hall states. *Phys. Rev. B*, 97:195314, May 2018. URL: https://link.aps.org/doi/10.1103/PhysRevB.97.195314, doi:10.1103/PhysRevB.97.195314.

[220] Yogesh N. Joglekar and Allan H. MacDonald. Microscopic functional integral theory of quantum fluctuations in double-layer quantum hall ferromagnets. *Phys. Rev. B*, 64:155315, Sep 2001. URL: https://link.aps.org/doi/10.1103/PhysRevB.64.155315, doi:10.1103/PhysRevB.64.155315.

[221] Yogesh N. Joglekar and Allan H. MacDonald. Is there a dc josephson effect in bilayer quantum hall systems? *Phys. Rev. Lett.*, 87:196802, Oct 2001. URL: https://link.aps.org/doi/10.1103/PhysRevLett.87.196802, doi:10.1103/PhysRevLett.87.196802.

[222] Yogesh N. Joglekar and Allan H. MacDonald. Bias-voltage-induced phase transition in bilayer quantum hall ferromagnets. *Phys. Rev. B*, 65:235319, Jun 2002. URL: https://link.aps.org/doi/10.1103/PhysRevB.65.235319, doi:10.1103/PhysRevB.65.235319.

[223] A. H. MacDonald, P. M. Platzman, and G. S. Boebinger. Collapse of integer hall gaps in a double-quantum-well system. *Phys. Rev. Lett.*, 65:775–778, Aug 1990. URL: https://link.aps.org/doi/10.1103/PhysRevLett.65.775, doi:10.1103/PhysRevLett.65.775.

[224] H. A. Fertig. Energy spectrum of a layered system in a strong magnetic field. *Phys. Rev. B*, 40:1087–1095, Jul 1989. URL: https://link.aps.org/doi/10.1103/PhysRevB.40.1087, doi:10.1103/PhysRevB.40.1087.

[225] R. Côté, L. Brey, and A. H. MacDonald. Broken-symmetry ground states for the two-dimensional electron gas in a double-quantum-well system. *Phys. Rev. B*, 46:10239–10250, Oct 1992. URL: https://link.aps.org/doi/10.1103/PhysRevB.46.10239, doi:10.1103/PhysRevB.46.10239.

[226] Kentaro Nomura and Daijiro Yoshioka. Evolution of $\nu = 1$ bilayer quantum hall ferromagnet. *Phys. Rev. B*, 66:153310, Oct 2002. URL: https://link.aps.org/doi/10.1103/PhysRevB.66.153310, doi:10.1103/PhysRevB.66.153310.

[227] Zlatko Papic. *Fractional quantum Hall effect in multicomponent systems*. PhD thesis, Université Paris Sud-Paris XI, 2010.

[228] K. Park. Spontaneous pseudospin spiral order in bilayer quantum hall systems. *Phys. Rev. B*, 69:045319, Jan 2004. URL: https://link.aps.org/doi/10.1103/PhysRevB.69.045319, doi:10.1103/PhysRevB.69.045319.

[229] K. Park and S. Das Sarma. Coherent tunneling in exciton condensates of bilayer quantum hall systems. *Phys. Rev. B*, 74:035338, Jul 2006. URL: https://link.aps.org/doi/10.1103/PhysRevB.74.035338, doi:10.1103/PhysRevB.74.035338.

[230] John Schliemann, S. M. Girvin, and A. H. MacDonald. Strong correlation to weak correlation phase transition in bilayer quantum hall systems. *Phys. Rev. Lett.*, 86:1849–1852, Feb 2001. URL: https://link.aps.org/doi/10.1103/PhysRevLett.86.1849, doi:10.1103/PhysRevLett.86.1849.

[231] Zheng Zhu, Liang Fu, and D. N. Sheng. Numerical study of quantum hall bilayers at total filling $\nu_T = 1$: A new phase at intermediate layer distances. *Phys. Rev. Lett.*, 119:177601, Oct 2017. URL: https://link.aps.org/doi/10.1103/PhysRevLett.119.177601, doi:10.1103/PhysRevLett.119.177601.

[232] Naokazu Shibata and Daijiro Yoshioka. Ground state of ν= 1 bilayer quantum hall systems. *Journal of the Physical Society of Japan*, 75(4):043712–043712, 2006.

[233] Takao Morinari. Composite-fermion pairing in bilayer quantum hall systems. *Phys. Rev. B*, 59:7320–7322, Mar 1999. URL: https://link.aps.org/doi/10.1103/PhysRevB.59.7320, doi:10.1103/PhysRevB.59.7320.

[234] Hiroki Isobe and Liang Fu. Interlayer pairing symmetry of composite fermions in quantum hall bilayers. *Phys. Rev. Lett.*, 118:166401, Apr 2017. URL: https://link.aps.org/doi/10.1103/PhysRevLett.118.166401, doi:10.1103/PhysRevLett.118.166401.

[235] Inti Sodemann, Itamar Kimchi, Chong Wang, and T. Senthil. Composite fermion duality for half-filled multicomponent landau levels. *Phys. Rev. B*, 95:085135, Feb 2017. URL: https://link.aps.org/doi/10.1103/PhysRevB.95.085135, doi:10.1103/PhysRevB.95.085135.

[236] Meera M. Parish. *The BCS–BEC Crossover*, chapter Chapter 9, pages 179–197. URL: https://www.worldscientific.com/doi/abs/10.1142/9781783264766_0009.

[237] Kun Yang. Dipolar excitons, spontaneous phase coherence, and superfluid-insulator transition in bilayer quantum hall systems at $\nu = 1$. *Phys. Rev. Lett.*, 87:056802, Jul 2001. URL: https://link.aps.org/doi/10.1103/PhysRevLett.87.056802, doi:10.1103/PhysRevLett.87.056802.

[238] Gunnar Möller, Steven H. Simon, and Edward H. Rezayi. Paired composite fermion phase of quantum hall bilayers at $\nu = \frac{1}{2} + \frac{1}{2}$. *Phys. Rev. Lett.*, 101:176803, Oct 2008. URL: https://link.aps.org/doi/10.1103/PhysRevLett.101.176803, doi:10.1103/PhysRevLett.101.176803.

[239] Gunnar Möller, Steven H. Simon, and Edward H. Rezayi. Trial wave functions for $\nu = \frac{1}{2} + \frac{1}{2}$ quantum hall bilayers. *Phys. Rev. B*, 79:125106, Mar 2009. URL: https://link.aps.org/doi/10.1103/PhysRevB.79.125106, doi:10.1103/PhysRevB.79.125106.

[240] J. K. Jain and R. K. Kamilla. Quantitative study of large composite-fermion systems. *Phys. Rev. B*, 55:R4895–R4898, Feb 1997. URL: https://link.aps.org/doi/10.1103/PhysRevB.55.R4895, doi:10.1103/PhysRevB.55.R4895.

[241] E. Rezayi and N. Read. Fermi-liquid-like state in a half-filled landau level. *Phys. Rev. Lett.*, 72:900–903, Feb 1994. URL: https://link.aps.org/doi/10.1103/PhysRevLett.72.900, doi:10.1103/PhysRevLett.72.900.

[242] Dung Xuan Nguyen, Tankut Can, and Andrey Gromov. Particle-hole duality in the lowest landau level. *Phys. Rev. Lett.*, 118:206602, May 2017. URL: https://link.aps.org/doi/10.1103/PhysRevLett.118.206602, doi:10.1103/PhysRevLett.118.206602.

[243] E. H. Rezayi and F. D. M. Haldane. Incompressible paired hall state, stripe order, and the composite fermion liquid phase in half-filled landau levels. *Phys. Rev. Lett.*, 84:4685–4688, May 2000. URL: https://link.aps.org/doi/10.1103/PhysRevLett.84.4685, doi:10.1103/PhysRevLett.84.4685.

[244] Jainendra K. Jain. *Composite Fermions*. Cambridge University Press, 2007. doi:10.1017/CBO9780511607561.

[245] G. Fano, F. Ortolani, and E. Colombo. Configuration-interaction calculations on the fractional quantum hall effect. *Phys. Rev. B*, 34:2670–2680, Aug 1986. URL: https://link.aps.org/doi/10.1103/PhysRevB.34.2670, doi:10.1103/PhysRevB.34.2670.

[246] Y Xiang, D.Y Sun, W Fan, and X.G Gong. Generalized simulated annealing algorithm and its application to the thomson model. *Physics Letters A*, 233(3):216–220, 1997. URL: https://www.sciencedirect.com/science/article/pii/S037596019700474X, doi:https://doi.org/10.1016/S0375-9601(97)00474-X.

[247] Dam Thanh Son. Is the composite fermion a dirac particle? *Phys. Rev. X*, 5:031027, Sep 2015. URL: https://link.aps.org/doi/10.1103/PhysRevX.5.031027, doi:10.1103/PhysRevX.5.031027.

[248] Gunnar Möller and Steven H. Simon. Composite fermions in a negative effective magnetic field: A monte carlo study. *Phys. Rev. B*, 72:045344, Jul 2005. URL: https://link.aps.org/doi/10.1103/PhysRevB.72.045344, doi:10.1103/PhysRevB.72.045344.

[249] D. Kamburov, Yang Liu, M. A. Mueed, M. Shayegan, L. N. Pfeiffer, K. W. West, and K. W. Baldwin. What determines the fermi wave vector of composite fermions? *Phys. Rev. Lett.*, 113:196801, Nov 2014. URL: https://link.aps.org/doi/10.1103/PhysRevLett.113.196801, doi:10.1103/PhysRevLett.113.196801.

[250] Xiaomeng Liu, J. I. A. Li, Kenji Watanabe, Takashi Taniguchi, James Hone, Bertrand I. Halperin, Philip Kim, and Cory R. Dean. Crossover between Strongly-coupled and Weakly-coupled Exciton Superfluids. *arXiv e-prints*, pages ,see in particular Supplementary Material., December 2020. arXiv:2012.05916.

[251] Tai Tsun Wu and Chen Ning Yang. Some properties of monopole harmonics. *Phys. Rev. D*, 16:1018–1021, Aug 1977. URL: https://link.aps.org/doi/10.1103/PhysRevD.16.1018, doi:10.1103/PhysRevD.16.1018.

[252] Zhao Liu, Ajit C. Balram, Zlatko Papić, and Andrey Gromov. Quench dynamics of collective modes in fractional quantum hall bilayers. *Phys. Rev. Lett.*, 126:076604, Feb 2021. URL: https://link.aps.org/doi/10.1103/PhysRevLett.126.076604, doi:10.1103/PhysRevLett.126.076604.

[253] Scott D. Geraedts, Michael P. Zaletel, Roger S. K. Mong, Max A. Metlitski, Ashvin Vishwanath, and Olexei I. Motrunich. The half-filled landau level: The case for dirac composite fermions. *Science*, 352(6282):197–201, 2016. URL: https://science.sciencemag.org/content/352/6282/197, doi:10.1126/science.aad4302.

[254] Hantao Lu, S. Das Sarma, and Kwon Park. Superconducting order parameter for the even-denominator fractional quantum hall effect. *Phys. Rev. B*, 82:201303, Nov 2010. URL: https://link.aps.org/doi/10.1103/PhysRevB.82.201303, doi:10.1103/PhysRevB.82.201303.

[255] J. I. A. Li, Q. Shi, Y. Zeng, K. Watanabe, T. Taniguchi, J. Hone, and C. R. Dean. Pairing states of composite fermions in double-layer graphene. *Nature Physics*, 15(9):898–903, Sep 2019. URL: https://doi.org/10.1038/s41567-019-0547-z, doi:10.1038/s41567-019-0547-z.

[256] Xiaomeng Liu, Zeyu Hao, Kenji Watanabe, Takashi Taniguchi, Bertrand I. Halperin, and Philip Kim. Interlayer fractional quantum hall effect in a coupled graphene double layer. *Nature Physics*, 15(9):893–897, Sep 2019. URL: https://doi.org/10.1038/s41567-019-0546-0, doi:10.1038/s41567-019-0546-0.

[257] Ulrich Schollwöck. The density-matrix renormalization group in the age of matrix product states. *Annals of Physics*, 326(1):96–192, 2011. January 2011 Special Issue. URL: https://www.sciencedirect.com/science/article/pii/S0003491610001752, doi:https://doi.org/10.1016/j.aop.2010.09.012.

[258] Subir Sachdev. Condensed matter and ads/cft. *Lecture Notes in Physics*, page 273–311, 2011. URL: http://dx.doi.org/10.1007/978-3-642-04864-7_9, doi:10.1007/978-3-642-04864-7_9.

[259] Rajiv Krushna Kamilla. *Composite Fermions: Physics of 2-Dimensional Electron Systems Under Strong Magnetic Fields*. PhD thesis, Stony Brook University, 1997.